REPUBLIC OF TURKEY YILDIZ TECHNICAL UNIVERSITY GRADUATE SCHOOL OF NATURAL AND APPLIED SCIENCES

INTEGRATION OF OPTICAL AND SYNTHETIC APERTURE RADAR IMAGERY FOR IMPROVING CROP MAPPING

Rouhollah NASIRZADEHDIZAJI

DOCTOR OF PHILOSOPHY THESIS

Department of Geomatic Engineering

Program of Remote Sensing and GIS

Advisor Prof. Dr. Füsun BALIK ŞANLI

Co-Advisor Prof. Dr. Ziyadin ÇAKIR

January, 2020

REPUBLIC OF TURKEY YILDIZ TECHNICAL UNIVERSITY GRADUATE SCHOOL OF NATURAL AND APPLIED SCIENCES

INTEGRATION OF OPTICAL AND SYNTHETIC APERTURE RADAR IMAGERY FOR IMPROVING CROP MAPPING

A thesis submitted by Rouhollah NASIRZADEHDIZAJI in partial fulfillment of the requirements for the degree of **DOCTOR OF PHILOSOPHY** is approved by the committee on 06.01.2020 in Department of Geomatic Engineering, Program of Remote Sensing and GIS.

Prof. Dr. Füsun BALIK ŞANLI Yildiz Technical University Advisor Prof. Dr. Ziyadin ÇAKIR Istanbul Technical University Co-Advisor

Approved By the Examining Committee Prof. Dr. Füsun BALIK ŞANLI, Advisor Yildiz Technical University Prof. Dr. Ali Melih BAŞARANER, Member Yildiz Technical University Prof. Dr. Elif SERTEL, Member İstanbul Technical University Prof. Dr. Bülent BAYRAM, Member Yildiz Technical University Assoc. Prof. Dr. Saygın ABDİKAN, Member Zonguldak Bulent Ecevit University

I hereby declare that I have obtained the required legal permissions during data collection and exploitation procedures, that I have made the in-text citations and cited the references properly, that I haven't falsified and/or fabricated research data and results of the study and that I have abided by the principles of the scientific research and ethics during my Thesis Study under the title of Integration of Optical and Synthetic Aperture Radar Imagery for Improving Crop Mapping supervised by my supervisor, Prof. Dr. Füsun BALIK ŞANLI. In the case of a discovery of false statement, I am to acknowledge any legal consequence.

Rouhollah NASIRZADEHDIZAJI Signature



ACKNOWLEDGEMENTS

First of all, I would like to express my sincere gratitude to my thesis and research advisor Prof. Dr. Füsun BALIK ŞANLI for her great support that helped me become an independent researcher. She always motivated me when I had struggling times and her ideas, attention to details and teaching helped me to improve my research immensely and learn lots of academic concepts in my PhD journey. At many stages in the course of this research, the critical discussions I had with her led me to develop a critical sense of thinking and encouraged me for thinking big.

I would also like to extend my deepest gratitude to my co-advisor Prof. Dr. Ziyadin ÇAKIR for his constant support, availability and constructive suggestions, which were determinant for the accomplishment of the work presented in this thesis.

Last, but not least, I deeply thank my parents who have been authentic proof of eternal love and support throughout my life. I am also grateful to my siblings for their timely encouragement and emotional support along the way. My PhD journey would not have been possible without the support of my family.

Rouhollah NASIRZADEHDIZAJI

TABLE OF CONTENTS

LI	ST O	F SYMBOLS	vii		
LI	ST O	F ABBREVIATIONS	X		
LI	ST OI	F FIGURES	xiii		
LI	ST O	F TABLES	xvii		
Αŀ	3STR	ACT	xviii		
Ö	ZET		xxi		
1	Intr	oduction	1		
	1.1	Literature Review	1		
	1.2	Objective of the Thesis	6		
	1.3	Hypothesis	7		
2	Gen	eral Overview of Satellite Remote Sensing Systems	9		
	2.1	Optical Remote Sensing Systems	10		
	2.2	Microwave Remote Sensing Systems	14		
3	Radar Bachground				
	3.1	Synthetic Aperture Radar	17		
	3.2	Radar image distortions	25		
	3.3	Microwave polarizations	30		
	3.4	Radar data formats	32		
	3.5	Radar signal and object interactions	33		
	3.6	Historical Background	34		
4	Inte	erferometric SAR	37		
5	Met	hodology	40		
	5.1	Polarimetric SAR Backscatter	40		
	5.2	Interferometric Coherence	43		
		5.2.1 Decorrelation Sources	45		

6	Opt	ical, SA	AR, PolSAR and InSAR Applications in Crop Monitoring and	
	Mapping			
	6.1	Sensit	ivity of Multi-Temporal SAR Parameters to Crop variables	48
		6.1.1	Materials and methods	48
		6.1.2	Study Area	49
		6.1.3	Field Surveys	50
		6.1.4	Sentinel-1 Dual Polarimetric SAR Data Statement and Processing	g 53
		6.1.5	SAR Parameters and Their Correlation with Crop Height	55
		6.1.6	SAR Parameters and Their Correlation with Crop Coverage	60
	6.2	Integr	ation of radar and optical datasets for crop mapping improvment	67
		6.2.1	Ground truth data acquisition	68
		6.2.2	Datasets	69
		6.2.3	SAR Image Pre-processing	69
		6.2.4	Optical Image Pre-processing	72
		6.2.5	Combination of SAR and optical data	72
		6.2.6	Crop Mapping	73
		6.2.7	Accuracy Assessment	73
	6.3	Multi-	temporal data analysis for crops growth monitoring and	
		fication of different crop types	77	
		6.3.1	Sentinel-1 SAR data statement and processing	78
		6.3.2	SAR backscattering analysis	79
		6.3.3	Crop mapping	79
		6.3.4	Accuracy assessment of crop classification	82
	6.4	Interfe	erometric coherence analysis to crop growth monitoring	85
		6.4.1	Coherence estimation and its relation with crop growth	86
7	Rest	ults An	d Discussion	94
Re	ferer	ices		97
Pu	ıblica	tions F	from the Thesis	108

LIST OF SYMBOLS

 ϑ Angle Variation from Near to Far Range

 θ_H Angular Spread of the Radar Beam in the Azimuth Direction

l Antenna length

 β_a Azimuth Beamwidth

 ρ_a Azimuth Resolution

 σ^0 Backscattering coefficient

 σ_B Bistatic Radar Cross Section

 C_p Complex Pixel

 Δ_{v} Constant Resolution on the Ground Range

 Δ_r Constant Resolution on the Slant Range

C Covariance Matrix

dB Decibel

 R_R Distance from the Receiver to the Object

 R_T Distance from the Transmitter to the Object

 B_{Dop} Doppler Bandwidth

 γ_{DC} Doppler Centroid Decoreelation

 f_D Doppler Frequency

χ Ellipticity Angle

 β_0 Estimated backscattered energy

y Frequency

 $\gamma_{spatial}$ Geometric or Spatial Baseline Decorrelation

 $ho_{\rm g}$ Ground Range Resolution of a RAR

K_C Hermitian Conjugate

HH Horizontal Transmission and Horizontal Reception

A_{ill} Illuminated Surface Area

 η Incidence Angle

 ψ Interferometric Phase

 $\Delta \varphi$ Interferometric Phase Difference

 $\theta_{i,local}$ Local incidence angle

 θ_{off} Off-nadir Angle

 ψ Orientation Angle

 α Orientation Angle of the Baseline

 ϕ Phase Difference

 V_s Platform Speed

 τ_p Pulse Length

*G*_{ant} Radar Antenna Gain

 ρ Range Azimuth

 ΔR Range Difference of Two SAR Observations

R Range from the Sensor to the Object

au Range Time

 \vec{E} Real Vector

 G_R Receiver Gain

S Scattering Matrix

c Speed of light

 ω_s Squint Angle

 γ_{SNR} System Noise Decorrelation

 H_p Target Height

 $\gamma_{temporal}$ Temporal Terrain Decorrelation

 $\gamma_{thermal}$ Thermal Decorrelation

 γ_{total} Total Correlation or Coherence

 P_T Transmitted Energy

 G_T Transmitter Gain

 ϕ Unwrapped Phase

VV Vertical Transmission and Vertical Reception

VH Vertical Transmission and Horizontal Reception

 γ_{vol} Volume Decorrelation

 λ Wavelength

LIST OF ABBREVIATIONS

ALOS Advanced Land Observing Satellite

AT Along-Track

BBCH Biologische Bundesanstalt, Bundessortenamt, and CHemische

BOA Bottom Of Atmosphere

CC Canopy Coverage

CSA Canada Space Agency

CT Cross-Track

DEM Digital Elevation Model

DInSAR Differential InSAR

ENVI Environment for Visualizing Images

ENVISAT Environmental Satellite

ERIM Environmental Research Institute of Michigan

ERS European Remote Sensing

ESA European Space Agency

ESM Electromagnetic spectrum

EVI Enhanced Vegetation Index

FVC Fractional Vegetation Cover

GMT Generic Mapping Tools

GMTSAR Generic Mapping Tools Synthetic Aperture Radar

GRD Ground Range Detected

GSD Ground Sampling Distance

HSV Hue, Saturation, and Value

InSAR Interferometric Synthetic Aperture Radar

IW Interferometric Wide swath

JERS Japanese Earth Resources Satellite

JPL Jet Propulsion Laboratory

LAI Leaf Area Index

LOS Line-Of-Sight

MLC Maximum Likelihood Classification

MSI Multispectral Instrument

MSS Multi Spectral Scanner

NASA National Aeronautics and Space Administration

NDVI Normalized Difference Vegetation Index

NDWI Normalized Difference Water Index

NESZ Noise Equivalent Sigma Zero

PI Pasture Index

PolSAR Polarimetri Synthetic Aperture Radar

RADAR RAdio Detection And Ranging

RAR Real Aperture Radar

RCS Radar Cross Section

ROI Regions of Interest

RVI Radar Vegetation Index

RVI Ratio Vegetation Index

SAR Synthetic Aperture Radar

SCP Semi-Automatic Classification plugins

SIR Shuttle Imaging Radar

SLAR Side Looking Aperture Radar

SLC Single Look Complex

SNAP Sentinel Application Platform

SNR Signal-to-Noise-Ratio

STRM Shuttle Radar Topography Mission

TOA Top Of Atmosphere

UTM Universal Transverse Mercator

WGS84 World Geodetic System 1984

LIST OF FIGURES

Figure	2.1	Electric and magnetic fields of the electromagnetic wave	9
Figure	2.2	The EMS different wavelength (frequency) regions	10
Figure	2.3	An illustration of optical remote sensing system (Image source: Sun	
		et. al.)	11
Figure	2.4	Spectral characteristics of typical surface features (Image source:	
		crisp)	11
Figure	2.5	The interactions of the radiation with targets on the earth's surface	12
Figure	2.6	Two different types of radiation reflection; specular reflection (left)	
		and diffuse reflection (right)	12
Figure	2.7	Visible and infrared wavelengths interactions with vegetation	
		leaves (left) and water (right)	13
Figure	2.8	Spectral responses of the vegetation and water over a variety of	
		different wavelengths	14
Figure	2.9	Parts of the electromagnetic spectrum	15
Figure	2.10	Microwave bandwidth ranges and specifications [72]	16
Figure	3.1	Geometry of RAR, side looking aperture radar [74]	18
Figure	3.2	Exemplification of the slant range [76]	19
Figure	3.3	RAR range resolution [75]	19
Figure	3.4	Geometry of imaging radar [75]	20
Figure	3.5	SAR system geometry with the parameters [77] [78]	21
Figure	3.6	Synthetic aperture processing, basic theory including the Doppler	
		effect, matched filter, and azimuth compression [80]	23
Figure	3.7	Radar Transmission scheme and coordinate system [82] [83]	24
Figure	3.8	SAR geometry in the plane indicating slant range versus ground	
		range resolutions [80]	26
Figure	3.9	Geometric distortions in radar images due to relief displacement [76]	27
Figure	3.10	Foreshortening effect when $0 < \alpha < \vartheta$, where the pixel on the ground	
		is highlighted [80]	27
Figure	3.11	Foreshortening effect when $-\vartheta < \alpha < 0$, where the pixel on the	
-			28
Figure	3.12	Lavover effect when $\vartheta < \alpha [80]$	29

Figure :	3.13	Shadow effect when $\alpha + \vartheta > 90 [80]$	29
Figure	3.14	Schematic of polarization pulse traveling from the radar and wave	
		interactions [88]	31
Figure	3.15	EM wave polarization represented in combination of two	
		orthogonal electric fields and direction of propagation a wave with	
		a circularly polarized wave (left) and polarization ellipse (right)[87]	31
Figure	3.16	Schematic illustrations of radar wave backscatter over various	
		surface cover conditions [92]	34
Figure -	4.1	Geometry of repeat-pass CT-InSAR (left) and AT-InSAR (right) [77]	37
Figure -	4.2	Configuration of the InSAR geometry [95]	38
Figure	5.1	Flowchart of data processing	47
Figure	6.1	The location map of the study area; general overview (left) and	
		Sentinel-2 RGB image of the study site (right)	49
Figure	6.2	Soil map of the study area	50
Figure	6.3	Land use map of the study area (Source: Copernicus Land	
		Monitoring Service [129])	51
Figure	6.4	Seasonal maize, sunflower and wheat calendar of the region	52
Figure	6.5	Different growth stages of crops in the study area	53
Figure	6.6	BBCH-scale relationship with crop height (a-c), and Correlation	
		between canopy coverage (CC) and crop height (d-f) for maize,	
		sunflower, and wheat	54
Figure	6.7	Flowchart of Sentinel-1 dual polarization SAR data processing	56
Figure	6.8	Correlation between (a) intensity arithmetic calculation of VV+VH,	
		(b) σ_{VV}^0 backscatter, and (c) σ_{VH}^0 backscatter values of maize with	
		its height during growing stages	57
Figure	6.9	Correlation between (d) intensity arithmetic calculation of VV+VH,	
		(e) σ_{VV}^0 backscatter, and (f) σ_{VH}^0 backscatter values of sunflowe	
		with its height during growing stages	58
Figure	6.10	Correlation between (g) intensity arithmetic calculation of VV+VH,	
		(h) σ_{VV}^0 backscatter, and (i) σ_{VH}^0 backscatter values of wheat with	
		its height during growing stages	59
Figure	6.11	Correlation between Entropy (a), Anisotropy, (b) and Alpha (c)	
		decompositions of maize with its height during growing stages	61
Figure	6.12	Correlation between Entropy (d), Anisotropy, (e) and Alpha (f)	
		decompositions of sunflower with its height during growing stages	62
Figure	6.13	Correlation between Entropy (g), Anisotropy, (h) and Alpha (i)	
		decompositions of wheat with its height during growing stages	63

Figure 6.14	Canopy coverage extraction from in-situ photo taken using python	
	image processing packages. Left panel is the original photo and the	
	right panel shows white ratio calculated as green areas and black	
	to the bare soil in wheat sample field	64
Figure 6.15	Correlation between σ_{VV}^0 (a), and VV+VH (b), backscatter values	
	of maize, and VV+VH (c) backscatter value of sunflower with their	
	CC during growing stages	66
Figure 6.16	Crop classification methodology	68
Figure 6.17	Flowchart of multi-temporal mapping	70
Figure 6.18	RGB color composite of Sentinel-1, (R: 2016.07.01_VH_dB, G:	
	2016.07.13_VV_dB, B: 2016.07.25_VH_dB)	71
Figure 6.19	Sentinels combined dataset (R: Near-Infrared, G: Red, B:	
	2016.07.25_VH_dB)	74
Figure 6.20	Crop classification of combined dataset (MLC)	75
Figure 6.21	Producer, User and Overall accuracies and Kappa coefficient	
	assessment of only Sentinel-1 SAR data	76
Figure 6.22	Producer, User and Overall accuracies and Kappa coefficient	
	assessment of combined dataset	76
Figure 6.23	Seasonal maize, sunflower, wheat and potato calendar in the study	
	area	77
Figure 6.24	Workflow of multi-temporal SAR analysis	78
Figure 6.25	The backscatter value of maize, sunflower, wheat and potato on	
	multi-temporal Sentinel-1 images, in ascending pass direction with	
	VH (top) and VV (bottom) polarization	80
Figure 6.26	The backscatter value of maize, sunflower, wheat and potato on	
	multi-temporal Sentinel-1 images, in descending pass direction	
	with VH (top) and VV (bottom polarization	81
Figure 6.27	RGB color composite using multi-temporal Sentinel-1 SAR	
	data in descending pass direction (R: 2016.05.15_VH_dB, G:	
	$2016.06.01_VV_dB$, B: $2016.07.31_VH_dB$)	82
Figure 6.28	Crop classification of SAR dataset (MLC)	83
Figure 6.29	Producer's, User's and Overall accuracies and Kappa coefficient	
	assessment of multi-temporal Sentinel-1 SAR data (percentages are	
	rounded to the nearest decimal)	84
Figure 6.30	Sentinel-1 imagery locations. The colored boxes with T indicate	
	the tracks and perpendicular arrows represent satellite propagation	
	direction and its LOS with longer and short arrows respectively and	
	vellow box shows the study area	87

Figure 6.31 Mean Coherence values of 9 maize fields during the seasonal
growth stages in the ascending pass direction for VH and VV
polarization in two different tracks. The date of images used for
coherence pair formation is represented in the $x - axis$ of the graph 88
Figure 6.32 Mean Coherence values of 9 maize fields during the seasonal
growth stages in the descending pass direction for VH and VV
polarization in two different tracks. The date of images used for
coherence pair formation is represented in the $x - axis$ of the graph 89
Figure 6.33 Mean Coherence values of 6 sunflower fields during the seasonal
growth stages in the ascending pass direction for VH and VV
polarization in two different tracks. The date of images used for
coherence pair formation is represented in the $x - axis$ of the graph 90
Figure 6.34 Mean Coherence values of 6 sunflower fields during the seasonal
growth stages in the descending pass direction for VH and VV
polarization in two different tracks. The date of images used for
coherence pair formation is represented in the $x - axis$ of the graph 91
Figure 6.35 Mean Coherence values of 5 wheat fields during the seasonal
growth stages in the ascending pass direction for VH and VV

polarization in two different tracks. The date of images used for

coherence pair formation is represented in the x - axis of the graph 92

LIST OF TABLES

Table 6.1	Biologische Bundesanstalt, Bundessortenamt, und CHemische	
	(BBCH)-identification keys for field measurements and Synthetic	
	Aperture Radar (SAR) data acquisitions of the study area	52
Table 6.2	Specifications of acquired Sentinel-1 datasets over Konya basin, Turkey	54
Table 6.3	Coefficient of determination (R^2) between crop height and	
	Sentinel-1 SAR parameters	60
Table 6.4	Coefficient of determination (R^2) between CC and Sentinel-1 SAR	
	parameters	65
Table 6.5	Specifications of Sentinel-1 and Sentinel-2	69
Table 6.6	Maximum Likelihood classification confusion matrix	84
Table 6.7	Percentages of errors of omission, errors of commission, Producer's	
	and User's accuracies for each class	84
Table 6.8	Characteristic parameters of acquired Sentinel-1 datasets	85
Table 6.9	Datasets acquisition dates for different orbits	86

Integration of Optical and Synthetic Aperture Radar Imagery for Improving Crop Mapping

Rouhollah NASIRZADEHDIZAJI

Department of Geomatic Engineering

Doctor of Philosophy Thesis

Advisor: Prof. Dr. Füsun BALIK ŞANLI Co-advisor: Prof. Dr. Ziyadin ÇAKIR

Land use/cover mapping is one of the main application fields of the remote sensing data and thus is well suited for mapping of seasonally changing variables such as agricultural areas. Since, crops are characterized by their typical spatial patterns, temporal dynamics and changing radiation reflecting and scattering behavior due to crop phenology and plant status, hence applying time series of remote sensing data within a short revisiting time would be a beneficial method for agriculture monitoring.

The aim of this thesis therefore, centered on the monitoring and investigation of the agriculture activities over the time in terms of estimation of the biophysical parameters, crops phenological development and different growth stages, the identification of certain types of crops, and providing useful information about crops status in the study region located in the Konya basin central Anatolia Turkey. In this work, Synthetic Aperture Radar (SAR) and optical as two different remote sensing systems were applied to investigate and evaluate the temporal and spatial variability of agricultural activities more precisely. The focus of this thesis is two-fold: (1) to evaluate the use of SAR, Polarimetric SAR (PolSAR) and Interferometric SAR (InSAR) techniques in estimation and monitoring of crop variables and parameters, and discuss their potential relationship with remotely sensed data and field observations (2) to investigate the integration of optical and SAR imagery for improving crop mapping, and discuss the performance of the sensors backscatter and reflectance for temporal crop type mapping with combination of the optical and SAR data.

For these purposes as a first work, the sensitivity of 10 parameters derived from multi-temporal C-band Sentinel-1 SAR data, to crop height and canopy coverage (CC) of maize, sunflower, and wheat in the study area were analyzed. The coefficient determination (R^2) of 0.82 indicates that there is a strong relationship between the maize height and SAR parameters of VV + VH, during the early growing stage. The maize CC is well correlated with VV parameter ($R^2 = 0.73$), however, it is observed that at the later growing stage the correlation became weaker. This means that the sensitivity decreases with increasing vegetation cover growth. The sensitivity of SAR parameters to wheat variables is often good at the early stage. The sunflower's CC shows a relatively higher correlation with VV polarization ($R^2 = 0.46$) at the early stage while no considerable correlation is observed at the later stage. The sunflower height also had an insignificant correlation with the majority of SAR parameters. It is found that Sentinel-1 SAR data has a high potential for estimation of crop height and CC of the maize as a broad-leaf crop. The same is not true for sunflower as another broad-leaf crop.

The next step was the application of Sentinel-1 multi-temporal data for crop monitoring and mapping and thereby extracting useful information, such as crops status, estimating irrigation and harvesting time according to the changes made in backscatters. From the backscattering analysis, it was observed that each similar crop type in different test fields due to the distinct methods of irrigation and fertilization has shown different intensity values. It has indicated that the homogeneity between SAR backscatters is high for each field with the same crop type in descending pass direction with VH polarization. In contrary, high-intensity values are recorded in VV polarization for entire crop types. It is also observed that polarimetric composite images for a different date are useful to roughly identify crop types, and validated with the application of classification methods in the study area.

Later on, two different Sentinels data types in the same period of time and the same scene have been selected to describe how to get information from combined optical and SAR data. Hereby, to discriminate different land use/cover categories of the study area, the potential of remotely sensed image analysis to merge multi-spectral and SAR images within a hierarchical classification framework was evaluated. Multi-temporal Sentinel-1, C-band VV, and VH polarized SAR data and Sentinel-2 optical data were acquired simultaneously by in-situ measurements to investigate the performance of the sensors backscatter and reflectance for temporal crop type mapping and the sustainable management of agricultural activities for the study area. Results showed that the combination of the radar and optical data indices caused to enhance crop classification methodology and classification accuracies were improved results (5%) using combinations of sensors and reached 93% in this study.

Finally, the correlation between different phenological stages (sowing, growth, and harvesting) of the crops and radar coherence were studied. Within the context of this work, the relationship between the interferometric coherence calculated from the different pass directions and multi-track of 12 and 6-day Sentinel-1 SAR image pairs and the different crop type's growth stages (i.e. sowing, growing and harvesting) were investigated. For this purpose, field surveys were conducted for validation of the correlation between the coherence and crop growth status. For interferometric coherence analysis to monitoring the time evolution of different crop fields, 31 SAR images in ascending and 31 in descending orbit direction were acquired throughout the same growth season of the subject area. The results showed that coherence values were high before plowing and seeding and had sharp coherence decrease with starting the growing the crops. During the growth stage of crops the values stay low and slightly similar for each field and crop type. The coherence values were significantly higher after crop harvesting and reaping the remnants of the crops. In comparing with ascending pass direction it has indicated that coherence value is high for each field with the same crop type in descending orbit.

This dissertation emphasizes the potentialities of the remote sensing data - the methodology of SAR, PolSAR and InSAR time-series analysis and integrated use of SAR and optical data to efficiently evaluate the crop variables and parameters at different phenological stages and crop map as an agricultural monitoring and management strategies. To the better interpretation of the sensitivity of SAR parameters to the crop biophysical variables most precise field observations are needed and as the further work high spatial resolution SAR data would be efficient to achieve more accurate information regarding agricultural activities and crop studying.

Keywords: Agricultural monitoring, Sentinel-1 SAR backscatter, polarimetric and interferometric SAR, crop variables, crop mapping

YILDIZ TECHNICAL UNIVERSITY
GRADUATE SCHOOL OF NATURAL AND APPLIED SCIENCES

Ürün Deseni Haritası Üretimini İyileştirmek Üzere Optik Ve Sentetik Açıklıklı Radar Görüntülerinin Entegrasyonu

Rouhollah NASIRZADEHDIZAJI

Fotogrametri Anabilim Dalı Doktora Tezi

Danışman: Prof. Dr. Füsun BALIK ŞANLI Eş-Danışman: Prof. Dr. Ziyadin ÇAKIR

Arazi kullanımı/örtüsü haritası üretimi, uzaktan algılama verilerinin ana uygulama alanlarından biridir ve tarımsal alanlar gibi mevsimsel olarak farklılık gösteren değişkenlerin haritalanması için çok uygundur. Tarım alanları tipik mekansal özellikleri ile karakterize edildiğinden bitki fenolojisi ve bitki durumuna bağlı olarak paternler, zamansal dinamikler ve değişen ışınımın yansıma ve saçılma davranışlarından dolayı uzaktan algılama sistemleri ile izlenebilmektedir. Uyduların kısa aralıklarla tekrarlı geçişleri sayesinde elde edilen zaman serisi verileri ile tarım alanlarının izlenmesinde çok faydalı bir method olarak kabul edilmektedir. nedenle, bu tezin amacı, zaman içerisinde bitkilerin biyofiziksel parametrelerinin tahmini, bitkilerin fenolojik gelişmeleri ve farklı büyüme aşamaları, bitki türlerinin belirlenmesi ve bu konuda bitkilerin statüsü ile ilgili yararlı bilgiler verilmesi açısından Türkiyenin Konya havzasında bulunan çalışma bölgesinde ekili alanların tarımsal faaliyetlerin izlenmesi ve araştırılması konusuna odaklanmıştır. Bu çalışmada, tarımsal faaliyetlerin zamansal ve mekansal değişkenliğini daha kesin ve doğru olarak araştırmak ve değerlendirmek için Sentetik Açıklık Radarı (SAR) ve optik sistemler iki farklı uzaktan algılama veri kaynağı olarak kullanılmıştır. Bu tezin iki temel odağı vardır: (1) SAR, Polarimetric SAR (PolSAR) ve Interferometric SAR (InSAR) tekniklerinin bitki değişkenleri ve parametrelerinin tahmini ve izlenmesinde kullanımını değerlendirmek ve uzaktan algılanan verilerle arazi gözlemleri arasındaki potansiyel ilişkiyi analiz etmek; (2) ürün deseni haritalarının iyileştirilmesi için optik ve SAR görüntülerinin entegrasyonunu araştırmak ve aynı zamanda optik ve SAR verilerini birleştirerek yansıma ve saçılma değerlerinin zamansal ürün deseni harita üretimindeki performansını analiz etmektir.

Bu amaçlar için ilk çalışmada, çok zamanlı C-bant Sentinel-1 SAR verilerinden elde edilen 10 parametrenin, çalışma alanındaki mısır, ayçiçeği ve buğday bitkilerinin yüksekliği ve toprağı örtme oranına (CC) olan duyarlılığı analiz edildi. Korelasyon katsayısı değerleri, ilk büyüme aşamasında mısır için yüksek bir korelasyon olduğunu göstermektedir. Saptama katsayısı ($R^2 = 0.82$), ilk büyüme aşamasında, VV + VH'nin mısır yüksekliği ile SAR parametreleri arasında yüksek bir ilişki olduğunu göstermektedir. Mısırın toprağı örtme oranı, VV parametresi ile iyi korelasyonludur $(R^2 = 0.73)$, ancak son büyüme evresinde korelasyonun zayıflaştığı görülmektedir. Yani bitki örtüsünün büyümesi arttıkça duyarlığının azaldığı anlamına gelir. SAR parametrelerinin buğday değişkenlerine duyarlılığı ilk aşamada genellikle iyidir. Avciceğinin toprağı örtme oranı, ilk asamada VV polarizasyonu ($R^2 = 0.46$) ile nispeten daha yüksek bir korelasyon gösterirken, sonraki aşamada önemli bir korelasyon gözlenmemiştir. Ayçiçeği yüksekliği, SAR parametrelerinin çoğunluğu ile anlamlı olmayan bir korelasyona sahiptir. Sentinel-1 SAR verilerinin, geniş yapraklı bir bitki olarak mısırın toprağı örtme oranı ve boyunu tahmin etmek için yüksek bir potansiyele sahip olduğu bulunmuştur. Aynısı durum diğer bir geniş yapraklı bitki olan ayçiçeği için geçerli değildir.

Bir sonraki adım, Sentinel-1 çok-zamanlı verilerinin kullanılmasıyla ürünlerin izlenmesi ve haritalarının üretilmesi ve böyleyce geri saçılmalarda oluşan değişikliklere göre bitkinin durumu, sulama ve hasat zamanı gibi yararlı bilgilerin çıkarılmasıyla ilgilidir. Geri saçılma analizinden, farklı sulama ve gübreleme yöntemleri nedeniyle farklı test alanlarındaki benzer bitki türlerinin farklı yoğunluk değerlerin elde edildiği görülmüştür. SAR geri saçılmaları arasındaki homojenliğin, VH polarizasyonu ile alçalan geçiş yönünde aynı bitki tipinde olan her alan için yüksek olduğunu göstermiştir. Ancak yüksek yoğunluk değerleri tüm ürün tipleri için VV polarizasyonunda kaydedilmiştir. Farklı tarihlerde elde edilen polarimetrik kompozit görüntülerin bitki tiplerini kabaca tanımlamak için yararlı olduğu gözlemlenmiştir ve çalışma alanında sınıflandırma yöntemlerinin uygulanmasıyla doğrulanmıştır.

Daha sonraki aşamada, aynı zaman dilimine ve aynı alana ait Sentinel 1 ve Sentinel 2 verileri SAR ve optik verilerin birleştirilmesi ile nasıl bilgi elde edileceği amacıyla seçilmiştir. Böylelikle, çalışma alanının farklı arazi kullanımı/örtüsü kategorilerini ayırt etmek için, hiyerarşik bir sınıflandırma çerçevesi içinde çok bantlı optic ve SAR görüntülerini birleştirmek üzere uzaktan algılama görüntü analizi potansiyeli değerlendirilmiştir. Arazi çalışmaları ile aynı tarihte alınan çok zamanlı Sentinel-1,

C-band VV ve VH polarizasyonlu SAR verileri ve Sentinel-2 optik verileri, sensörlerin geri saçılma ve yansıma performansı zamansal ürün deseni harita üretimi ve tarımsal faaliyetlerinin sürdürülebilir yönetimininde kullanılşabilirliğini araştırmak amacıyla incelendi. Sonuçlar, radar ve optik verilerin kombinasyonunun bitki sınıflandırma doğruluğunun artmasını sağladığı (5%) ve bu çalışmada toplam doğruluğun 93%'e ulaştığını gösterdi.

Son çalışma, bitkilerin farklı fenolojik aşamaları (ekim, büyüme ve hasat) ve radar tutarlılığı (coherence) arasındaki ilişkiyi incelemektedir. Bu çalışma kapsamında, farklı geçiş yönlerinden hesaplanan interferometrik tutarlılık ile 12 ve 6 günlük farklı izlerde alınan Sentinel-1 SAR görüntü çiftlerinin farklı ürün türleri için büyüme aşamaları (yani ekim, yetiştirme ve hasat) arasındaki ilişki araştırılmıştır. Bu amaçla, tutarlılık ile bitki büyüme durumu arasındaki korelasyonun doğrulanması için arazi çalışmaları yapılmıştır. Farklı bitki alanlarının zaman evrimini izlemeye yönelik interferometric tutarlılık analizi için, söz konusu alanın aynı büyüme mevsimi boyunca yükselen ve alçalan yörünge yönünde 31 SAR görüntüsü kullanılmıştır. Sonuçlar, tarlaların sürülmesi ve tohumlanmasından önce korelasyonun yüksek olduğununu ve bitkilerin büyümeye başladığında korelasyonun keskin bir şekilde azaldığını göstermiştir. Bitkilerin büyüme aşamasında, değerler her bir ürün tipi için düşük ve az da olsa benzer kaldığı gözlemlenmiştir. Tutarlılık değerleri, bitkinin hasadı ve bitkilerin kalıntılarının toplanmasından sonra önemli ölçüde yüksek değerde elde edilmiştir. Yükselen geçiş yönüyle karşılaştırıldığında, alçalan yörüngede aynı bitki tipinde olan her alan için tutarlılık değerinin yüksek olduğu gözlemlenmiştir.

Bu tez çalışması, uzaktan algılama verilerinin zaman serisi analizi ve farklı fenolojik aşamalardaki ürün değişkenleri ve parametreleri için – SAR, PolSAR ve InSAR ve de SAR ve optik verilerin entegre kullanılamasında ve ayrıca tarımsal izleme ve yönetim stratejileri olarak ürün deseni haritasını etkin bir şekilde değerlendirmesinde ki potansiyelini vurgulamaktadır. SAR parametrelerinin bitki biyofiziksel değişkenlerine duyarlılığının daha iyi yorumlanması için hassas arazi gözlemleri gereklidir ve bir sonraki çalışmada tarımsal faaliyetler hakkında daha doğru bilgi elde etmek üzere yüksek mekansal çözünürlüklü SAR verileri değerlendirilecektir.

Anahtar Kelimeler: Tarımsal izleme, Sentinel-1 SAR geri saçılması, polarimetrik ve interferometrik SAR, ürün değişkenleri, ürün deseni haritası üretimi

YILDIZ TEKNİK ÜNİVERSİTESİ FEN BİLİMLERİ ENSTİTÜSÜ

1 Introduction

1.1 Literature Review

Crops as food resources have a substantial importance in socio-economic issues of societies in terms of sustainable management. In this regard, sustainable food security is dependent on precise agricultural activities monitoring and the collection of accurate farming information [1]. Accordingly, agriculture is amongst important activities that have played a key role in providing food security to a growing population of the world [2]. Precision agriculture is a management strategy that integrates information and communication technologies with the agricultural industry. Therefore, the information of each component of the small area in a farm is used to adapt the type and amount of inputs in those areas in order to evaluate and manage the temporal and spatial variability more precisely. Spatio-temporal observing and evaluation of crop type as an agricultural monitoring system is a critical step regarding estimate the area allocated to each crop type, computing statistics for crop control of area-based subsidies or crop production forecasting, environmental impact analysis and some other applications. In fact, targeting and monitoring programs are designed to promote economic and environmental sustainability as an agricultural management policy [3].

Land use/cover mapping is one of the main application fields of the remote sensing data and thus is well suited for mapping of seasonally changing variables such as agricultural areas. Since, agricultural lands are characterized by their typical spatial patterns, temporal dynamics and changing radiation reflecting and scattering behavior due to crop phenology and plant status, hence applying time series of remote sensing data within a short revisiting time can be utilized for better discrimination and identification of different crops, investigating crop variables (e.g. crop height, canopy coverage and water content) for improvements in crop growth monitoring, crop disaster prediction and providing accurate information to precise farming. Thus, decision-makers can have accurate and updated information regarding crop management; agricultural production planning, food security stability

promotion, crop trading market, etc. Besides, farmers also benefit from obtaining timely information about crop phenological development as well as yield estimation. Therefore, Satellite data are widely used to study and investigate agriculture activities changes as dynamic phenomenon over the time and in terms of quantitative and qualitative agricultural products, estimation of the planted area, the identification of certain types of crops, the growth stages and crops tragedy prevision [4].

Remote sensing technologies that generating satellite data, are known as the most unique and important source of information about the earth and other planets in the space. The applicability of the satellite data is unlimited, providing various and multi-fold advantages of the global, regional and local scale. Earth observation satellites that transmit electromagnetic spectrum (EMS) energy and collect data (reflecting and radiating) of the earth's characteristics, in terms of their passive or an active imaging instrument mode are two different remote sensing systems. Different sensors measuring various wavelength portion (e.g. visible, near-infrared or microwave) of the EMS. The remote sensing systems that their measurements depend upon the external energy source, such as sun are known as passive and which the transmitted energy from the sensor provided by system's itself referred to active remote sensing systems [5]. Optical (passive) and SAR (active) are two different sources of remote sensing systems that can be applied separately or integrated, offering unique spectral and textural information for land use/cover evaluations, changes and generating information with higher quality [6]. The sensors that functioning in the optical region of wavelength spectrum obtaining information on visible, near-infrared and shortwave infrared wavelengths. Images obtained in the optical spectrum from multi-spectral sensors due to their high spectral and spatial resolutions and therefore, their straightforward interpretability are preferred data sources in the case of favorable weather conditions. However, during the persistent and long-lasting period of cloud cover in the rainy season and in the darkness, the use of optical sensors are limited for the continuous monitoring of the earth surface and characteristics [7].

One of the first remote sensing studies in vegetation monitoring is related to the year 1973, one year after the launch of the ERTS-1 satellite (Earth Resources Technology Satellite)- the first series of Landsat (Landsat 1) satellites, where Rouse et al. [8] have been developed a method for quantitative measurement of vegetation conditions over wide areas using ERTS-1 MSS (Multi Spectral Scanner) data. The main objectives were to evaluating of the application of the ERTS-1 spectral bands 5 and 7 data to compute a Band Ratio Parameter (correlation of the Band Ratio Parameter above-ground green biomass and vegetation water content) for measuring the vegetation type, amount, and condition of rangeland vegetation to provide a new data source for

regional basis agro-economic applications. Their project resulted that the proposed method using ERTS-1 MSS data had good potential for mapping vegetation conditions and for providing growth information in the test area. Different multispectral and hyperspectral optical data for various purposes are used in the agriculture domain. It has been achieved for many applications such as vegetation indices (e.g. Normalized Difference Vegetation Index (NDVI), Leaf Area Index (LAI), Normalised Difference Water Index (NDWI), Enhanced Vegetation Index (EVI), Pasture Index (PI), Ratio Vegetation Index (RVI), and etc. [8–13], nitrogen management [14–18], pasture management [19], identification of different crop types, crop's development monitoring and mapping [20–27], crop acreage estimation [28], yield and production forecasting [29–32], and other applications.

The role of active remote sensing systems including SAR, polarimetric SAR (PolSAR) and interferometric SAR (InSAR) in agricultural activities was investigated in different previous studies. SAR sensors are an active system independent of illumination sources, equipping the microwave region of the EMS with long wavelengths to collection of data in day-or-night and in different weather conditions with a constant observation of earth surface from the polar orbit [2, 33]. Microwaves can penetrate through clouds where the cloudy sky is a serious obstacle to the application of optical images particularly in a rainy climate. The SAR system has sensitivity to the physical morphology and the geometrical characteristics of the land surface and cover (soil roughness, moisture, vegetation structure, etc.). Therefore, radar sensors collect the echoes of the backscattered signal in a sequential way thus very different to that of optical satellite data, which measure reflected solar light in visible and infrared wavelengths [34]. The SAR technique has become increasingly an effective method of providing seasonal agricultural monitoring [1, 2]. The superiority of radar remote sensing techniques and capabilities of SAR technology have convinced researchers and government officials to apply it as a widely used, practical and efficient tool in such applications. The SAR system is sensitive to the vegetation biophysical variables and dynamical characteristics of plant targets, and underlying soil parameters such as moisture content, soil surface roughness, deflection and irregularity, geometric property, and due to its high spatial and temporal resolution help to perform field-level crop classification and monitoring activities [4, 35–37]. In addition, SAR sensor has a capability to differentiate crop types due to its sensitivity to the crop structure and water content. Plant water content, roughness, leaf size, and vegetation greenness level that are related to the bio-physical characteristics of the features represent the amount of reflectance. Crop structure and water content are variables that varying in respect with crop type, growing stage and crop conditions [38]. Different crop types at each phenological stage show different bio-physical characteristics [36]. Therefore,

for various land cover features, SAR products provide the feasibility of estimating crop height, crop type and crop condition mapping which are valuable information for different agricultural applications and marketing of agricultural yields [39].

Optical sensors are beneficial for crop mapping and reliable applicants for agricultural land use monitoring as they measure reflectance from targets in the electromagnetic spectrum (reflectance in visible and shortwave infrared and thermal spectrum). However, success in crop identification with optical data mainly depends on the acquisition of image during key crop phonological stages. The accuracyof the classification decreases during these critical periods if optical data are used [3]. When added to the broad land use/cover classes' information provided by the optical data, the surface roughness and moisture information which are provided by SAR sensor allow one to extract more detailed specification of land surface and features [2]. Integrating both optical (reflectance) and Synthetic Aperture Radar (backscatter) multi- temporal features provides some advantages in terms of a more reliable crop map. Combining data from different sources of remote sensing data such as optical and radar datasets offer unique spectral and textural information for land use/cover evaluations, characterizing land use changes and generating information with higher quality than the individual datasets [6]. The high potential of inegration of the SAR and optical datasets can meet various observational needs for land research activities such as agriculture monitoring [40–45].

Scattering SAR data can be obtained in different wavelengths and polarizations. Texture measures, multi-sensor fusion, multi-polarization data, multi-temporal data and polarimateric data are techniques which is used to classification of the vegetation type [46, 47]. In agricultural studying, interactions between radar configuration (frequency, wavelength, polarity, and incident angle) with each other, as well as its interaction with the plant variables, has made the use and interpretation of radar data useful but complicated [48–50]. In this regard, radar parameters such as polarization which affect the signal scatter and target parameters that influence the signal propagation is subject to study. Object characteristics such as orientation, material constituents, configuration, and dielectric properties can be estimated using SAR Polarimetry (PolSAR) [51, 52].

Previous studies have demonstrated the sensitivity of polarimetric SAR to crop variables such as crop leaf area index (LAI), and crop biomass [53–55]. Processing and analyzing of the radar signals indices at different wavelengths, frequencies, incident angles, and polarization are amongst the techniques used in the studies of the crop biophysical characteristics [6]. In a study of monitoring and estimating wheat yield, Mattia et al. [55] investigated the sensitivity of multi-temporal C-band, polarizations

(HH and VV) to biophysical parameters, and the relationship between the radar and biophysical measurements on the wheat development stages. In order to maximize the sensitivity of SAR sensors for the maize growth cycle monitoring and mitigating the soil moisture impact on the signal and in SAR time series, Blaes et al. [56] developed a model by simulating the signal in all possible configurations (polarization and incidence angles at C-band) for ENVISAT, RADARSAT, and ERS SAR images and they found that dual polarizations indices are more sensitive to maize growth and less sensitive to soil moisture variations. Ruiz et al. [35] utilized multi-polarized RADARSAT-2 data to set up indicators of crop condition and yield estimation for corn crop growth stages by obtaining polarization signatures from radar data, and applying related crop parameters and vegetation indices in Central Mexico. The results indicate that the application of RADARSAT-2 polarimetric SAR data isoperational in the agricultural activities. Liao et al. [57] investigated the sensitivity of RADARSAT-2 polarimetric SAR (C-band) data using sixteen parameters to crop height and fractional vegetation cover (FVC) variables of corn and wheat. They explored that the corn height and FVC are strongly correlated with SAR parameters at the early growing stage but the correlation is low at the later growing stages. Furthermore, they observed that the sensitivity of SAR parameters to wheat variables (height and FVC) is very low. The study concluded that RADARSAT-2 polarimetric SAR (C-band) data has high potential in crop variables estimation for broad-leaf crops. Some other studies have also investigated the potential use of PolSAR technique as an agricultural monitoring method such as using backscatter intensities of TerraSAR-X, ASAR/ENVISAT, and PALSAR/ALOS data to the detection of sugarcane harvesting events [58], analysing the COSMO-SkyMed X-band, ENVISAT ASAR, and ALOS PALSAR backscatter values relationship to the vegetation indices [59] and the sensitivity of C-band and X-band PolSAR to grasslands moving events [60, 61].

Regarding the different agricultural applications of SAR system and based on the analysis of backscatter intensities, InSAR approach has also shown the potentiality for monitoring and management practices and vegetation change detection. As the first applications of InSAR-based technique in vegetation parameters assessment were abrupt changes detection in vegetation in the forest region [62] and deforestation observations [63]. The InSAR-based approach has been applied for agricultural monitoring in terms of comparing interferometric coherence for mowed grasslands with grasslands covered by vegetation [64, 65], ploughed bare fields and vegetation with low height [66, 67], and the importance of the meteorological effects in the interpretation of interferometric coherence [68–70]. The relationship between the repeat pass temporal interferometric coherence C-band SAR and grasslands mowing events, and also temporal decorrelation affected by precipitation in Central Estonia

were investigated by [71] and resulted the feasibility of interferometric coherence for mowing detection and the source of factors that affect the coherence such as farming activities and meteorological conditions were determined.

On this purpose it is aimed to research different remote sensing systems including optical, SAR, PolSAR and InSAR in agricultural activities to crop monitoring, management and mapping in the selected test area in the konya basin, Turkey. In this study, the goal is application of the remote sensing system's potential to provide useful information during growing stages of different crop types and seasonally changing variables and hence, the information of each component of the small area in a farm is used to adapt the type and amount of inputs in those areas in order to evaluate and manage the temporal and spatial variability more precisely.

1.2 Objective of the Thesis

Agriculture in Turkey as one of the top ten largest agricultural producer in the world plays a critical role in socio-economic terms of the country. Due to its great variety in geomorphology, topography and climate, therefore, a large percentage of the country is allocated to the agricultural land, and hereby a great number of the population is employed in agriculture. The conventional agricultural survey and management, and crop condition monitoring which mainly based on field observations on small scale and being non-real-time, thus used to be time and labor-consuming and expensive. Whereas the plant biological and biophysical parameters which are measuring from the field surveys, can also be derived from remotely sensed data, freely or at a very low cost, in high frequency and more precisely at a very wide range of scales, from the micro-level to global surveys. On the other hand, for precision agriculture, real-time basis information and reliable data leading to better response times and allowing to take on time and appropriate actions. Therefore, remote sensing systems provide the actual synoptic view of large region at a time, frequently and accurate for those purpose, which is not possible to obtain from conventional survey methods.

This thesis attempted to investigate different remote sensing techniques and applications in crop monitoring and mapping in the study area. The main objective is to assess the sensitivity of remote sensing data to the crop variables (i.e. crop height and canopy coverage) of different crops and comparing the finding with the data acquired from field observation during the crop growing season. Moreover, the potential of the remote sensing data in crop condition estimation and the integration use of different sensors data to discriminate the different crop types were investigated. Therefore, the intention of this study is two-fold: (1) to highlight the potential use

of SAR, PolSAR and InSAR systems in crop variables and parameters estimation and assessment of the relationship with remotely sensed data and field observations in agricultural studying (2) to investigate the optical and radar data integration approach to the enhancement of crop mapping, and the performance of the sensors backscatter and reflectance for temporal crop type discrimination with a combination of the optical and SAR data. In order to evaluate the capability and efficiency assessment of the sensors, the datasets were acquired parallel to the field surveys in 2016 in the study area. The summary of the main contributions of this work is as follows:

- 1. To evaluate the sensitivity of different dual polarimetric SAR parameters to crop height and CC of maize, sunflower and wheat, and to investigate the changes in SAR backscatter arising from crop height and CC during crop phenological stages.
- 2. To investigates the potential of polarimetric SAR backscatter data in an agricultural area for growth monitoring of different crop types (maize, sunflower, wheat and potato) and crop mapping using that polarimetric composite of images which are produced from multi-temporal analysis.
- 3. To demonstrate the potential of discriminating crop types using polarimetric SAR (backscatter) in integration with useful optical (reflectance) indices.
- 4. To studying the relationship between the interferometric coherence calculated from the different pass directions and multi-track SAR image pairs and the different crop type's growth stages (i.e. sowing, growing and harvesting).

1.3 Hypothesis

To indicate the sensitivity of the SAR Parameters to Crop variables the research hypotheses were that:

- There is correlation between the SAR backscattering values with each crop in the different growing stages and SAR parameters are most correlated with crop variables.
- The different crop types from the same leaf category show the similar correlation between SAR parameters and crops variables.

To show the potentiality of the time-series analysis of the SAR polarimetry in growth monitoring and the temporal backscatter changes for different crop types and crop mapping:

- Useful information about crop status can be extracted from SAR backscattering values

during growing stages where polarity can affect intensity values.

- The classification of the polarimetric composite of the images can help to identify crop types.

To illustrate the advantages of the integration of the optical and SAR datasets:

- The integrated use of the optical and SAR data and a combination of different datasets can improve the crop classification results.

To assess the interferometric coherence capability to crop growth monitoring using InSAR repeated-pass approach:

- The interferometric coherence calculated from the multi-track and different pass directions of the SAR image pairs indicates the high correlation with crop growth status.

General Overview of Satellite Remote Sensing Systems

The events or objects that are being observed with remote sensing sensors, the information needs a physical carrier to move from the events/objects to the sensors via an intervening environment. The output of the obtained information from the scene being observed is an image that is required the additional steps of processing and analyzing to make the interpretation possible. In general, electromagnetic waves are as an information carrier in remote sensing systems. Electromagnetic waves are energy that transported through space in the form of periodic disturbances of electric and magnetic domains at the same speed as commonly known as the speed of light (Figure 2.1).

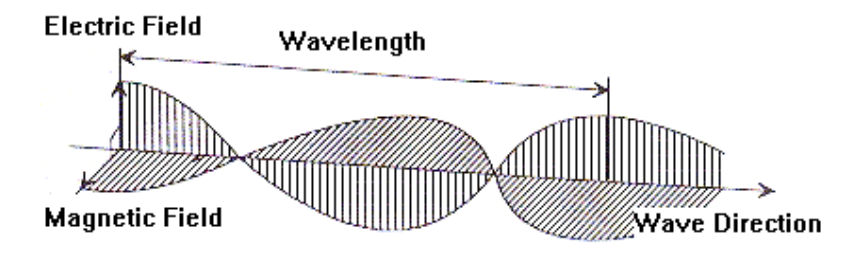


Figure 2.1 Electric and magnetic fields of the electromagnetic wave

An electromagnetic wave is specified by a frequency and a wavelength and these two quantities are related to the light speed and is shown as the equation 2.1.

speed of light (c) = frequency (v) × wavelength (
$$\lambda$$
) (2.1)

The frequency and therefore, the wavelength of an electromagnetic wave depend on the energy source. In our physical world there is a wide range of frequency encountered, beginning from the low frequency (long wavelength) of the radio waves of the electric waves created by the energy transmission lines and end to the very high frequency (very short wavelength) of the gamma rays originating from the atomic nuclei. This broad frequency domain of electromagnetic waves forms the Electromagnetic Spectrum (EMS). Figure 2.2 shows several wavelength (frequency) regions of the EMS.

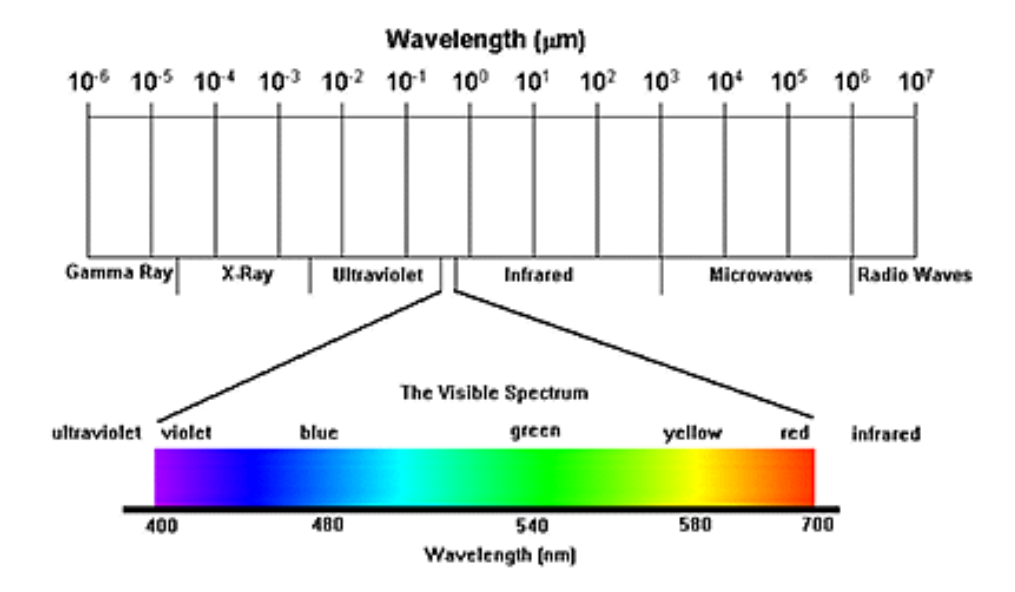


Figure 2.2 The EMS different wavelength (frequency) regions

From the wide range of electromagnetic radiation, only a narrow band of the EMS ranging from 400 to 700 nm is visible to the human eyes. Regarding the boundary between the EMS regions, it should be considered that the boundaries are approximate and two adjacent portions can be overlapped. Therefore, earth observation satellites in terms of their sensors' capabilities of using different parts of the EMS and also their energy source are categorized into two distinct optical and microwave remote sensing systems.

2.1 Optical Remote Sensing Systems

Optical sensors detect solar radiation (sunlight) reflected and/or emitted from the surface features of earth and targets on the ground to form images of the earth's surface and characteristics (Figure 2.3). The sensors that functioning in the optical region of wavelength spectrum obtaining information on visible, near-infrared and shortwave infrared wavelengths. Different features such as constructions, vegetation, water, cloud, road, and soil reflect visible and infrared radiation in different ways (Figure 2.4). The radiation after being emitted from its energy source (e.g. sun) and before used for remote sensing has to travel distances through the earth's atmosphere to reaches the earth's surface. The incoming electromagnetic radiation to the sensor due to the mechanisms which are known as scattering and absorption caused to be attenuated and redirected from its original pathway. These mechanisms are related to

the existence of particles or large gas molecules in the atmosphere and the interaction of light or radiation with these particles or gases. Therefore, the amount of scattering and absorption can be changed depending on the the distance the light travels through the atmosphere, the wavelength of the radiation, and the redundancy of particles or gas molecules.

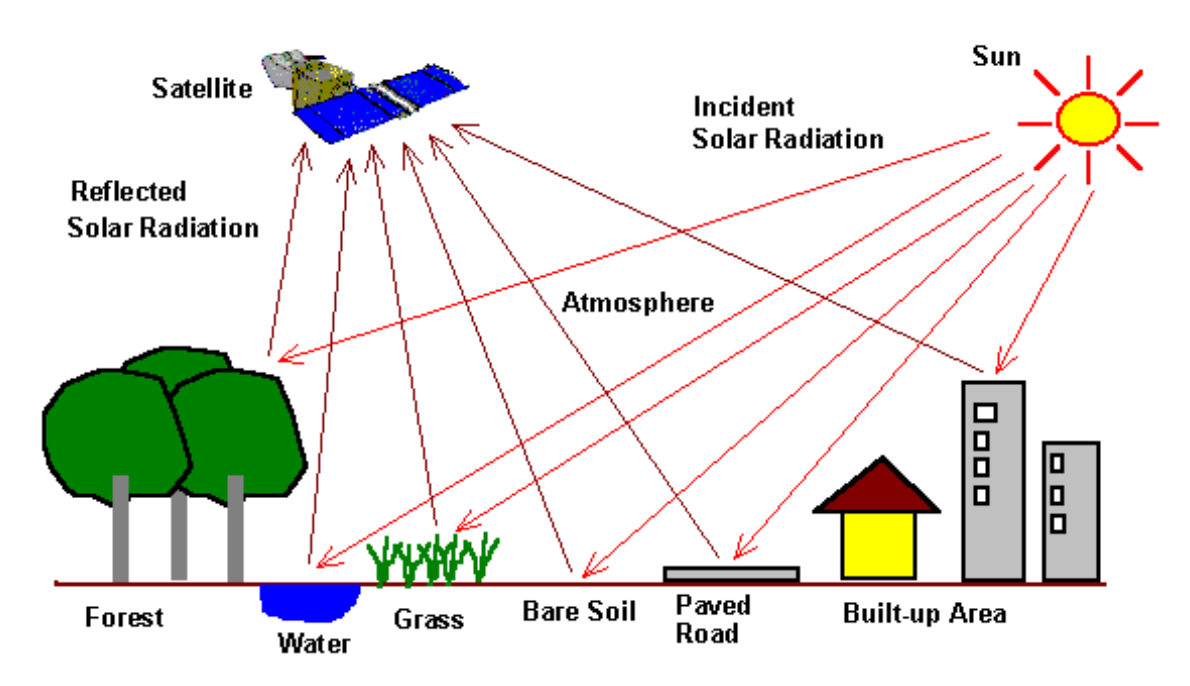


Figure 2.3 An illustration of optical remote sensing system (Image source: Sun et. al.)

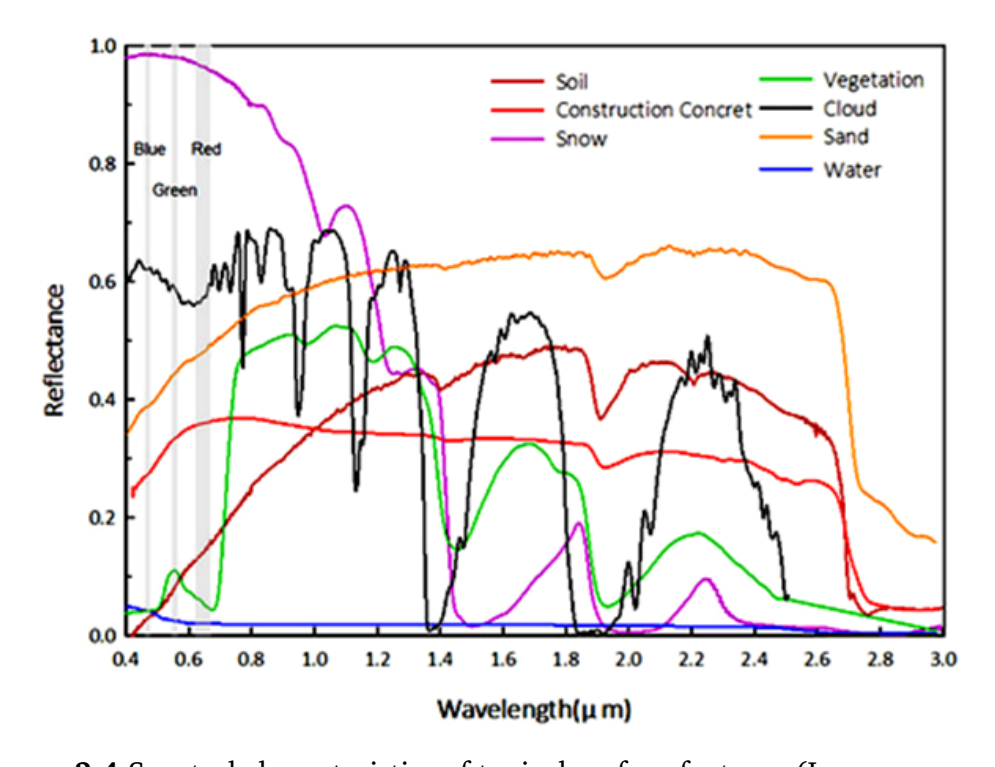


Figure 2.4 Spectral characteristics of typical surface features (Image source: crisp)

The rest of the radiation that is not scattered or absorbed in the atmosphere and reaches the ground can interact with the targets and the earth's surface. The Target Interactions when the energy hits or is incident (I) upon the surface are normally happening in three forms including absorption (A); transmission (T); and reflection (R) [72] as shown in Figure 2.5. With regard to the wavelength, the substance and the condition of the features, the proportions of each interaction will differ and hence, the collected incident energy will interact with the ground in one or more of these three forms.

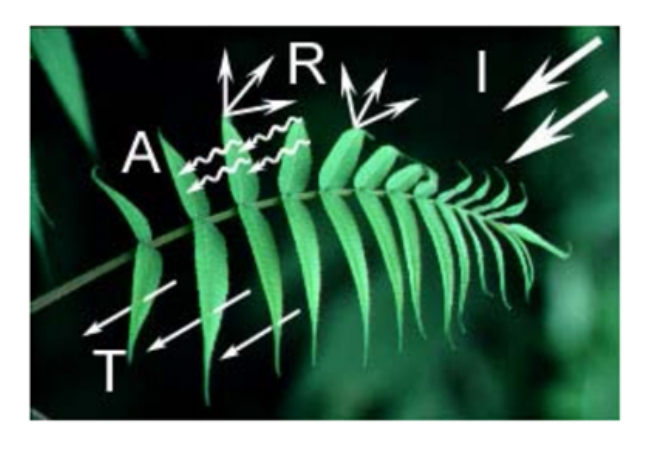


Figure 2.5 The interactions of the radiation with targets on the earth's surface

Among these three ways of interaction, the most interesting form in remote sensing is the reflection (R) and when the radiation bounces off from the object and redirected. Depending on the surface characteristics two types of radiation reflection occur, specular reflection and diffuse reflection (Figure 2.6). When a surface is smooth, approximately all the energy that reaches the ground is directed off from the surface in a single direction, and therefore, specular or mirror-like reflection occurs. Whereas, diffuse reflection happens when the surface is rough and the energy is reflected nearly in a uniform manner in different orientations.

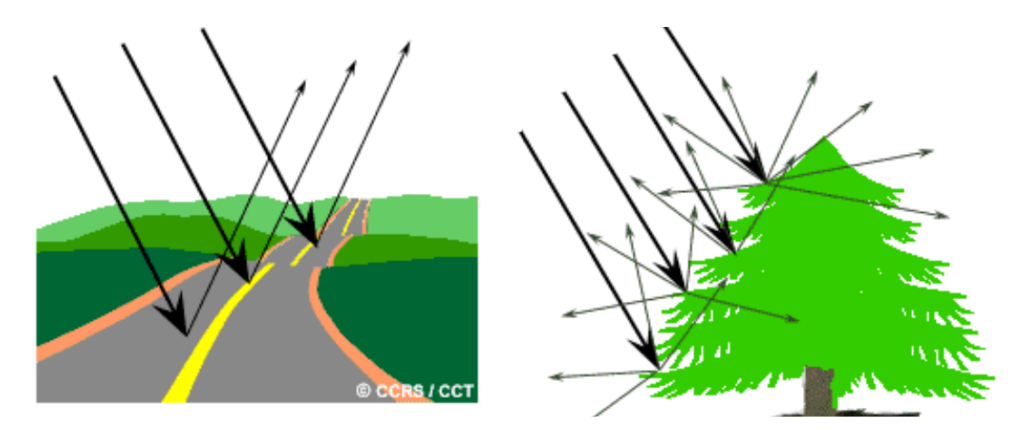


Figure 2.6 Two different types of radiation reflection; specular reflection (left) and diffuse reflection (right)

Depending on the target roughness and the incoming radiation wavelength, surface features mostly lie somewhere in the perfectly specular, perfectly diffuse reflectors or somewhere in between. This means that, once the wavelengths are considerably smaller than the surface properties variations or the dimension of the pieces that form the surface, the diffuse reflection would dominate. The interactions of some of the targets surface feature with incoming radiations at the visible and infrared wavelengths can be explained through some examples. For instance, in vegetation when chlorophyll pigment (a chemical compound that provides energy for photosynthesis with the absorption of light) is maximum at plants in summer, leaves appear greenest, and when the chlorophyll is less in autumn leaves appear red or yellow. This is due to that in summer, the chlorophyll strongly holds radiation in the red and blue wavelengths but reflects green wavelengths, whereas there is excessive green radiation absorption in autumn because of the less chlorophyll in the leaves and therefore, more reflection of the red wavelengths occurs. If the internal structure of leaves is healthy then leaves act as perfectly diffuse reflectors to the near-infrared wavelengths. Hence, as a one way to determine how healthy vegetation is the measuring of the near-infrared reflectance. Water as another example is the strong reflector of shorter visible wavelengths (e.g. blue) and absorbs radiation with longer wavelengths (e.g. near-infrared). Since water reflects radiation in the blue wavelength, it usually looks blue or blue-green but darker if observed at red or near-infrared wavelengths. Figure 2.7 shows the interactions of different visible and infrared wavelengths with vegetation leaves and water.

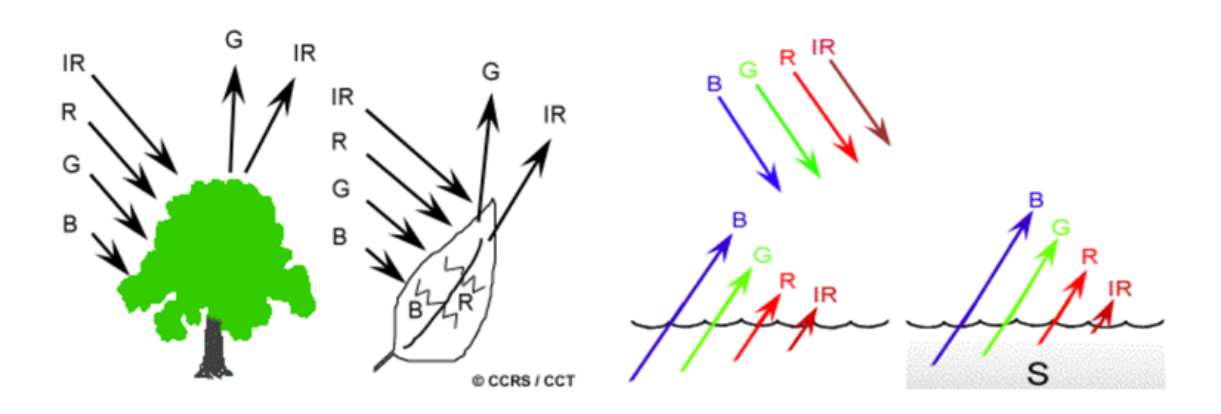


Figure 2.7 Visible and infrared wavelengths interactions with vegetation leaves (left) and water (right)

However, the existence of algae in the water can make confusion in terms of reflection because the chlorophyll in algae causes to reflects radiation in the green and absorbs more of the blue wavelengths and, making the water look greener in color. Moreover, water surface characteristics such as water surface roughness, suspended materials

and oil spills, due to their different reflection properties, therefore, can also make the water-related interpretation more complicated. Accordingly, to indicate spectral responses for the different objects over a variety of different wavelengths and to correctly evaluate the interaction of the surface properties with electromagnetic radiation, knowing the factors which influence the spectral response is critical. Therefore, a spectral response for the specific target can be build up by measuring the reflected (or emitted) amount of electromagnetic energy by the targets over a variety of different wavelengths. Figure 2.8 illustrates the vegetation and water spectral response at different wavelengths.

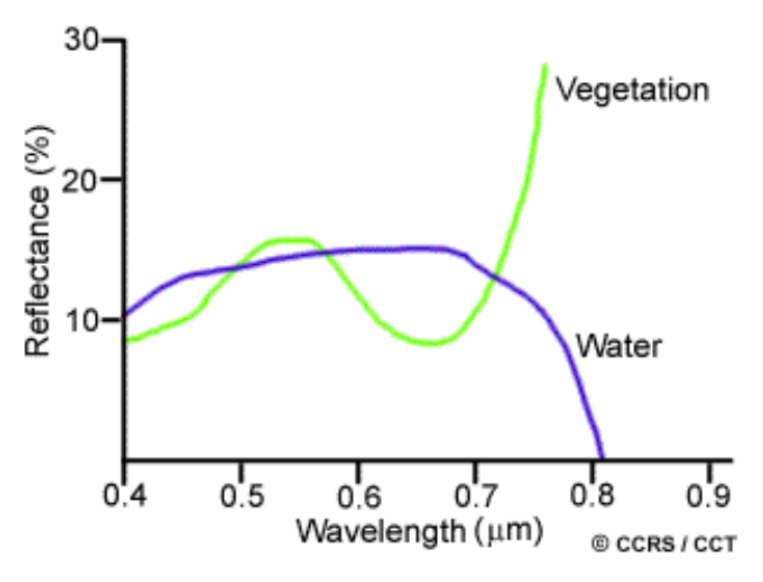


Figure 2.8 Spectral responses of the vegetation and water over a variety of different wavelengths

2.2 Microwave Remote Sensing Systems

This remote sensing system uses the long-wavelength radiation region of the electromagnetic spectrum and measures the microwave portion of the EMS which is ranging from approximately 1 mm to 1 m in wavelength of the spectrum. Microwave frequency is ranging from 0.3 GHz to 300 GHz corresponding to the 1 mm to 1 m in wavelength, respectively (Figure 2.9). Microwave sensors are typically active remote sensing systems that detect and record echos (backscatters) reflected from transmitted microwave radiation incident upon the features on the surface [73]. In compare to the active microwave remote sensing system, passive sensor utilizes a broad range of microwave radiation. The microwave bandwidths are commonly known as the K, X, C, L and P bands that are employed the microwave band ranges in the active microwave sensors (Figure 2.10) [72]. In order to proceed active microwave, the sensor integrates several pieces of microwave equipment for imaging (i.e. SAR sensor)

and non-imaging including radars (RAdio Detection And Ranging), scatterometer, and altimeter. Radar sensor transmits a signal (microwave radio) upon the target and records the backscattered part of the signal. The round trip time delay between the signals (transmitted and reflected pulses) defines the distance (or range) to the object and therefore, the intensity (which is related to the surface characteristics and incidence angle) of the backscattered signal is measured to separate different targets on the ground. SAR as an imaging sensor is used for measuring and imaging the surface variations in microwave backscattered signal such as surface roughness and surface moisture. Non-imaging scatterometers are used to detect variations in a wide range area, for example, estimating ocean wind speed by measuring the variations in the surface roughness. The elevation of the earth's surface is measured by the altimeters that are fixed below the platform viewing the ground straight down at nadir. In fact, non-imaging microwave sensors are one linear dimension profiling devices while imaging sensors take measurements in two-dimensional.

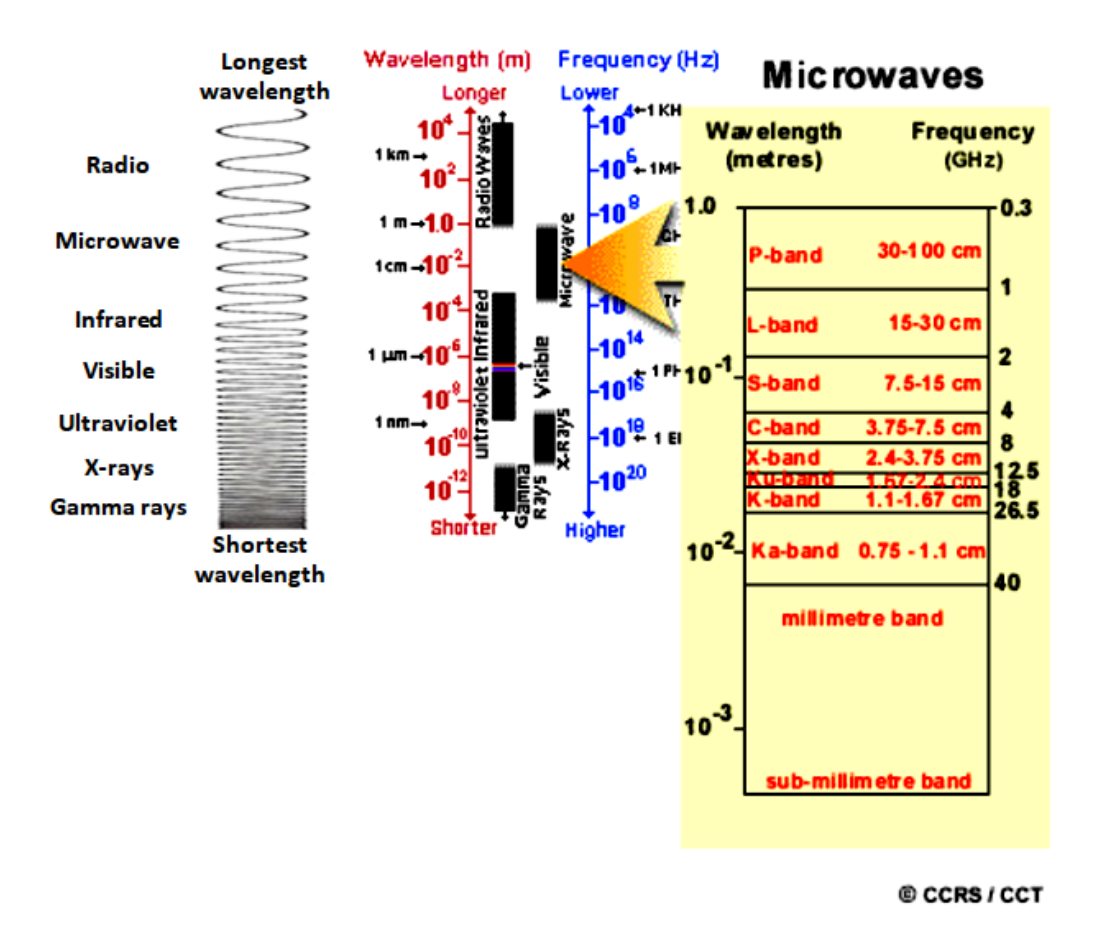


Figure 2.9 Parts of the electromagnetic spectrum

Given that active microwave remote sensing carrying its own energy source and independent of the sun as source of illumination and hence, can be operated day-or-night. In addition, microwave radiations with long wavelengths are not prone

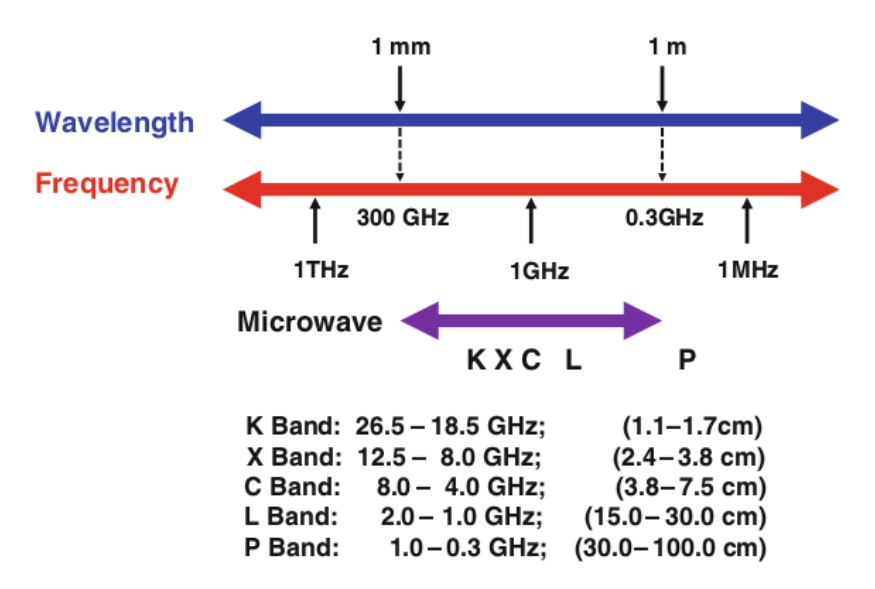


Figure 2.10 Microwave bandwidth ranges and specifications [72]

to atmospheric scattering and therefore, enables radar pulses to penetrate through cloud cover, haze, smoke, dust, and all rainy climate but the heavy rainfall [5]. Consequently, These properties of microwave energy allow collecting data at any time, different weather and environmental conditions.

The focus of this thesis is solely on imaging radar active microwave remote sensing systems. The basic principles of Synthetic Aperture Radar (SAR), Polarimetric SAR and Interferometric SAR is discussed in the next chapter.

Radar Bachground

3.1 Synthetic Aperture Radar

Imaging radar can be generally divided into two distinct categories: Side Looking Aperture Radar or Side Looking Radar (SLAR or SLR) and Synthetic Aperture Radar (SAR). SLAR radar is the classical radar system that is well-known as Real Aperture Radar (RAR) with a real aperture antenna (a physical antenna) in limited length. The SLR imaging system is equipped to a straight lengthy antenna mounted on the aircraft or satellite platform that its longitudinal axis parallel to the flight direction. Parallel direction to the flight track is called the azimuth direction (along-track) and the direction of the radar Line-Of-Sight (LOS) is called the range direction (across-track). Detail of the imaging geometry of the side-looking monostatic radar in a straight flight line over the flat terrain at altitude H is illustrated in Figure 3.1. The radar platform is on motion with velocity ν , and the radar antenna emits microwave energy pulses perpendicularly to the platform flight direction and towards to the targets on the ground. The pulses after reaching to the ground and depending on the targets characteristics are scattered usually in different directions as well as the direction of the antenna. The return pulses (the backscattered echoes) are received by the antenna at different times based on the distance between the antenna and different objects on the ground and the recorded backscatters of the echoes are used in the construction of the radar image. Radar is basically a ranging device that measures range (distance) to targets located within the beam footprint [74]. In any microwave remote sensing systems, a transmitter, an antenna, a receiver, and a recorder are basic devices in the configuration of the radar sensors. The size of the antenna is the principle for the footprint (beam width) and therefore, for the radar imagery resolution. The ground resolution of a real aperture SLAR system (i.e. spatial resolution; range and azimuth resolution) is related to the slant range and azimuth direction which depending on the length (aperture length) and the antenna beamwidth and is defined as the capability of the device to differentiate between two objects on the ground [75]. The slant range and range resolution of a RAR are displayed in Figure 3.2 and Figure 3.3, respectively.

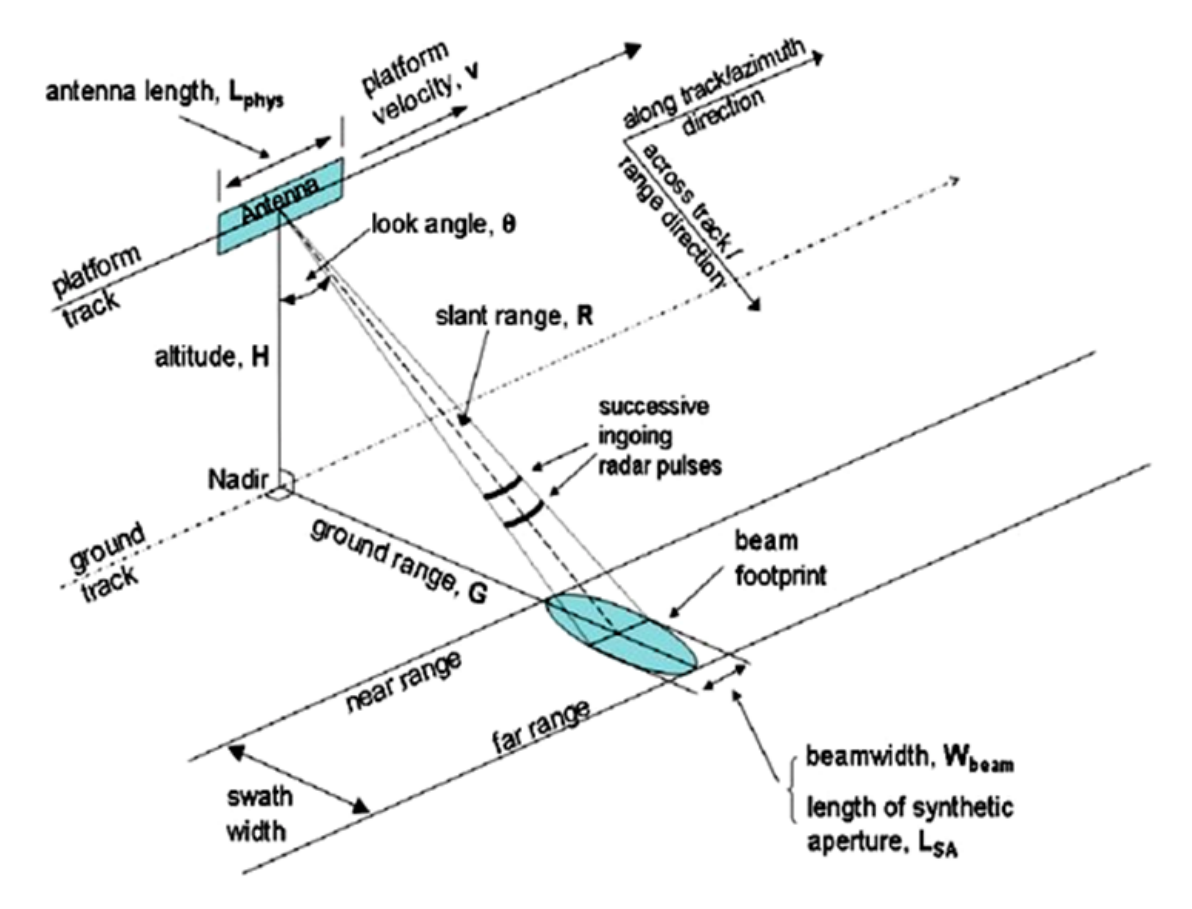


Figure 3.1 Geometry of RAR, side looking aperture radar [74]

The ground range resolution of a RAR is assigned as $\rho_{\rm g}$ in Figure 3.3 and is given as equation 3.1.

$$\rho_g = \frac{c\tau_p}{2\sin\theta} \tag{3.1}$$

Where τ_p is indicates the pulse length and c is the speed of light. In fact, the range resolution is based on the pulse width and look angle but it is independent from the height. The coefficient of two is related to the round-trip of the radar pulse (sent out from and return to the radar). Since there are practical limits on peak transmitter energy and, in practice, the radar pulses cannot be made short arbitrarily thus, sufficient microwave energy required to be delivered to lightening the target in order to gain the needed Signal-to-Noise-Ratio (SNR). Therefore the maximum transmitter energy and required SNR determine the length of the pulse [74]. Azimuth resolution which is parallel to the flight direction of the platform is defined by the minimum distance on the ground in which two objects can be separately imaged. Hence, two objects at the same slant range can be distinguished only if they are not at the same time in the radar beam. Thus, the azimuth resolution (ρ_a) can be written as equation 3.2, where the θ_H the angular spread of the radar beam in the azimuth

direction is equal to wavelength (λ) divided by antenna length (l).

$$\rho_a = R\theta_H = \frac{R\lambda}{l} \tag{3.2}$$

There is an inverse proportional between the footprint and the size of the antenna, thereby the longer antenna has a narrow footprint and hence, high spatial resolution in azimuth direction. The resolution in terms of the slant range is defined with the distance that two objects on the ground have to be away from each other to give two different waves (echoes) in the return signal to avoid overlap of the incoming signals. This means that if two objects (e.g. A and B objects in Figure 3.2) are separated by at least half a pulse length then they can break down in the range direction.

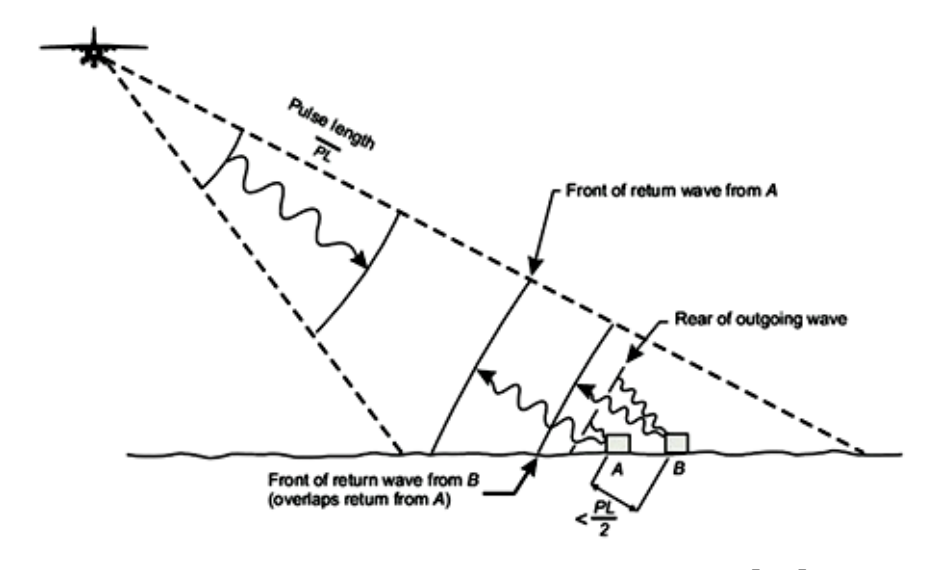


Figure 3.2 Exemplification of the slant range [76]

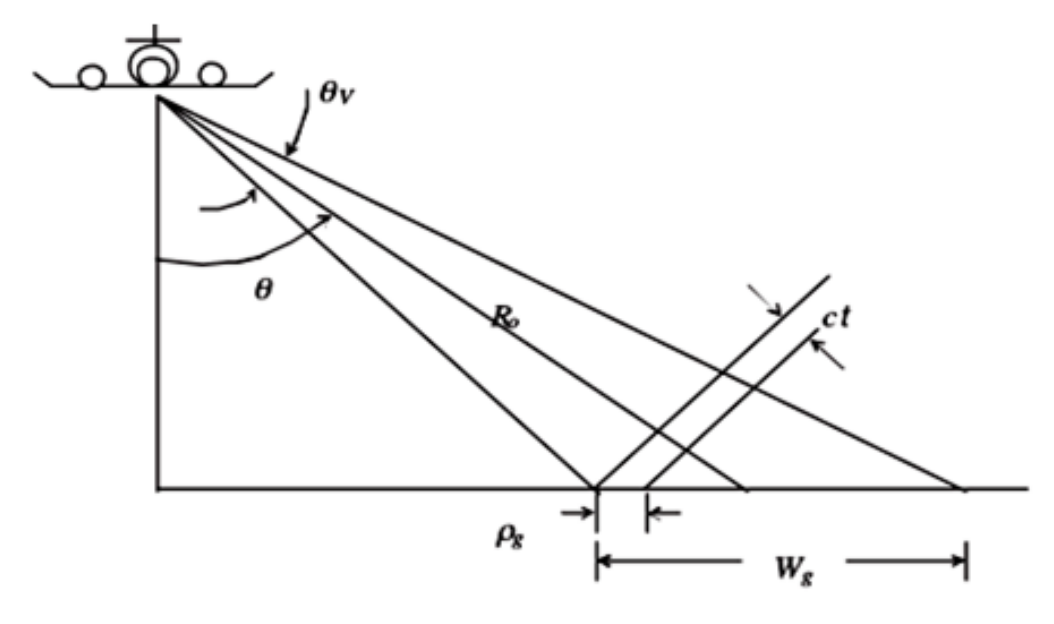


Figure 3.3 RAR range resolution [75]

The interaction between the several components of the radar imaging system is that the transmitter generates the microwave energy and transmits the energy to the antenna from where it is emitted upon to the target. After the energy hits and interacts with the target, the receiver accepts the backscattered energy (signal) as received by the antenna, and the received signal is filtering and amplifying by the receiver as it required for recording and the recorder then stores the signal [76]. Radar imaging principles and the systematic interactions between its components is shown in Figure 3.4.

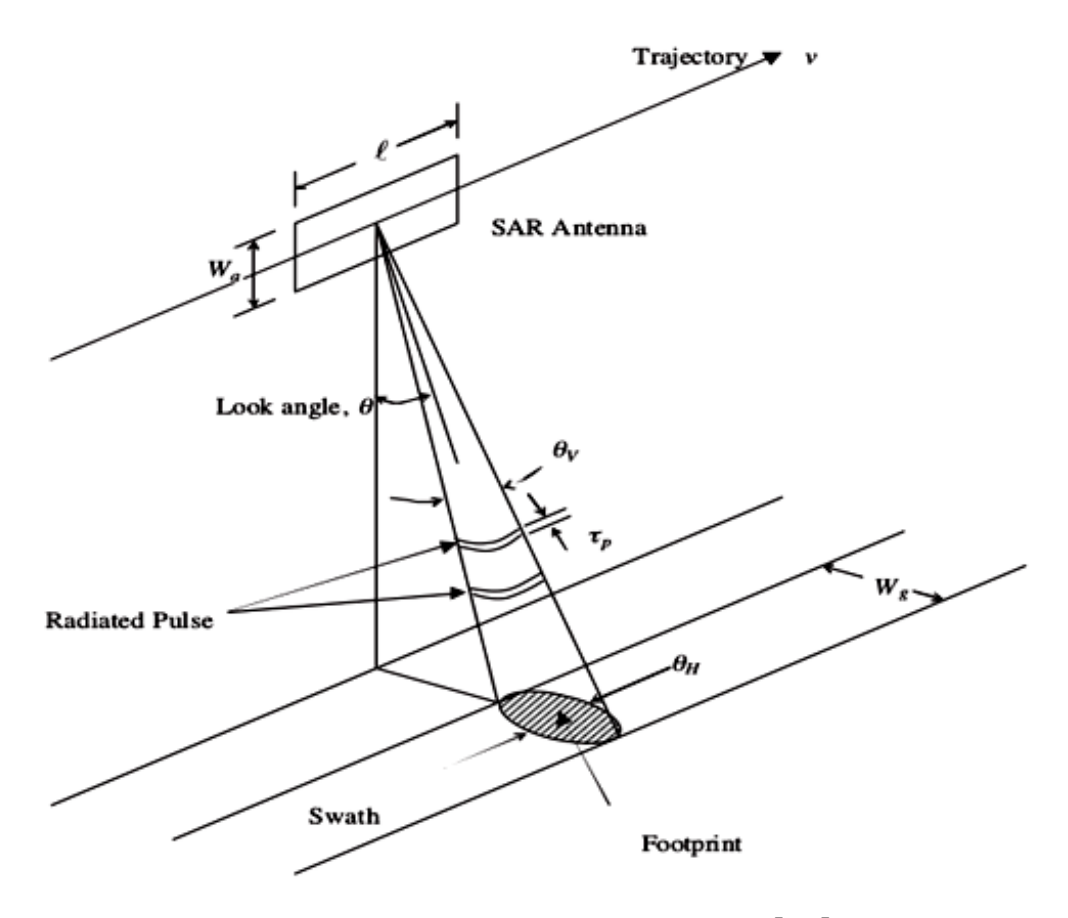


Figure 3.4 Geometry of imaging radar [75]

Given that it is not feasible for a RAR system platform (aircraft or spacecraft) to carry a very long physical antenna which is required for getting useful and high spatial resolution imaging of the earth surface, therefore, SAR was developed to overcome this limitation of the RAR system and thus, to improve spatial resolution with synthesizing the large antenna from the small antenna (RAR real antenna) by taking advantages of the motion of the platform to emulate a longer antenna [76]. As shown in the Figure 3.5, SAR principally, operates by simulating long antennae and this virtual implication is achieved through the Doppler effect that allows the small real antennae with a limited beam width (D) to forward microwave beams at different time intervals along with the beamwidth [72]. During the time that radar transmits the microwave

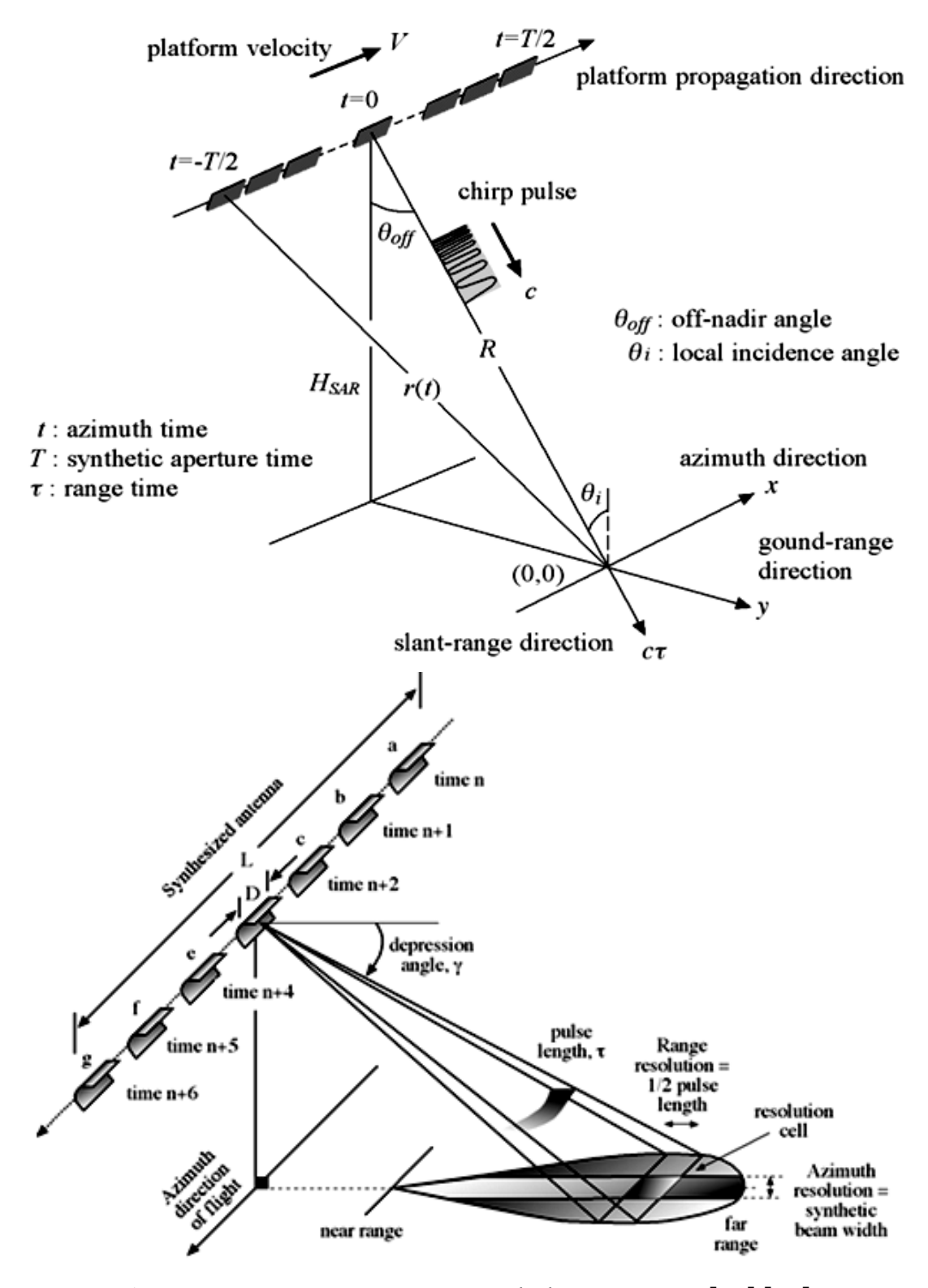


Figure 3.5 SAR system geometry with the parameters [77] [78]

signals to the object, SAR continues to receive the return pulses. Meanwhile with the movement of the platform the relative distance between the radar and the object changes which causes a Doppler effect to dampen a chirp modulation of the received return pulses.

In the imaging radar, due to the earth's rotation and because of the radar moves along its flight direction the relative speed between the radar and each scatterer changes, hence, the Doppler frequency shift corresponding to each point scatterer on the ground is different, and this causes the received signals to have a fading characteristic. Therefore, Doppler frequency shifts can more easily be perceived when applying higher frequency due to that the proportion of frequency shift would be larger. However, there would be a slight angle called the squint angle, ωs of the radar platform [79]. Thus, the Doppler frequency for a specific target, based on the squint angle and platform speed Vs (the sensor-target velocity), and look angle can be written as equation 3.4.

$$f_D = \frac{2\nu_s}{\lambda} \sin \omega_s \sin \theta \tag{3.3}$$

When the sensor is in the closest position to the target and the center frequency of the sequence of a target through the radar beam is in zero Doppler position ((i.e. t=0) it is called the Doppler centroid frequency. It is assumed that the Doppler frequency first is positive in zero Doppler position and decreases down to zero, and then becomes increasingly negative as the movement of the frequency of the sequence of a target through the antenna beam. The changes of the Doppler frequency composes the Doppler bandwidth B_{Dop} , where β_a is the azimuth beamwidth of the antenna and the ν_s is the relative speed of the platform and is given by the equation 3.5.

$$B_{Dop} = \frac{2\beta_a \nu_s}{\lambda} \tag{3.4}$$

The total Doppler frequency turn is from -v/L to v/L, thus describing the Doppler bandwidth as the following equation.

$$\Delta f_D = \frac{2\nu}{I} \tag{3.5}$$

The resolution in the azimuth direction of a SAR focused image related to Doppler bandwidth and the relative speed of the platform is shown in equation 3.6.

$$\Delta A_g = \frac{v_s}{B_{Dop}} = \frac{l}{2} \tag{3.6}$$

Therefore, the azimuth resolution of a SAR is only a function of the length of the

physical antenna and not depend on imaging distance or wavelength. In order to increase the azimuth resolution of azimuth direction, a matched filter proportional to the reverse characteristics of chirp modulation called azimuth compression is intended as shown Figure 3.6. On the Doppler frequency shift assessment, it is considered that the Doppler shift when the target is moving away from the radar system is negative (opening range) and when the target is moving toward the radar it is positive (closing range).

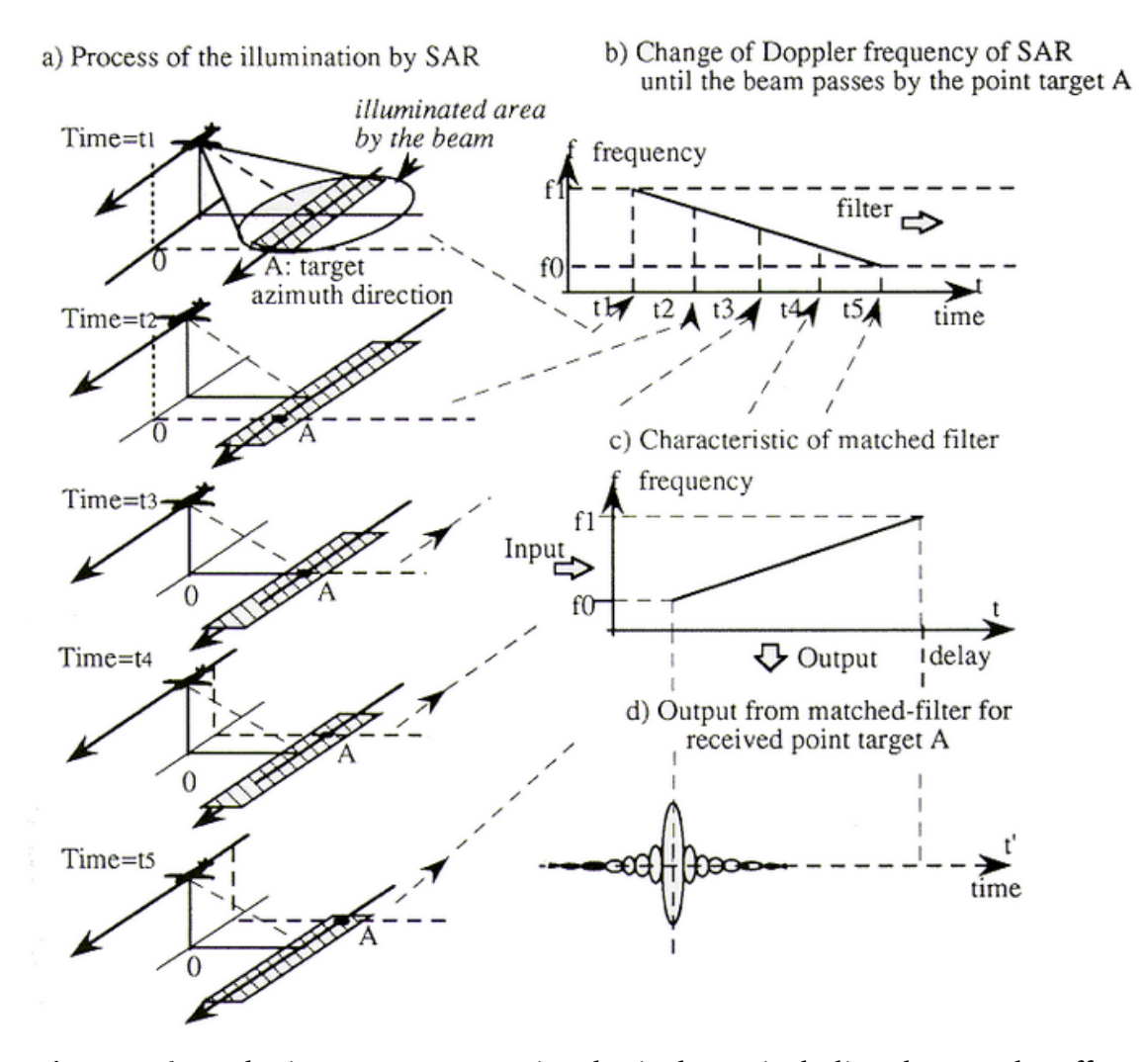


Figure 3.6 Synthetic aperture processing, basic theory including the Doppler effect, matched filter, and azimuth compression [80]

An image acquired by the radar contains a digital number for each pixel which indicates the strength of the received backscattered energy from the ground. The received energy from the each transmitted radar signal can be represented by the physical parameters and illumination geometry using radar equation as shown in equation 3.7 [81]. The bistatic radar equation is extracted as with monostatic radar (transmitter and receiver is at the same platform) and solely the grouping of terms is different.

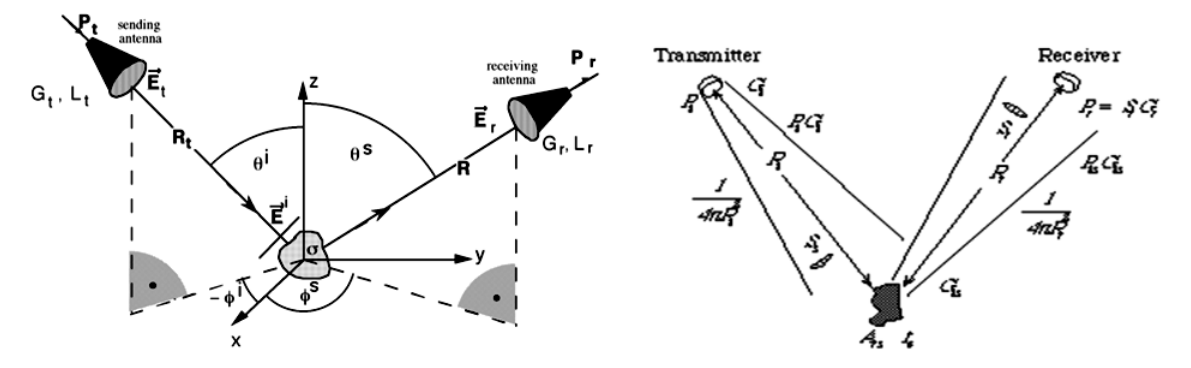


Figure 3.7 Radar Transmission scheme and coordinate system [82] [83]

$$P_{R} = P_{T}G_{T} \cdot \frac{1}{4\pi R_{T}^{2}} \cdot \sigma_{B} \cdot \frac{1}{4\pi R_{T}^{2}} \cdot \frac{\lambda^{2}}{4\pi} G_{R}$$

$$= P_{T} \cdot \frac{G_{T}G_{R}\lambda^{2}}{(4\pi)^{3}R_{T}^{2}R_{R}^{2}} \sigma_{B}$$
(3.7)

Where

 P_R = received energy,

 P_T = transmitted energy,

 R_T = distance from the transmitter to the object,

 R_R = distance from the receiver to the object,

 G_T = transmitter gain,

 G_R = receiver gain,

 λ = wavelength,

R = range from the sensor to the object, and

 σ_B = bistatic Radar Cross Section (RCS) of the target and it is depending on the target properties and the extent of the illuminated terrain.

In fact, the radar equation demonstrates the basic relationship between the radar system parameters, the received energy, and the target's characteristic [82]. Measurement of the intensity of the received signal is the critical objective made by the radar that allows various subjects are differentiated in microwave remote sensing systems. Accordingly, measuring the angle and distance to a target is made by recording the arrival time of the received signals to discriminate among different targets. For distributed targets with the bistatic radar equation 3.7 can be extended by integrating the backscattered energy over the illuminated terrain surface and modified it as equation 3.8.

$$P_R = P_T \int_{A_{iii}} \left(\frac{G_{ant}^2 \lambda^2}{(4\pi)^3 R^4} \right) \sigma^0 dA$$
 (3.8)

Where (A_{ill}) is the illuminated surface area, G_{ant} is the radar antenna gain and σ^0 is the unitless backscattering coefficient that indicates the return backscattered per unit surface area. The radar equation can be used to estimate the energy backscattered by the target if the characteristics of the radar system and the imaging geometry are specified. The intensity of the backscattered radar turn back from the pointlike target is described by the RCS (σ) through the equation 3.7 (radar equation) in the units of area (m^2) . In general, RCS mostly depends on the shape of the scatterer, its dielectric constant, imaging geometry (orientation of the scatterer), and the used wavelength than the size of the object in the real-world [84]. Similar to the RCS, the proportion of the backscattered energy compared with the incident energy on the scene for distributed targets obtained from equation 3.7, is described by the backscattering coefficient which is unitless and normalized by the illuminated surface area using the incidence angle θ_i , assumed in flat terrain and can be expressed by equation 3.9.

$$\sigma^0 = \frac{\beta_0}{\sin \theta_i} \tag{3.9}$$

Where β_0 is the estimated backscattered energy (brightness estimate) aquired by the radar in slant-range geometry that is not related the incidence angle and local topography [85]. However, if the local terrain topography is recognized for normalize the backscattered energy properly, the local incidence angle $\theta_{i,local}$, should be used in equation 3.9. According to the published works recommendation, the σ^0 is used only in connection with calibrated radar systems [84]. The σ^0 is often represented in *decibels* and is given as equation 3.10.

$$\sigma_{dB}^0 = 10\log_{10}(\sigma^0) \tag{3.10}$$

Because of the normalisation of σ and σ^0 the backscattering coefficient in decibels σ^0_{dB} properly defines the orientation of the scattering which 0 dB refers to isotropic scattering, positive and negative values to scattering are representing that energy focuses towards or away from the radar respectively.

3.2 Radar image distortions

SAR imaging with the side-looking viewing geometry is achieved by sweeping the ground through the antennae in an orthogonal direction to the platform flight direction (azimuth direction). The sweeping width is a function of the magnitude of the off-nadir angle. Radar is measuring the distance to targets in slant range rather than the ground range (real lateral distance) along the ground thus slant-range distortion appeared which causes variations in scale (caused by slant range to ground

range conversion) that change from near to far range in the image [86]. Therefore, due to the terrain elevation, SAR images in the natural coordinates (range and azimuth) is limited by the presence of geometric distortions (caused by slant range to ground range conversion) inherent to the range imaging mode. Figure 3.8 illustrates the SAR geometry in the plane perpendicular to the azimuth track with a side-looking antenna that illuminates the planarity (ground range plane) area in slant range directions. A constant resolution (Δy) on the ground range corresponding to a constant resolution (Δr) in the slant range direction of a target within the near and far range can be derived from the equation 3.11.

$$\Delta y = \frac{\Delta r}{\sin \vartheta} \tag{3.11}$$

Where the incidence ϑ angle variation from near to far range causes to reduce the ground range resolution Δy ; meaning that features in the near range are compressed with regard to the features at far range. These results also are relevant to the ground range pixel (resolution cell) dimension. Similarly to the distortions encountered in

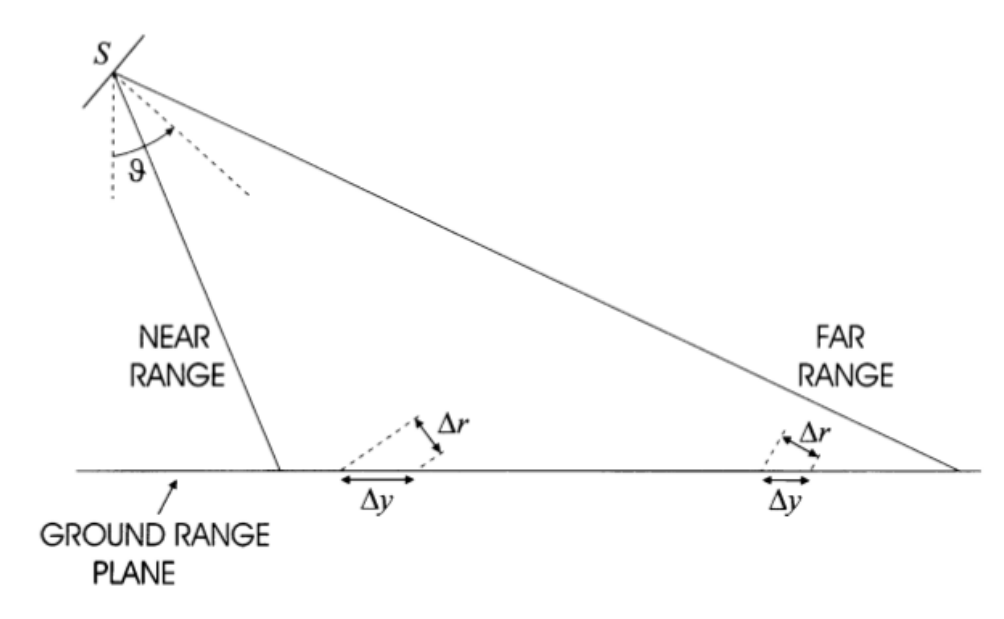


Figure 3.8 SAR geometry in the plane indicating slant range versus ground range resolutions [80]

the planar area, radar imagery are also exposure to geometric distortions due to relief displacement. In considering the effects of the surface slope α , the resolution of the ground is determined by the local incidence angle $\vartheta_i = \vartheta$ - α and related to the terrain topography on the slant range direction of radar. *foreshortening*, *layover* and *shadows* are three consequences that are resulted from relief displacement as depicted in Figure 3.9. As previously mentioned radar measures distance in slant range, and hence, foreshortening that depends on the angle that surface slope makes in relation to the incidence angle, is responsible to the dilation or compression of the

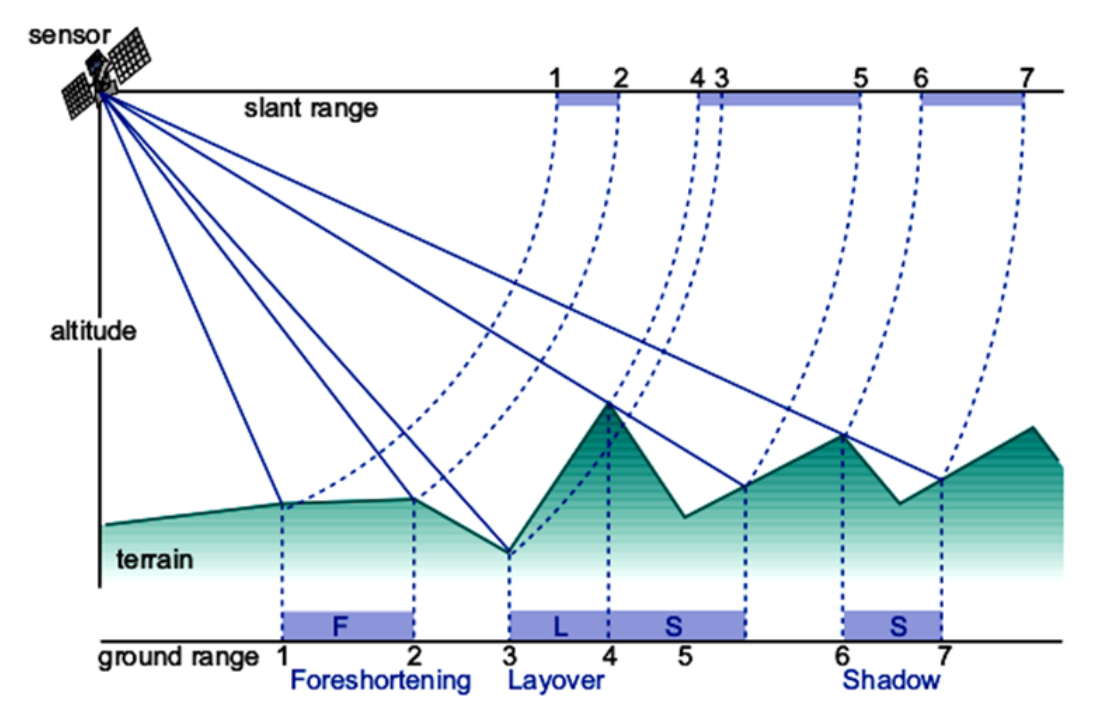


Figure 3.9 Geometric distortions in radar images due to relief displacement [76]

pixel in the radar image with respect to the radar beam with the slope on the ground. Different foreshortening effects in terms of slant range and slop ($-\vartheta < \alpha < \vartheta$) are shown in Figures 3.10 to 3.13. foreshortening occurs when the radar beam hits the base of

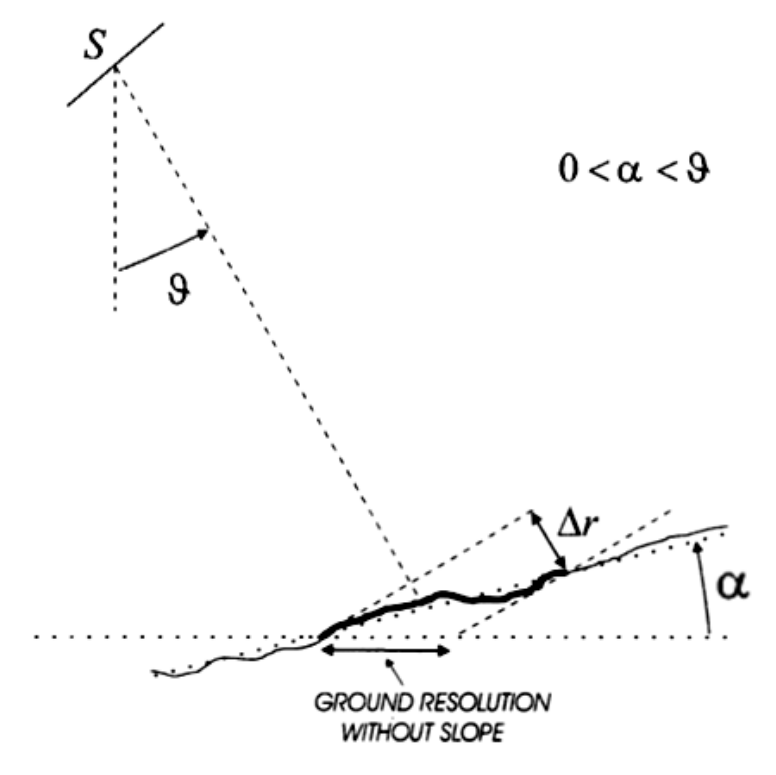


Figure 3.10 Foreshortening effect when $0 < \alpha < \vartheta$, where the pixel on the ground is highlighted [80]

tall features (e.g. hills or mountains) and back towards the radar before it arrives at the peak. When the radar beam is orthogonal to the slope such that the slope, the base, and the peak are imaged simultaneously, then maximum foreshortening occurs. The slopes in the mountainous terrain with intensive foreshortening effects appear as bright features on the image and therefore, the length of the slope not represented correctly. Layover happens when the radar beam hits the peak of a hill

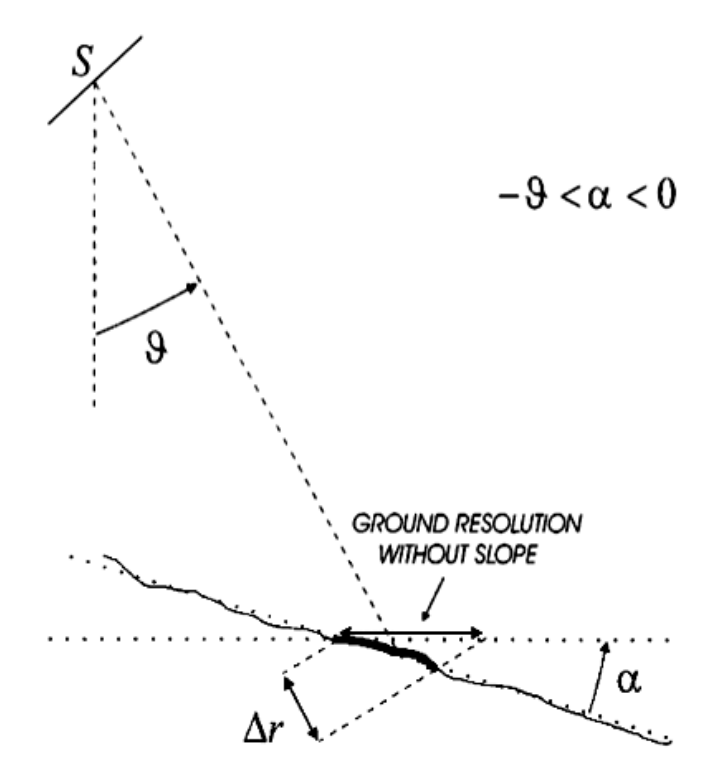


Figure 3.11 Foreshortening effect when $-\vartheta < \alpha < 0$, where the pixel on the ground is highlighted [80]

or mountain before it arrives at the base, where the return pulse from the peak of the hill or mountain is received before the pulse from the bottom and resulting to the compression of the area with the slope into a single pixel in the radar image. It causes where the incidence angle is smaller than the slope angle In the image it appears bright features. This is similar to what happens in foreshortening but layover is extremely severe for small incidence angles in the near range and in very steep slope mountainous. In the case of, targets in the valley have a larger slant range than related mountain peak, then the foreslope is "reversed" in the slant range image and therefore, the ordering of surface features in the radar image is the inverse with the ordering on the ground.

Radar shadow results from foreshortening and layover. In the case, that radar beam is not able to illuminate the surface and the region does not generate any backscattered signal thus radar shadow occurs and behind vertical features or slopes with steep sides appear dark in the radar image due to the absence of the backscattered energy.

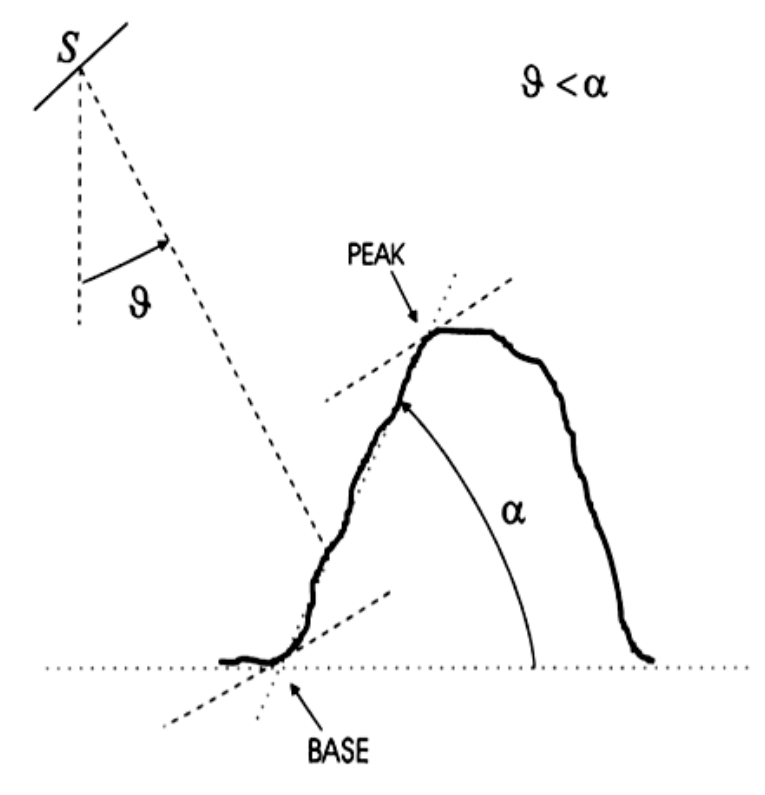


Figure 3.12 Layover effect when $\vartheta < \alpha$ [80]

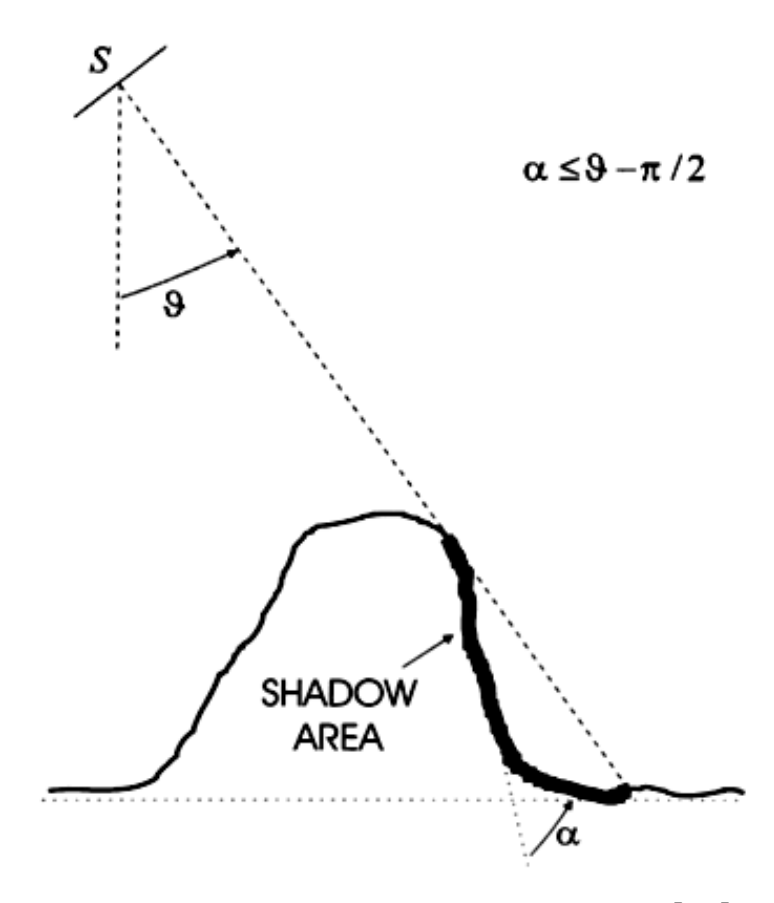


Figure 3.13 Shadow effect when $\alpha + \vartheta > 90$ [80]

Besides its characteristic slant range geometry, radiometric distortion is also subjects of the side-looking SAR sensor which is related to the spectral anomalies arise from the sensor itself imaging geometry (non-systematic errors). As backscattered energy is received in the slant-range, therefore, the collected energy coming from a slope facing the sensor is recorded in a diminished space in the image, meaning that it is compressed into fewer image pixels than should be the case if acquired in-ground range geometry [76]. Because the obtained energy from different features is combined thus this results in high digital numbers and hence, the slops projecting the radar appear extremely bright. Therefore, it is essential to correct SAR images geometrically and radiometrically so that the pixel values truly and directly represent the radar backscatter of the reflecting surface. For proper interpretation of the images, due to the inherent radar geometry and radiometric distortions, a postprocessing step is necessary to generate SAR images with uniform and earth-fixed grids to represent the images in a standard map projection, for example, the Universal Transverse Mercator (UTM). Thereby, the images are corrected and transformed into ground range geometry that is usually referred to as geocoding. SAR images also have inherent salt and pepper like texturing called *speckle-effect* nose, due to the hardware or the erratic radiation from other sources (constructive and destructive interference) resulting in dark and bright pixels in the image. The quality of the image decreases with the appearance of speckle noise and the interpretation of the features be more difficult. To reduce speckle nose effects either multilook processing or spatial filtering can be applied.

3.3 Microwave polarizations

An electromagnetic wave polarization in the field of radar remote sensing applications has a substantial function. In respect to the direction of the transmitted and received microwave signal, different backscattering values and consequently different radar images resulting from it. In fact, radar systems are capable to transmit the EM wave horizontally and receive it again horizontally (HH), vertical transmission and vertical reception (VV) and cross-polarized transmit and receive (HV or VH). In respect to the direction of the transmitted and received microwave signal, different backscattering values, and consequently different radar images result. The principles of the transmitted and received radar wave in the linear (horizontal-vertical) combination of two perpendicular fields are shown in Figure 3.14. Accordingly, a wave strikes, out of $+\infty$ (orientation of propagation z), on a target, then the incident electric field registers as a superposition of two linear, orthogonal polarized waves in the linear reference system. The polarization transformation state represented in terms of *polarization ellipse*, [87]. It describes a curve, which the real part of the electrical field

vector passes through if either the position of the propagation orientation is held steady and the time runs or the time is held constant and the position of propagation direction changes [76]. Figure 3.15 illustrates the direction of propagation a wave

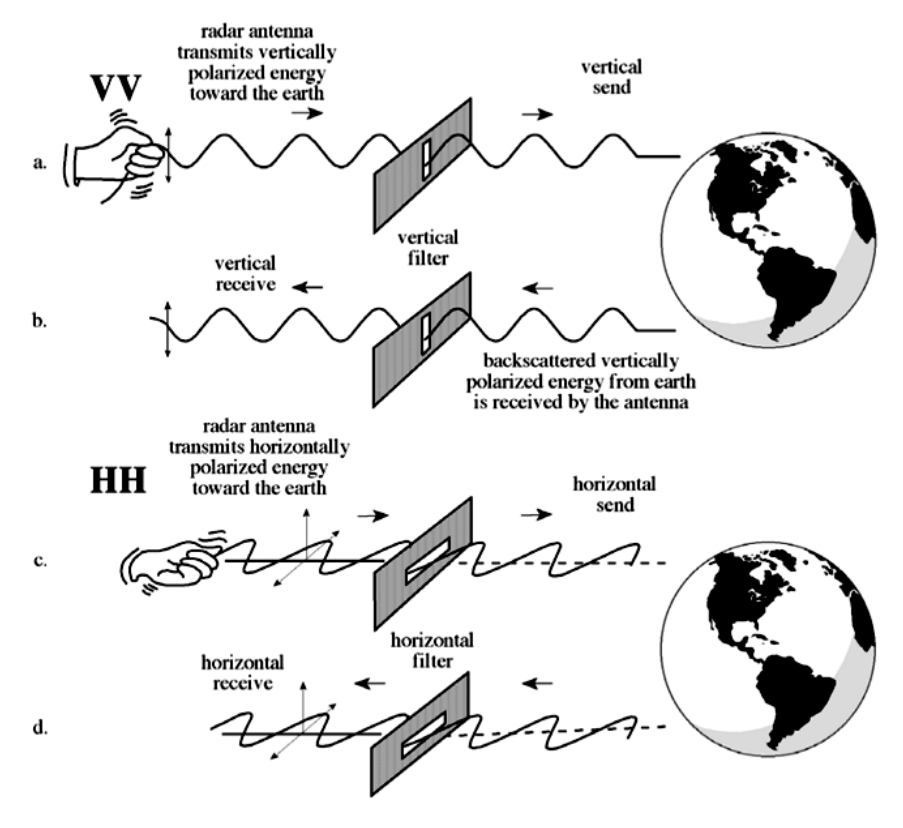


Figure 3.14 Schematic of polarization pulse traveling from the radar and wave interactions [88]

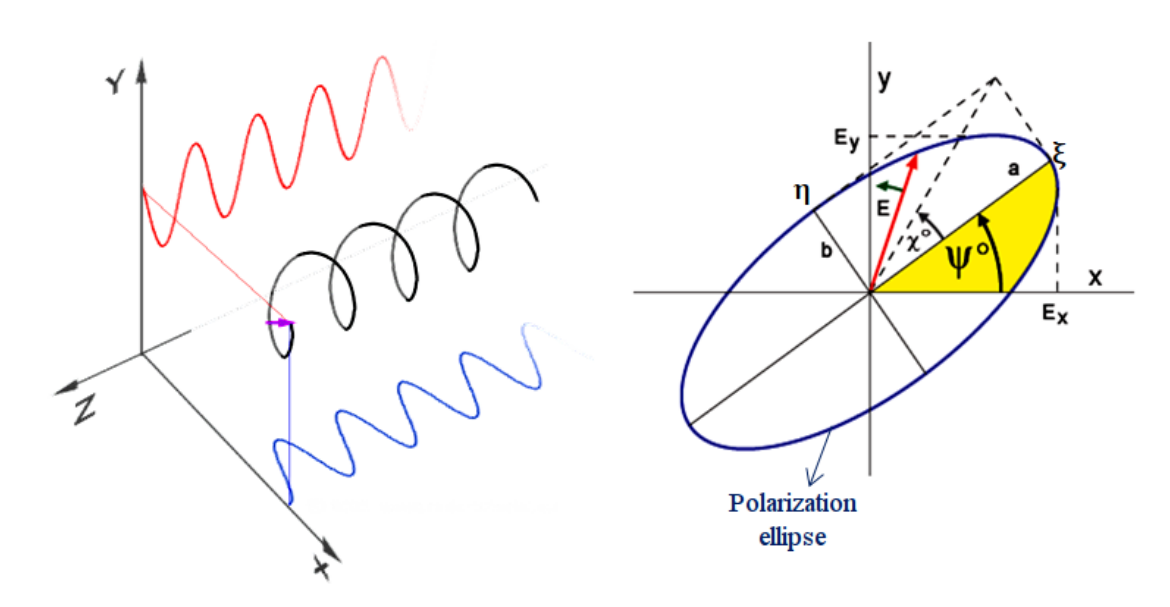


Figure 3.15 EM wave polarization represented in combination of two orthogonal electric fields and direction of propagation a wave with a circularly polarized wave (left) and polarization ellipse (right)[87]

in electric fields with a circularly polarized wave as a sum of two linearly polarized

elements 90° out of phase and polarization ellipse. The orientation angle (ψ) and the ellipticity angle (χ) are two angular parameters that the polarization ellipse can be represented. The EM wave is fully determined by the parameters of its electric vector $\vec{E}(\vec{r},t)$ including magnitude, phase, and direction given by equation 3.12.

$$\vec{E}(\vec{r},t) = E_x \vec{x} + E_y \vec{y} \tag{3.12}$$

Where (\vec{E}) is corresponding components of the real vector Real (\vec{E}) and $\vec{r}(x, y, z)$ is related to the position of a vector that illuminated of a point in the space by the wave characterized by the wave vector [89].

3.4 Radar data formats

The primary obtained SAR data are in a raw data format which their spatial resolution depending on the radar system imaging characteristics. Raw data include the backscatter of targets on the ground viewed at different points in the sensor trajectory. The received backscatter signals from the targets are sampled and separated into two components including information about the amplitude and the phase of the detected signal are stored in different layers, together forming a *complex number*. Different products derived from the raw data such as intensity images, geocoded images, and phase-containing data are generated after being processed with a SAR processor. Based on each pixel's range and unique Doppler shift information the raw data are compressed meaning that many backscatters of a point are merged into one pixel in complex format which has information of the returned microwave. It should be noted that the highest possible spatial resolution for compressed data is still maintained. For each pixel, the phase and amplitude information is calculated from the complex number.

When all backscattered information (both phase and amplitude) of a point is used in the compression, then the *Single Look Complex (SLC)* format data is the output data. In the case of multi-look processing, the whole range of the orbit in that an object can be seen is separated into multiple components which each component provides a look at the object. With making an average of these multiple looks, the output image that acquired is a *Multi-look* image that is still in complex format but with reduced spatial resolution. However, multiple looks averaging also reduces the effects of the speckle-noise in the image. In order to produce an image to use for visual interpretations, the SLC or Multi-look data require to be processed to change the complex format into the *Intensity* image. The number of looks that are used in the compression step, has a direct effect on the spatial resolution of the intensity image.

3.5 Radar signal and object interactions

The received energy rate by the radar antenna is a function of the illuminating signal strength and the characteristics of the illuminated object [76]. The transmitted energy rate for illuminating the object on the ground is related to the surface characteristics of the illuminated object such as surface roughness, shape, orientation, and dielectric constant. On the other hand, illuminating signal (microwave energy) strength which is in relation to radar system parameters such as wavelength, polarization, and imaging geometry vary depending on the sensor types which has been explained in previous sections. Surface roughness is the terrestrial property that most strongly influenced the intensity of the radar backscatters such that a smaller scale also affects radar return pulses. It is inferred by the wavelength of the radar (usually between 5 and 40 cm) comparable with textural elements such as leaves and twigs of vegetation, gravel, and sand. In terms of the radar wave interactions, a distinction needs to be taken between the surface roughness and topographic relief. Surface roughness happens in the radar wavelength range and between centimeters to decimetres while this range is between meters to kilometers that topographic relief takes place [76]. A smooth surface acts as a mirror (specular scattering), reflecting the radar wave at an angle equal and opposite to the incidence angle which causes that the energy reflected away from the sensor and thus a smooth surface appears black in the SAR image due to the no signal return to the radar antenna. A surface is considered smooth with the Rayleigh roughness criteria as written in below.

$$h = \frac{\lambda}{8\sin\eta} \tag{3.13}$$

Where h is mean height of surface roughness feature, λ is radar wavelength and η is incidence angle [90]. The electrical properties of surface materials is measured by the the complex dielectric constant which is related to the reflectivity of the microwave consist of two part including permittivity and conductivity of a medium [91]. These two properties are strongly related to the moisture or liquid water content of a medium (e.g. soil moisture) in which an object with high dielectric coefficient has a strong surface reflection. The distinguish of the two surfaces with equal roughness and the equal radar return intensity for two surfaces, is detected by the difference in their dielectric properties. Radar backscatter depends also on to the orientation of the target relative to the radar antenna and also the local incidence angle. Natural surfaces (e.g. vegetation canopy, forested area, grasses, variable soil surface, etc.) which are composed of different mediums are generally inhomogeneous and thereby usually depending on the wavelength of the radar and the permittivity of the media, resulted in both *surface scattering* and *volume scattering*. Usually the high backscatter is caused by the corner reflection (e.g. the dihedral corner reflector) in point objects with

limited size (manmade features, such as buildings, transmission towers, trunk of trees) which gives a very strong radar return. The interactions of radar waves with the point objects resulted *double bounced scattering*. Different radar backscatter behaviours over the various objects on the ground is depicted on the Figure 3.16.

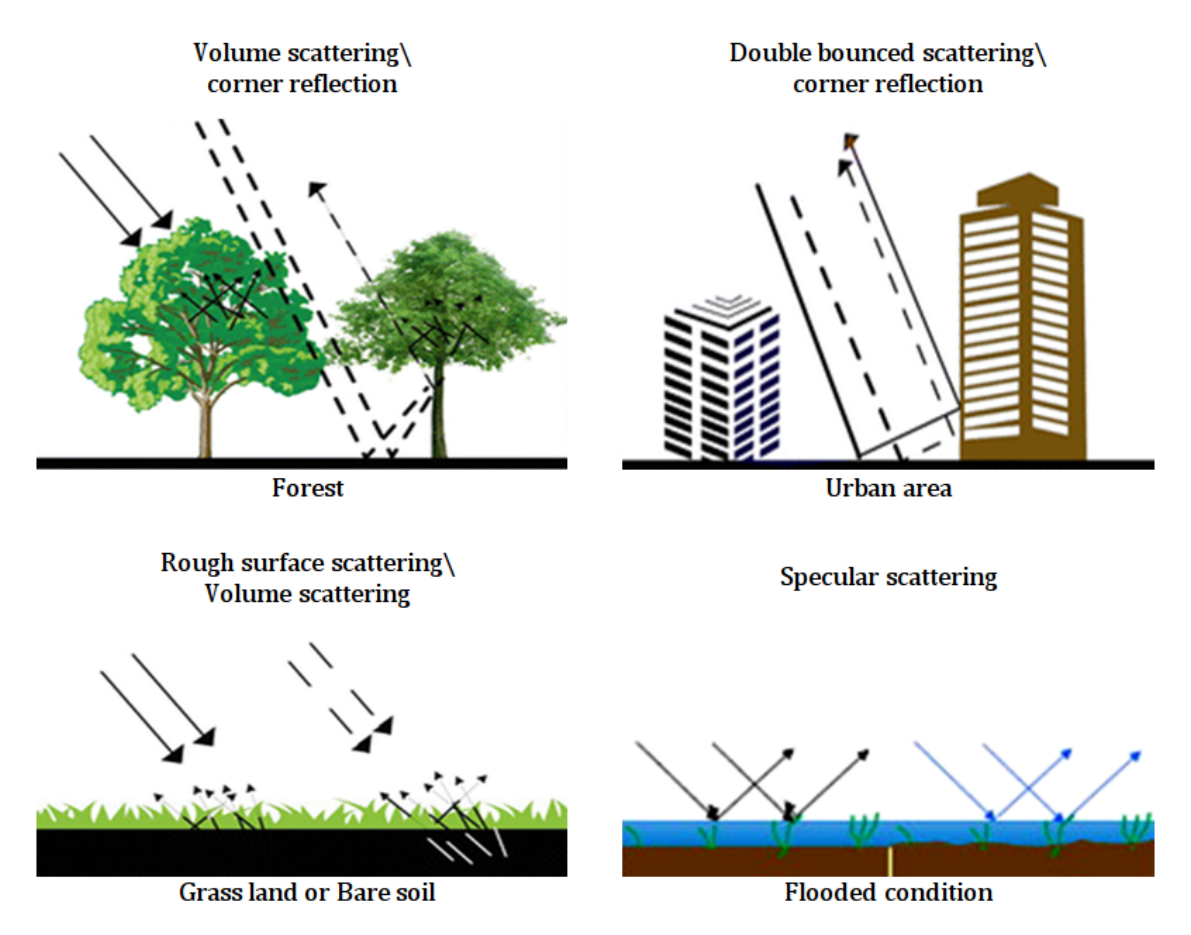


Figure 3.16 Schematic illustrations of radar wave backscatter over various surface cover conditions [92]

3.6 Historical Background

SAR system first operational time is believed to be the X-band (3 cm wavelength) sensor built in 1957 by Willow Run Laboratories of the University of Michigan for the U.S. Department of Defense. NASA started to support the development of SAR systems for civilian programs. The SEASAT-A developed by Environmental Research Institute of Michigan (ERIM) and Jet Propulsion Laboratory (JPL) convinced NASA in 1978 to launch it as the earliest earth based radar remote sensing satellite that was included an L-band (23cm wavelength) SAR sensor [80]. Although, The SEASAT-A operational time was short and limited to 100 days due to damage occurred in the system, the achieved results significantly shown the importance of the SAR system. NASA approved the Shuttle Imaging Radar (SIR) series following the SEASAT-A

mission and in years 1981 and 1984 the SIR-A and SIR-B series were launched respectively. The L-band SIR space shuttles designed for monitoring of glacial movements, oceanography and terrestrial analysis applications. The first S-band SAR satellite was launched in 1987 by the former Soviet Union called as spacecraft Cosmos 1870. The ALMAZ-1, second S-band HH-polarized satellite with 15 m ground resolution was launched in 1991. Same year European Space Agency (ESA) launched first European Remote Sensing satellite (ERS-1) with C-band (5.6 cm wavelength) VV-polarized sensor and aim for 10 years data acquisitions. In 1992 the first Japanese Earth Resources Satellite (JERS-1) L-band HH-polarized satellite was launched with 6 years operational mission until 1998.

In 1994 a four-polarization C-band and L-band system that has been integrated with an X-band SIR-C sensor jointly developed by Germany and Italy. So far the SIR-C/X-SAR was representing a unique spaceborne sensor due to its capabilities of simultaneously acquire different bands and polarizations. ERS-2 was as a second mission which overlapped with the ERS-1, and was launched in 1995. TANDEM orbit mission, was offered to compose and the joint use of the two sensors (ERS-1and ERS-2) which allowed a repeat orbit of the sensor with 1 day temporal baseline, and therefore, this approach was provided different opportunities such as repeat pass SAR interferometry. Canada Space Agency (CSA) in 1995, operated Radarsat-1, a multimode C-band HH polarization satellite. NASA's Shuttle Radar Topography Mission (SRTM) that in 2000 was released, used C and X band to compose Digital Elevation Model (DEM) outfitted with two radar antennas with 60 m baseline between. The SRTM was designed to moved the temporal decorrelation of repeat pass satellites and hence to implement a single pass interferometry.

ESA was launched the Environmental Satellite (ENVISAT) in 2002, to study on earth as land, ocean and atmosphere with ten different equipments. Japan, following the JERS-1 and in 2006, has launched the second L-band equipped satellite called the Advanced Land Observing Satellite (ALOS). In 2007 the other SAR new generation satellites including COSMO-SkyMed in 8th of June, TerraSAR-X in June 15th, and Radarsat-2 in the 14th of December were launched. The Italian COSMO-SkyMed satellite series provides very short temporal baseline due to the constellation of the four satellites equipped with X-band SAR sensor. The German TerraSAR-X satellite has X-band and an 11 day revisit time. Canadian C-band Radarsat-2 satellite has left and right looking operation systems. Since 2012 the SEOSAR/PAZ as an X-band SAR satellite, is based on the TerraSAR-X platform operated by Spanish Earth Observation Program as a dual-use (civil/defense) mission. ESA, in 2014 and 2016 has been launched Sentinel-1 (Sentinel-1A/B) as a constellation of two satellites orbiting 180° apart with the main goals of land and ocean monitoring and also to provide C-band

SAR data continuity following the retirement of the ERS-2 and end of the Envisat mission. Sentinel-1 offers dual-polarized (HH+HV, VV+VH) products with a different spatial resolution (down to 5 m) and coverage (up to 400 km) and high temporal resolution (6 days repeat frequency) in four exclusive imaging operational mode which enables to map the entire world (land and ocean). The expected operational life of each SENTINEL-1 satellite to transmit earth observation data is at least 7 years and have fuel on-board for 12 years. ESA has ensured the continuation of the Sentinel-1 by ordering two more radar satellites i.e. Sentinel-1 C and -1D that will be launched from 2021 onwards to extend the operational monitoring at least until the end of 2030.

4 Interferometric SAR

Interferometry is a procedure enables precise quantitative measurements of the terrain heights and is among the principal applications of the SAR technology which is typically represented by the SAR interferometry (InSAR) technique [93, 94]. It essentially relies on the ability to measure the phase difference of radar waves in interactions with a scattering objects from different passes made with the same sensor, or even from different sensors and/or at a different time interval. InSAR technique can be employed either to represent variations in height to generate a Digital Elevation Model (DEM), referred as InSAR-DEM or an interferogram of the ground topography and/or to obtain very accurate terrain surface height (sub-centimeter) changes information (surface deformation) after the events (e.g. earthquake or volcanic activity). InSAR is categorized into two groups as Cross-Track-InSAR (CT-InSAR) and Along-Track-InSAR (AT-InSAR) depending on the measurable quantities (Figure 4.1). Repeat-pass CT-InSAR (also known as two-pass CT-InSAR) including DInSAR

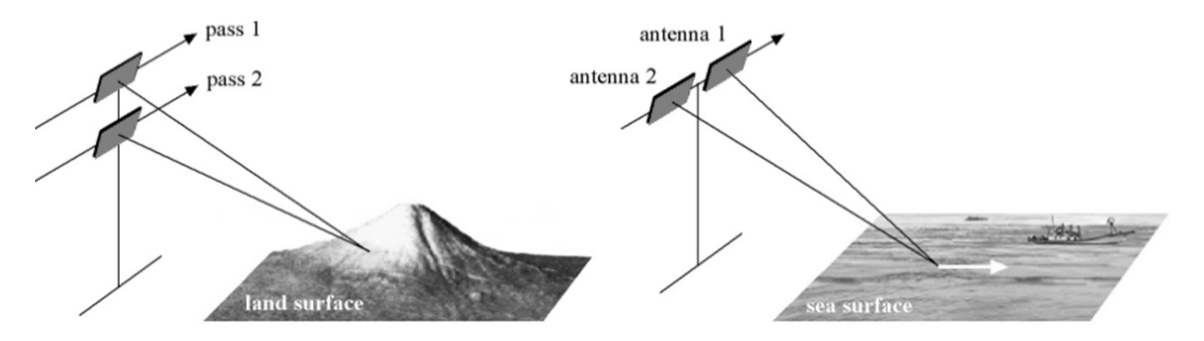


Figure 4.1 Geometry of repeat-pass CT-InSAR (left) and AT-InSAR (right) [77]

(Differential InSAR), in which a single antenna forming two complex images (SLC images) of the same area on land in different times and/or passes and a complex interferogram is generated by multiplying of the first complex image (i.e. typically referred to as master image) and the complex conjugate of the second image (i.e., the so-called slave image). Hence, from the measuring of the exact phase variation between the two backscatters within an accuracy of the sequence of the wavelength (i.e., centimeters) and also with the knowledge of the precise position of the antennas

with respect to the earth's surface from Global Navigation Satellite Systems (GNSS) and the position of the pixel including its elevation the difference in the path length can be estimated [72]. Figure 4.2 shows the repeat-pass interferometry and the configuration of the InSAR geometry. In the AT-InSAR system a complex interferogram is produced by using a satellite outfitted with two radar antennas with 60 m baseline in between (e.g. SRTM sensor) by implementing single-pass interferometry. The produced interferogram includes the interferometric phase, ψ (InSAR phase) and coherence information (InSAR coherence). In addition to the radar wavelength and antenna separation, the InSAR phase ψ also depends on the ground-range distance and surface elevation. The ψ that depends on the ground-range distance is referred to as the orbital or the flat phase and the relevant interferometric fringes are termed as the orbital fringes. The ψ that related to the surface elevation is the topographic phase to produce topographic fringes. In order to estimate the topographic phase, the flat phase should be removed from the ψ . Since for computing the complex interferogram, the complex conjugate of the second image is used then InSAR phase ψ is folded or "wrapped" about $(0,2\pi]$ at each 2π and therefore, ψ is so-called the wrapped phase and the unwrapped phase ϕ is subjected as the true phase, absolute phase [77].

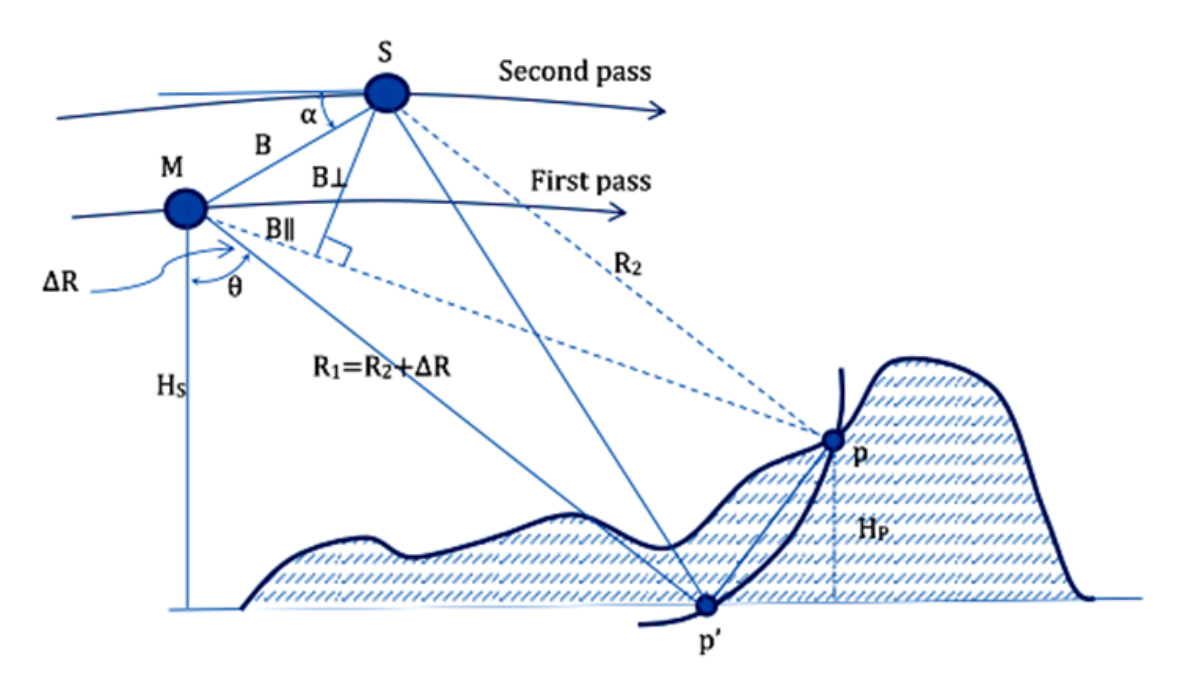


Figure 4.2 Configuration of the InSAR geometry [95]

The complex pixel (C_p) value which is calculating from the two complex images and the phase difference (ϕ) are expressed by the equations 4.1 and 4.2, respectively.

$$C_p = A_1 A_2 \cos \phi + i \sin \phi = A_{12} e^{i\phi}$$
 (4.1)

$$\phi = \phi \, 1 - \phi \, 2 = -\frac{4\pi}{\lambda} \Delta R \tag{4.2}$$

Where A_1 , A_2 and $\phi 1$, $\phi 2$ respectively, are representing amplitude and phase components of two SAR images for the same pixel, ΔR is the range difference of two SAR observations (displacement in the Line Of Sight (LOS)), the orientation angle of the baseline (B) is α . Regarding that ΔR can not be derived directly from the geometry because of the orbital inaccuracies and also the 2π phase ambiguity (because of the atmospheric condition changes between the two radar observations), thus ΔR can be expressed through the equation 4.3 and 4.4 and thereby, the target height H_p can be written as equation 4.5.

$$(R_1 + \Delta R)^2 = R_1^2 + B^2 + 2R_1 B \sin \theta - \alpha \tag{4.3}$$

$$\Delta R \approx B \sin(\theta - \alpha) \tag{4.4}$$

$$H_p = H - R_1 \cos \theta \tag{4.5}$$

Therefore, Interferometric phase $(\Delta \varphi)$ is influenced by four factors consist of topographical distortions caused by slightly different imaging angles of the two sensors directions (t) atmospheric impacts (α) resulting in the wavelength distortions, any range displacement of the radar target (ΔR) , and decorrelation effects (noise). Among these four contributions, the decorrelation effects when the noise amount is low are negligible and due to the local topography is accurately compensated (errors in the DEM) the phase contribution is also negligible and therefore $\Delta \varphi$ can be simplified as equation 4.6.

$$\Delta \varphi = \frac{4\pi}{\lambda} \Delta R + \alpha \tag{4.6}$$

5 Methodology

5.1 Polarimetric SAR Backscatter

Several studies on the processing of radar data indicate that the phenological stages of the plant have an effect on the backscatter of the signal, and there is a significant correlation between the biophysical parameters of the plants, including height, leaf area index, vegetation mass, plant water content, and radar signal backscatter [50, 58, 96]. Radar backscattering from vegetation is a function of both wavelengths polarization and frequency. Different frequencies and polarizations enable one to infer various and supplementary information from the single object. In agricultural radar applications, combination of polarizations (co-polarization and cross-polarization) allows analyst to extract extra information about crop characteristics. The polarization of backscattering microwaves indicates the target structural properties and visualizes scattering characteristics of observed features [35, 97]. A majority of the space borne radar systems often transmit only one polarization and receives both polarization giving rise to dual polarimetric SAR data (e.g., Sentinel-1 with VH and VV polarizations), while some collecting full polarimetric so-called quad polarization (HH, VV, HV, and VH) imagery (e.g., PALSAR, TerraSAR-X, and RADARSAT-2). Fully polarimetric SAR data is acquired using the H and V polarizations which extracted from SLC data and can be represented by a 2×2 scattering matrix S (Equation 5.1) including polarimetric information for each individual resolution cell [98, 99].

$$S = \begin{bmatrix} S_{HH} & S_{HV} \\ S_{VH} & S_{VV} \end{bmatrix}$$
 (5.1)

Scattering matrix which depends on incident and the scattered field, has four components, each representing the received and transmitted polarizations [100, 101]. The scattering matrix consists of information on the nature and characteristic of the observed media and features. Full polarimetric SAR data set which is described as scattering matrix is foundation for several coherent polarimetric decomposition and analysis. For polarimetric analysis an alternative procedure is derived from a

covariance matrix (C_3) that represents the average polarimetric information extracted from a set of neighboring pixels to produce the mean polarimetric response. The covariance matrix C_3 , (Equation (5.2)), is determined from the outer element of the vector form of the scattering matrix with its Hermitian conjugate, K_C [57, 102]. The averaged target vector (covariance matrix) for fully polarimetric data is given by Equation 5.3.

$$C_{3} = K_{C}.K_{C}^{*T} = \begin{bmatrix} C_{11} & C_{12} & C_{13} \\ C_{21} & C_{22} & C_{23} \\ C_{31} & C_{32} & C_{33} \end{bmatrix},$$

$$\langle C \rangle_{full} = \langle S(i)S(i)^{H} \rangle,$$

$$= \begin{bmatrix} \langle S_{HH}S_{HH}^{*} \rangle & \langle S_{HH}S_{HV}^{*} \rangle & \langle S_{HH}S_{VV}^{*} \rangle \\ \langle S_{VH}S_{HH}^{*} \rangle & \langle S_{HV}S_{HV}^{*} \rangle & \langle S_{VH}S_{VV}^{*} \rangle \\ \langle S_{VV}S_{HH}^{*} \rangle & \langle S_{VV}S_{VH}^{*} \rangle & \langle S_{VV}S_{VV}^{*} \rangle \end{bmatrix}$$
(5.2)

$$= \begin{bmatrix} \left| S_{HH} \right|^{2} & \sqrt{2}S_{HH}S_{HV}^{*} & S_{HH}S_{VV}^{*} \\ \sqrt{2}S_{HV}S_{HH}^{*} & 2\left| S_{HV} \right|^{2} & \sqrt{2}S_{HV}S_{VV}^{*} \\ S_{VV}S_{HH}^{*} & 2S_{HV}(S_{HV} - S_{VV})^{*} & \left| S_{VV} \right|^{2} \end{bmatrix}$$
 (5.3)

Where ensemble averaging is shown by the | | represents the modulus, the * indicates complex conjugation and the complex conjugate transpose shown by superscript H. For natural targets, in case and transmitted polarization $(r, t \in \{h, v\})$ for horizontal and vertical polarization and the scattering matrix is defined by three-element complex target vector, $K_C = \left[S_{HH}\sqrt{2}S_{HV}S_{VV}\right]^T$, where superscript T indicates the matrix transpose [100, 101]. In the covariance matrix, diagonal elements $(C_{11} = \sigma_{HH}^0)$, $C_{22} = \sigma_{HV}^0$), and $C_{33} = \sigma_{VV}^0$) define backscattering coefficients and the upper or lower triangular components represent complex numbers. The backscattering coefficients have correlation with the structural characteristics of the features [57, 103].

In comparison to the quad polarization, dual polarimetric SAR sensors collect a fraction of total (precisely half of the scattering matrix components) polarimetric information involved in fully polarimetric imagery [102]. It means that each resolution cell at each time point is defined by a 2×2 covariance matrix (C_2) that is obtained from C_3 . The resulting covariance matrix which is for dual polarization

(e.g., Sentinel-1) is represented by Equation 5.4.

$$C_{2} = \begin{bmatrix} C_{11} & C_{12} \\ C_{21} & C_{22} \end{bmatrix},$$

$$\langle C \rangle_{dual} = \begin{bmatrix} \langle S_{VV} S_{VV}^{*} \rangle & \langle S_{VV} S_{VH}^{*} \rangle \\ \langle S_{VH} S_{VV}^{*} \rangle & \langle S_{VH} S_{VH}^{*} \rangle \end{bmatrix}$$

$$(5.4)$$

Since dual polarization has only diagonal elements, the matrix with off-diagonal components are set to zero and do not follow a complex Wishart distribution; however, the two diagonal blocks (1 by 1) do [101, 104].

Polarimetric Synthetic Aperture Radar (PolSAR) technique has resulted many different investigations and improvements in crop growth monitoring, yield estimation, crop disaster prediction and prevention and in more general terms providing accurate information for precision farming. PolSAR products, such as Entropy (H), Alpha (α) and Anisotropy (A) decompositions are calculated from the covariance matrix. The H- α -A decompositions are used to extract average parameters from experimental data suggested by Cloude and Pottier [105]. This approach is based on second-order statistics using a smoothing algorithm [106]. Natural measure of the inherent reversibility of the backscattering data is defined by entropy (H), and indicates the randomness of the scatter, while the underlying average scattering mechanisms, scattering type (surface, double-bounce and volume scattering) can be identified using Alpha parameters. The relative power the second and third eigenvectors is described by Anisotropy (A), which represents being of different properties in different directions when measured along different axes [105, 107]. The Entropy (H) decomposition parameter has more sensitivity to the crop parameters and the density and randomness of some vegetation canopy than Alpha and Anisotropy [99, 108].

In agricultural radar monitoring, Radar Vegetation Index (RVI) is a method for observation of the level of the vegetation growth in time series data analysis as an alternative to NDVI (Normalized Difference Vegetation Index) method used in optical image processing studies [109]. Ranging between 0 and 1, RVI is used for measuring the randomness of scattering in microwave signal [110]. It is close to 0 for a smooth bare surface and as vegetation grows the value increases till the crop reaches to the end of growth cycle and it is affected by vegetation water content and sensitive to the biomass [111]. RVI calculation needs quad-polarized data, thus for full polarization, RVI is retrieved by the Equation 5.5.

$$RVI = \frac{8\sigma_{HV}^{0}}{\sigma_{HH}^{0} + \sigma_{VV}^{0} + 2\sigma_{HV}^{0}}$$
 (5.5)

where σ_{HH}^0 and σ_{VV}^0 are co-polarized backscattering coefficients and σ_{HV}^0 is cross-polarized backscattering coefficient in power units. According to the Charbonneau et al. [112] the assumption that supposes $\sigma_{HH}^0 \approx \sigma_{VV}^0$ then Equation 5.5 can be reduced to the form as Equation 5.6.

$$RVI_{HH} = \frac{4\sigma_{HV}^{0}}{\sigma_{HH}^{0} + \sigma_{HV}^{0}}$$
 (5.6)

Melanie et al. [113] studied the RVI and concluded that RVI_{HH} is useful when just two polarizations are available and can be an appropriate approximation of the surface scattering if the interaction between the surface plane and vegetation is insignificant. Since Sentinel-1 is dual polarization and has VH and VV polarizations, following Charbonneau et al. [112] assumption of possibility to modification of RVI in case of availability of two polarizations we assume an alternative to RVI for dual polarization as shown in Equation 5.7.

$$RVI = \frac{4\sigma_{VH}^0}{\sigma_{VV}^0 + \sigma_{VH}^0} \tag{5.7}$$

5.2 Interferometric Coherence

A digital SAR image is consist of rows and columns of small picture elements called pixels and each pixel is representing a small area of the earth's surface known as a resolution cell. Each pixel is achieved by summing the complex numbers along a constant range which contains amplitude (the strength of the reflected signal) and phase (the position of a point in time on a waveform cycle) information about the microwave reflected signals toward the satellite antenna by the objects (scatterers) such as rocks, vegetation and buildings within the corresponding resolution cell projected onto the surface of the earth. Coherence, as a complex quantity and its absolute value, is considered as a critical analytical parameter which provides a useful measure of the interferogram quality (SNR: signal-to-noise ratio) and evaluating the quality of the two complex SAR images [114–118]. To obtain Interferometric synthetic aperture radar (InSAR) coherence image and interferogram generation it's necessary to input Single Look Complex (SLC) image pair referred to as 'master' and 'slave' that are focused complex SAR data in full resolution and that preserve both amplitude and phase information for each pixel. Equation 5.8 indicates the general expression of the SLC image [119].

$$C(x) = A(x)e^{i\phi(x)} \tag{5.8}$$

Where C(x) (a complex value) is represented by A(x) amplitude, and e Euler's number of exponential function wherein i is an imaginary number and equals to $\sqrt{-1}$ and $\phi(x)$ is phase. Since SLC image is composed of a regular grid, then x can be replaced by (ρ, a) which ρ is the range and a is the azimuth. Equation 5.8 can be replaced with Equation 5.9 [119].

$$C(\rho, a) = A(\rho, a)e^{i\phi(\rho, a)}$$
(5.9)

The complex interferogram is the product of two registered SLC images acquired at different times and consists of backscatter amplitude and phase differences between the acquisitions. The complex interferogram is achieved by pixel-by-pixel cross-multiplication of the first the image with the complex conjugate of the second [80, 94, 120, 121] and it can be written as Equation 5.10 [119, 122].

$$C_2C_1^* = A_1A_2e^{i(\phi_2-\phi_1)} = R(\rho, a) + I(\rho, a)$$
 (5.10)

Where C_1 and C_2 are refer to the master (the reference) and slave (the repeat) SLC images, A1 and A2 are master and slave amplitudes and ϕ_1 and ϕ_2 are master and slave phases, respectively. The asterisk (*) denotes complex conjugation. R is the real and I represents the imaginary component of the complex interferogram. As it can be inferred from the Equation 5.10, that the amplitude multiplication of the first and second images produces the interferogram amplitude whereas the interferometric phase is the phase difference between the images [118]. The phase of the interferogram is extracted in usual manner and can be expressed as Equation 5.11.

$$(\phi_2 - \phi_1) = \tan^{-1} \left(\frac{I}{R}\right)$$
 (5.11)

Considering complex SAR image pair that contain both amplitude and phase information, the correlation between the two radar complex signals can be evaluated by calculating the interferometric phase noise. In fact, the coherence is the cross-correlation coefficient of an InSAR pair estimated over a small window with a specific size (a few pixels in range and azimuth) [123, 124]. The interferometric coherence (γ) between two complex co-registered images can be defined as Equation 5.12 [125].

$$\gamma = \frac{\left| \langle C_1 C_2^* \rangle \right|}{\sqrt{\left(\langle C_1 C_1^* \rangle \langle C_2 C_2^* \rangle \right)}} \tag{5.12}$$

Where | | indicates absolute value, * indicates complex conjugation and angle brackets ⟨ ⟩ are the averaging operation to the statistical estimation with a rectangular filter (also known as the window size). The filter is applied for the extra reduction of the difference in radar impulse response perceived by sensor path from the same piece of ground [94]. To enhance the quality of the amplitude image of the single-look Sentinel-1 that has 5 m resolution in range and 20 m in azimuth, and to obtain a spatial averaging coherence, different window sizes (e.g. 3 × 3 or 5 × 5 pixels) is applied based on the corresponding spatial resolution of the image [119]. The magnitude of the coherence ranges from 0 in the case of decorrelation (the interferometric phase is just noise), and 1 if the two signals are entirely correlated (complete absence of phase noise and a meaningless phase measurement). When the position and physical properties of the scatterers within the averaging window are the same for the two observations the coherence reaches to the maximum value [126]. In contrast, any differences in the position or properties of the scatterers in the interval between the two observations cause the phase difference of two signals backscattered by targets and thereby cause the coherence value to decrease. The phase difference of two signals backscattered by scatterers to the sensor is represented by an image called interferogram and the phase is given modulus 2π and revealed in the image by fringes [127].

5.2.1 Decorrelation Sources

A decrease of the coherence magnitude or decorrelation can have several sources such as physical changes in the terrain and changes in the position or charachteristics of the scattereres of the surface caused the non-conformity of the properties of the two acquisitions and expressed by the temporal terrain decorrelation ($\gamma_{temporal}$) [79]. The difference in the incidence angles between the two observations give rise to the geometric or spatial baseline decorrelation ($\gamma_{spatial}$). Thermal or system noise decorrelation ($\gamma_{thermal}$) or (γ_{SNR}) due to the charachteristics of the system e.g., antenna charachteristics and gain factor, the volume decorrelation (γ_{vol}) which results by volume scattering, (γ_{DC}) Doppler centroid decoreelation raised by the differences in the Doppler centroids between the two observations, the processing induced decorrelation ($\gamma_{processing}$) that is the error eventuates from the selected algorithms for example for co-registration and interpolation, and the bias decorrelation caused by the averaging window size (γ_{bias}). The total correlation or coherence (γ_{total}) which is calculated from Equation 5.12 is corresponding of the multiplication of the aforementioned correlation terms [63] and is defined as the equation 5.13.

$$\gamma_{total} = \gamma_{temporal} \gamma_{spatial} \gamma_{thermal} \gamma_{vol} \gamma_{DC} \gamma_{processing} \gamma_{bias}$$
 (5.13)

To obtain the Interferometric coherence this study only focused on the temporal decorrelation due to rapid changes in the scattereres over the agricultural fields during the crop growth season between the acquisitions and the other sources of the decorrelation (including geometric decorrelation, given the small differences in the incidence angles and the baselines between the Sentinel-1 interferometric acquisitions) was Ignored. However, due to that the absolute value of the coherence $|\gamma|$ which varies between 0 and 1, is alternatively demonstrated as a function of the Signal-to-Noise-Ratio (SNR) [63, 116, 128] and the sensitive interaction between C-band signal and vegetation therefore, the system noise decorrelation (γ_{SNR}) is also considered in this study and is defined in Equation 5.14.

$$\left|\gamma\right| = \frac{SNR}{SNR + 1} \tag{5.14}$$

Since the noise (n) and signal (C) are uncorrelated then:

$$\left|\gamma\right| = \frac{\left|C\right|^2}{\left|C\right|^2 + \left|n\right|^2} \tag{5.15}$$

Given that the thermal Signal-to-Noise-Ratio (SNR) is $\frac{\left|c\right|^2}{\left|n\right|^2}$, then the Equation 5.15 may be equivalently written as Equation 5.16 [63].

$$\gamma_{SNR} = \frac{1}{1 + SNR^{-1}} \quad Or = \frac{1}{\sqrt{(1 + SNR_{sat1}^{-1})(1 + SNR_{sat2}^{-1})}}$$
(5.16)

Where SNR_{sat} , the Signal-to-Noise-Ratio for each images is calculated in the interferometric pair and can be defined using Equation 5.17.

$$SNR_{sat} = \frac{\sigma_{sat}^0 - NESZ_{sat}}{NESZ_{sat}}$$
 (5.17)

Where σ_{sat}^0 is the backscattering coefficient for different acquisitions, and $NESZ_{sat}$ (Noise Equivalent Sigma Zero) that can be estimated suing look-up tables which is available in the Sentinel-1 metadata.

Figure 5.1 shows the general overview of satellite data processing in this thesis. A more detail workflow has been provided in each related subsection.

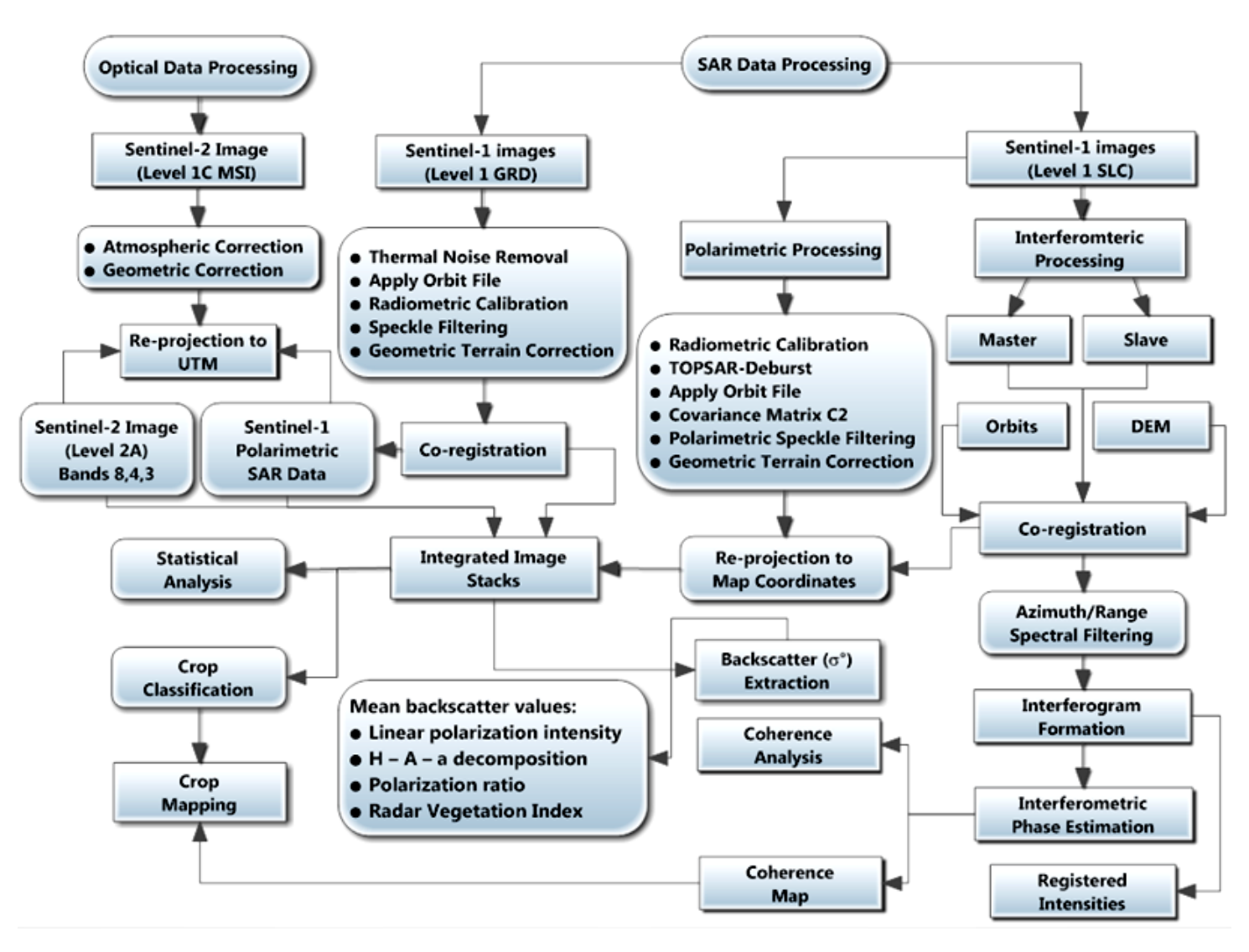


Figure 5.1 Flowchart of data processing

Optical, SAR, PolSAR and InSAR Applications in Crop Monitoring and Mapping

6.1 Sensitivity of Multi-Temporal SAR Parameters to Crop variables

The SAR technique has become increasingly an effective method of providing seasonal agricultural monitoring. SAR is a coherent radar system that generates high-resolution remote sensing imagery. A SAR sensor has capability to collect data in different weather conditions where the cloudy sky in most time of the growing season (particularly in rainy climate) is a serious obstacle to the application of optical images. Moreover, it can acquire data in day-or-night; exclusivity makes it suitable for long-term and multi-seasonal agricultural monitoring. The SAR system is sensitive to the vegetation biophysical variables and dynamical characteristics of plant targets, and underlying soil parameters such as plant water content, geometric property, deflection and irregularity, soil surface roughness and moisture content. The Polarimetric Synthetic Aperture Radar (PolSAR) technique has provided various opportunities and challenges in agricultural activities mainly on crop management. This study investigates the potential of Sentinel-1 dual polarimetric SAR in estimation and monitoring of crop parameters, namely crop height and canopy coverage (CC) in an agricultural area. The objective of this study is to evaluate the sensitivity of different Sentinel-1 dual polarimetric SAR parameters to crop height and CC of maize, sunflower and wheat, and to investigate the changes in SAR backscatter arising from crop height and CC during crop phenological stages.

6.1.1 Materials and methods

Within this framework, we have investigated the sensitivity of 10 parameters including linear polarization backscattering coefficients, H-A- α decompositions, polarization intensity ratios (VH/VV , VV/VH and VV-VH/VV+VH), Radar Vegetation Index (RVI) and intensity arithmetic calculations (VH-VV and VV+VH) derived from

multi-temporal C-band Sentinel-1 SAR data, to crop height and canopy coverage (CC) of maize, sunflower, and wheat. For this purpose, field measurements were carried out simultaneously with SAR data acquisitions. For backscattering analysis four Sentinel-1 SAR images in descending orbit direction were acquired throughout the same growth season of the study area.

6.1.2 Study Area

The Konya basin (38° 40' N, 32° 26' E) in central Turkey is selected for field measurements and satellite images collection (Figure 6.1). The terrain of the study area is partly flat with a gently sloping (2%-6%) and, the smallest field area of approximately 0.5 and the largest 18 hectare in size. According to the Ministry of Agriculture and Forestry of Turkey, the distribution of major soils in the study region is Reddish Brown and Brownish soils Figure 6.2. The soil texture in the study area

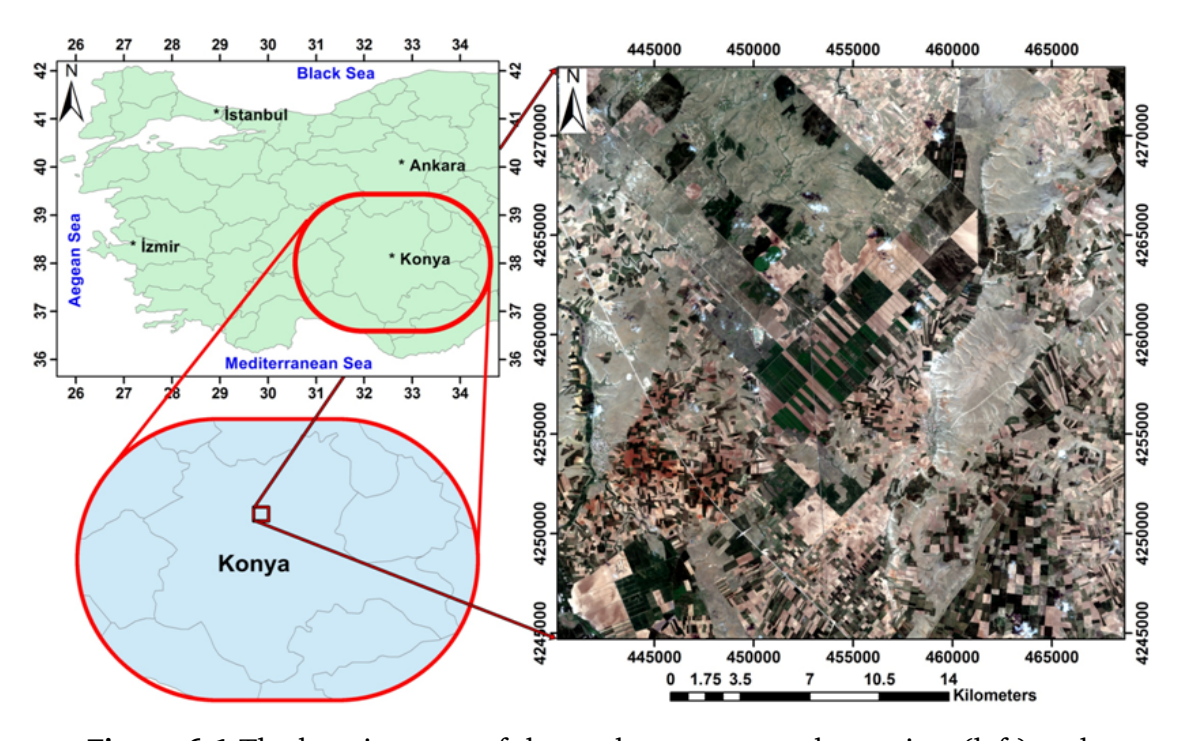


Figure 6.1 The location map of the study area; general overview (left) and Sentinel-2 RGB image of the study site (right)

consists of clayed loam and loamy (medium structure), slightly alkaline, salt-free, and low contents of organic matter (1.30-2.08%). The region has an arid to semi-arid predominant weather conditions. The land use type is mainly agricultural land in the study site (Figure 6.3). Therefore, the demand for water consumption for irrigation is increasing due to the extent and dense of agricultural activities. Maize, sunflower, and wheat are three investigated crops patterns as they have different structures. Maize and sunflower based on field campaign, generally are planted at the beginning of May,

and harvested at the end of August or the beginning of September in this study area. Winter wheat is seeded in previous November and harvested at the end of July.

6.1.3 Field Surveys

In situ measurements were conducted for maize, sunflower and wheat fields in the spring–summer agricultural season of the year 2016. Crop variables and parameters which indicate the growth rate including crop height and CC were collected simultaneously with the SAR data acquisition, and recorded during the field works. Field data collection includes measuring the row and plant cover by still tape in unit area, taking photographs by the camera and recording field characteristics such as soil properties and irrigation status. For calculating CC, photographs were taken in downward position and perpendicular to the ground with 100 cm distance from camera and canopy outmost in the tillering stage when the crop height was less than 100 cm. Considering the study area, 36 test fields that consist of 19 maize, 6 sunflower fields, and 11 wheat fields were dedicated for this research.

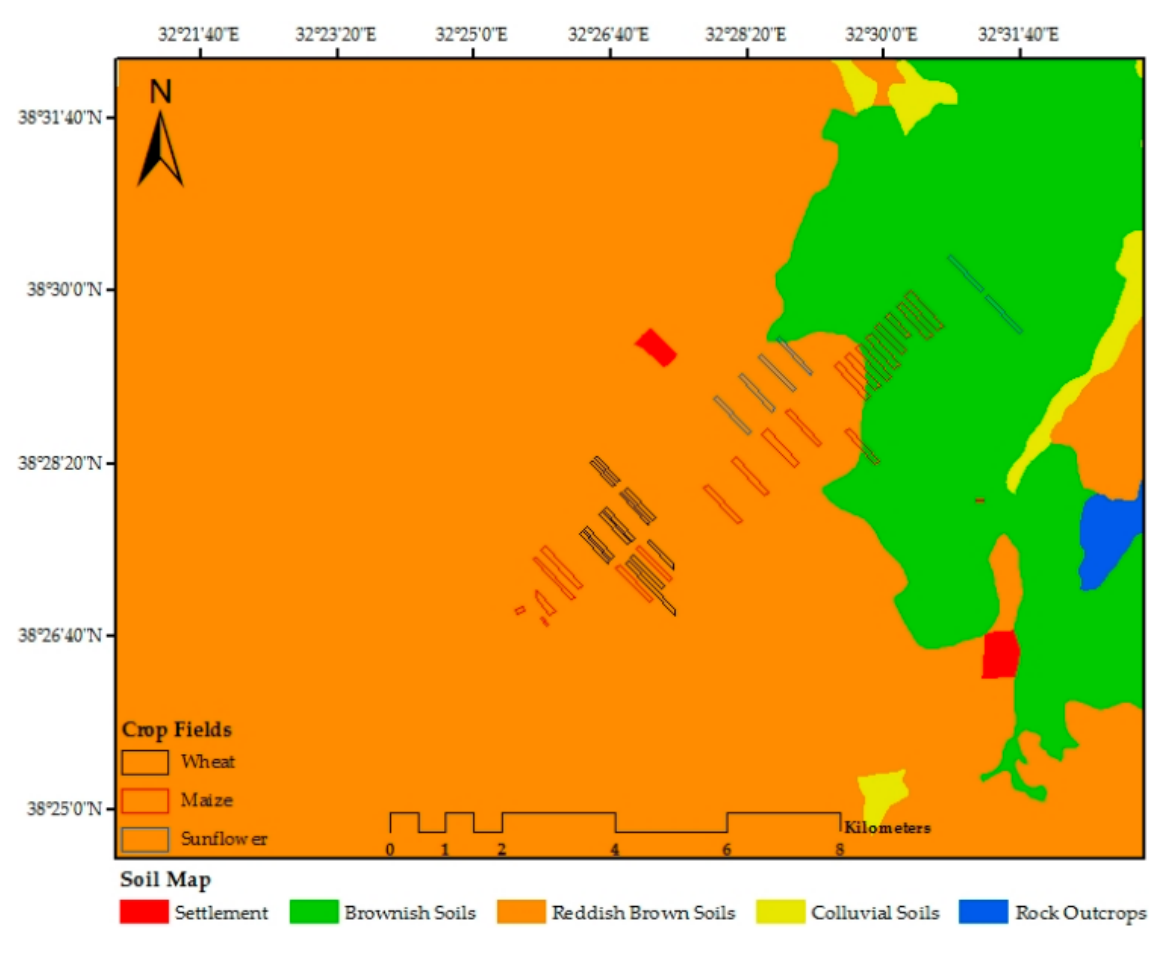


Figure 6.2 Soil map of the study area

The variability of development stages for maize, sunflower and wheat has been defined

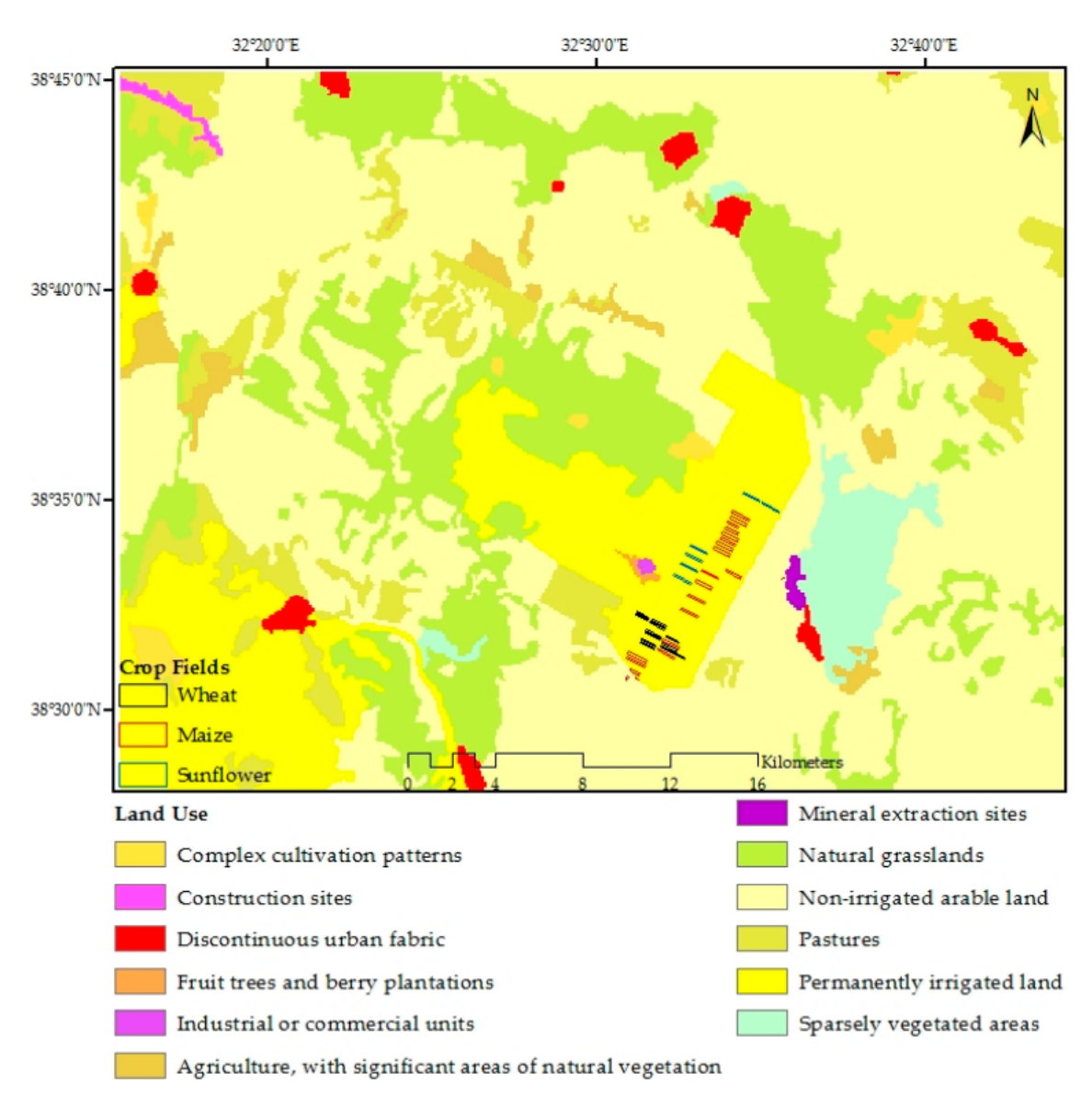


Figure 6.3 Land use map of the study area (Source: Copernicus Land Monitoring Service [129])

by applying the "Biologische Bundesanstalt, Bundessortenamt, and CHemische" (BBCH) [20] indicator for each field that generally consist of vegetative and reproductive stages. Seasonal maize, sunflower, and wheat crop calendar of the study area is presented in Figure 6.4.

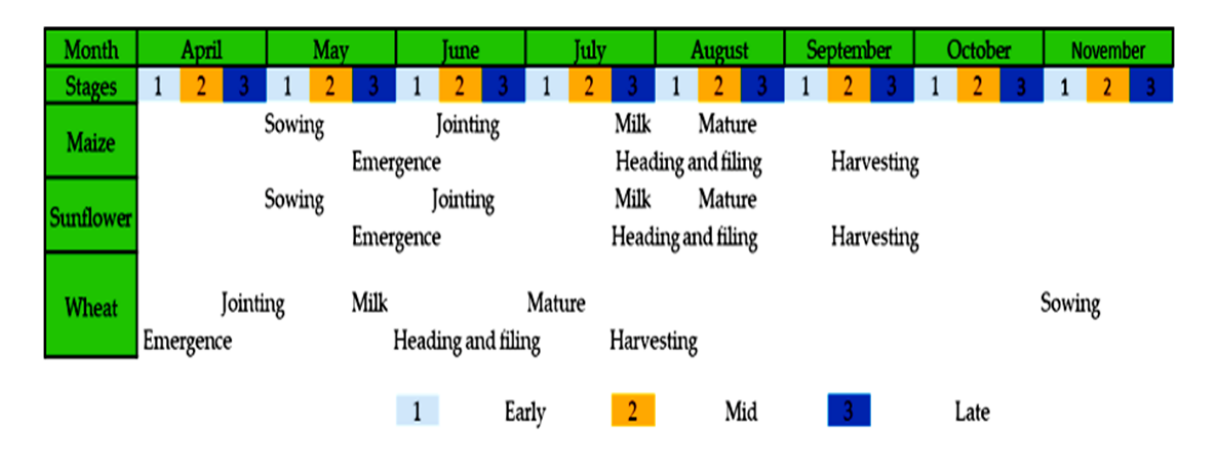


Figure 6.4 Seasonal maize, sunflower and wheat calendar of the region

According to the defined height and CC thresholds, derived from SAR backscattering and BBCH-scale, we call two stages for crops growth season; season; the early stage and the later stage.

Four field surveys were conducted to obtain accurate ground measurements in late May—mid June, early July, late July, and late August 2016. General growth stages categories (leaf development, stem elongation, heading and flowering), are defined according to the BBCH-scale (Table 1). For calculating the crop height of each test site, five height measurements were obtained and their mean value was calculated to represent the crop height of the relevant test field. From the test sites, plant cover and row were measured and also photographs were captured to determine and evaluate the CC percentage. A synopsis of the maize, sunflower and wheat of different growing stages is given in Figure 6.5.

Table 6.1 Biologische Bundesanstalt, Bundessortenamt, und CHemische (BBCH)-identification keys for field measurements and Synthetic Aperture Radar (SAR) data acquisitions of the study area

Field Surveys	Crop Growth Stages (BBCH)	SAR Acquisitions Dates	
19 May–12 June 2016	leaf development	13 June 2016	
01–02 July 2016	stem elongation	07 July 2016	
31 July 2016	heading ¹	31 July 2016	
24–25 August 2016	flowering	24 August 2016	

¹Due to variation in wheat growth conditions in different fields, in general heading stage starts at late May and lasts until mid-June.



Figure 6.5 Different growth stages of crops in the study area

In this study site, the BBCH-scale is considered as 53 when the maize height was in range of 120–150 cm. This growth stage of the maize is at the inflorescence emergence and heading stage. When maize height was greater than 220 cm, the BBCH-scale was 69 and represented the end of flowering. Once the sunflower height was greater than 92 cm, the BBCH-scale is found as 79, indicating the end of flowering and the inflorescence reaches full size. The BBCH-scale is considered as 59 after that wheat height reached to 53 cm and inflorescence fully emerged. We observed that different wheat height could have the similar wheat BBCH due to variation of wheat growth conditions which cause to distinction even though they are at the same phenology, in agreement with the study of Liao et al. [57]. Figure 6.6 (a-c) shows the relationship between crop height and the BBCH-scale corresponding to the each crop principal growth stages.

Scatterplots (d–f) in Figure 6.6 show the relationship between crop height and CC. Note that the correlation between CC of three different crops has been changed in different height in each crop. For maize, the variation of correlation was determined when the maize CC threshold is 75%. This threshold is 85% and 60% for sunflower and wheat respectively.

6.1.4 Sentinel-1 Dual Polarimetric SAR Data Statement and Processing

We used Single Look Complex (SLC) Sentinel-1A interferometric wide swath (IW) data in descending pass direction (Table 2). Sentinel-1 satellites are equipped with C-band sensor with an incidence angle range between 29.1° and 46.0° at 5405 MHz radar

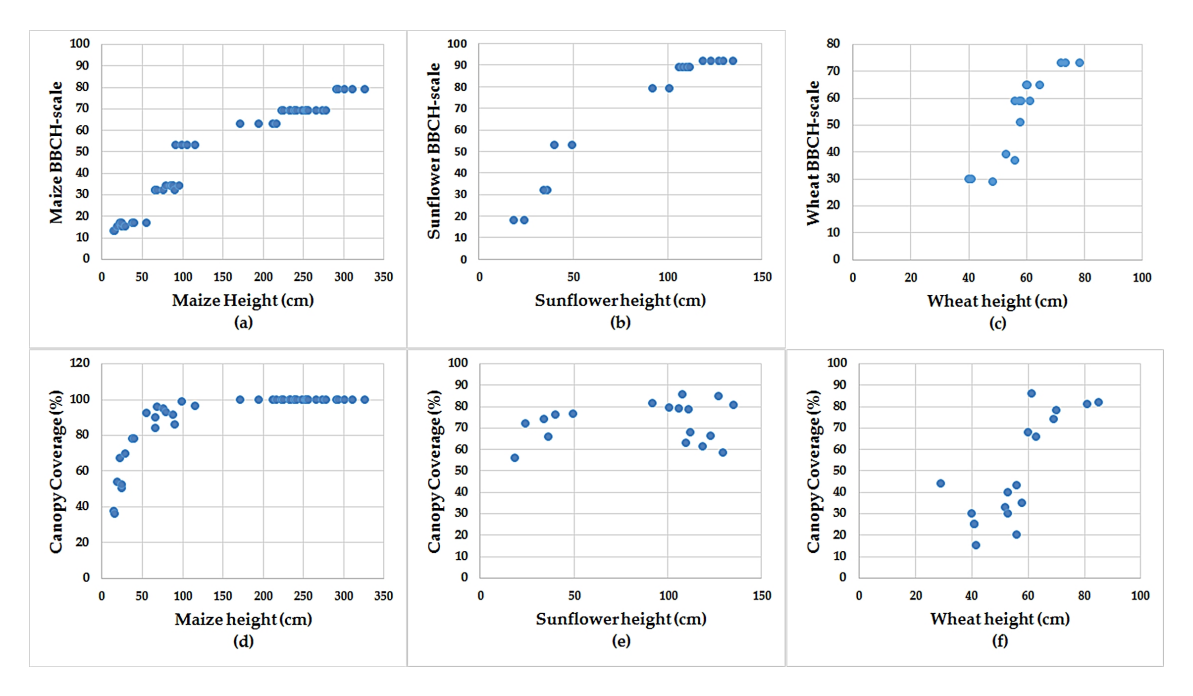


Figure 6.6 BBCH-scale relationship with crop height **(a–c)**, and Correlation between canopy coverage (CC) and crop height **(d–f)** for maize, sunflower, and wheat

frequencies. The satellite obtains data with dual polarization (VV and VH) backscatter where electromagnetic waves have polarized vertically (V) for transmission and H/V for reception [130]. Data can be acquired in both ascending and descending orbit pass directions, which means that any object on the earth surface can be evaluated as two independent sights. The difference is that due to steeper incident angle of the ascending orbit therefore the mean backscatter values are rather higher in compare with descending orbit [131]. For time series analysis of SAR backscatter, four C-band polarimetric SAR data during the growth stages of the selected crops from mid-June to late August were acquired for investigation of the sensitivity of Sentinel-1 data to the crops. Figure 6.7 shows the flowchart of Sentinel-1 dual polarimetric SAR data processing.

Table 6.2 Specifications of acquired Sentinel-1 datasets over Konya basin, Turkey

Acquisition	Incidence	Satellite	Polarization	Nominal	Orbit
Date	Angle ($^{\circ}$) 1	Pass	Polatization	$Res.(m)^2$	No
13 June 2016	30.72-49.09	Descending	VH and VV	2.33-13.93	65
07 July 2016	30.72-49.11	Descending	VH and VV	2.33-13.93	65
31 July 2016	30.72-49.11	Descending	VH and VV	2.33-13.93	65
24 August 2016	30.72-49.11	Descending	VH and VV	2.33-13.93	65

¹Incidence angle from near to far range ²Range and azimuth resolutions

Different Sentinel-1 dual polarimetric SAR parameters including linear polarization backscattering coefficients, H-A- α decompositions, polarization intensity ratios (VH/VV, VV/VH and VV-VH/VV+VH), Radar Vegetation Index (RVI), intensity

arithmetic calculations and crop variables (crop height and CC) are investigated. Mean backscattering coefficient values for each sample site for different crops are defined and the correlation between the in situ measurements are analyzed. The results show that responses of polarimetric SAR parameters to the crop variables (crop height and CC) vary for different crop types at different phenological stages of the crops. For maize, SAR backscatter coefficient is more sensitive to crop height at the early stage of crop growth compared to the later stage, while the same situation is not true for sunflower and wheat.

6.1.5 SAR Parameters and Their Correlation with Crop Height

Almost in all visited fields, the mean backscatter values indicated similar tendency in four stages of crop growth. In Figure 6.8, mean backscatter coefficient (σ_{VV} and σ_{VH} and VV+VH) values of each sample site are determined and the correlation between the field measurements are presented. It is observed that the maize had high sensitivity at the beginning but starts to decrease when the maize height is higher than 150 cm at inflorescence emergence and heading stages. Sunflower is not sensitive to the crop height only when the sunflower height is greater than 90 cm. At the end of flowering and the inflorescence, it shows low sensitivity compared to its early and later stages. In comparison with maize and sunflower, wheat had relatively good sensitivity at the end of heading. Regarding wheat full inflorescence which is varying in different heights, the correlation between SAR backscattering (VV+VH and σ_{VV}^0) and wheat height is considerably less as in inferred from Figure 6.10 g,h in growing stage.

Table 6.3 gives the coefficient of determination (R^2) between Sentinel-1 dual polarimetric SAR parameters and measured crop height for maize, sunflower and wheat. Both σ_{VV}^0 and σ_{VH}^0 showed high correlation ($R^2=0.81$ and 0.80 respectively) and VV+VH had highest correlation ($R^2=0.82$) with maize height at the early stage. Whereas the correlation between SAR parameters to sunflower height is very low ($R^2=0.31$) at the same stage. Almost all SAR parameters show relatively good correlation at the early stage of wheat. For instance, a good negative correlation with VH/VV intensity ratio and σ_{VH}^0 are obtained at the early stage of wheat ($R^2=0.66$, and 0.65 respectively). However, all of the crops have very weak correlation or even they are not correlated and sensitive to plant height in the later stage.

Amongst the H-Alpha decomposition parameters, Alpha (α) decomposition parameter represents the highest correlation ($R^2=0.67$) with wheat height during the early growth stage. The maize height is relatively correlated with H-Alpha decomposition

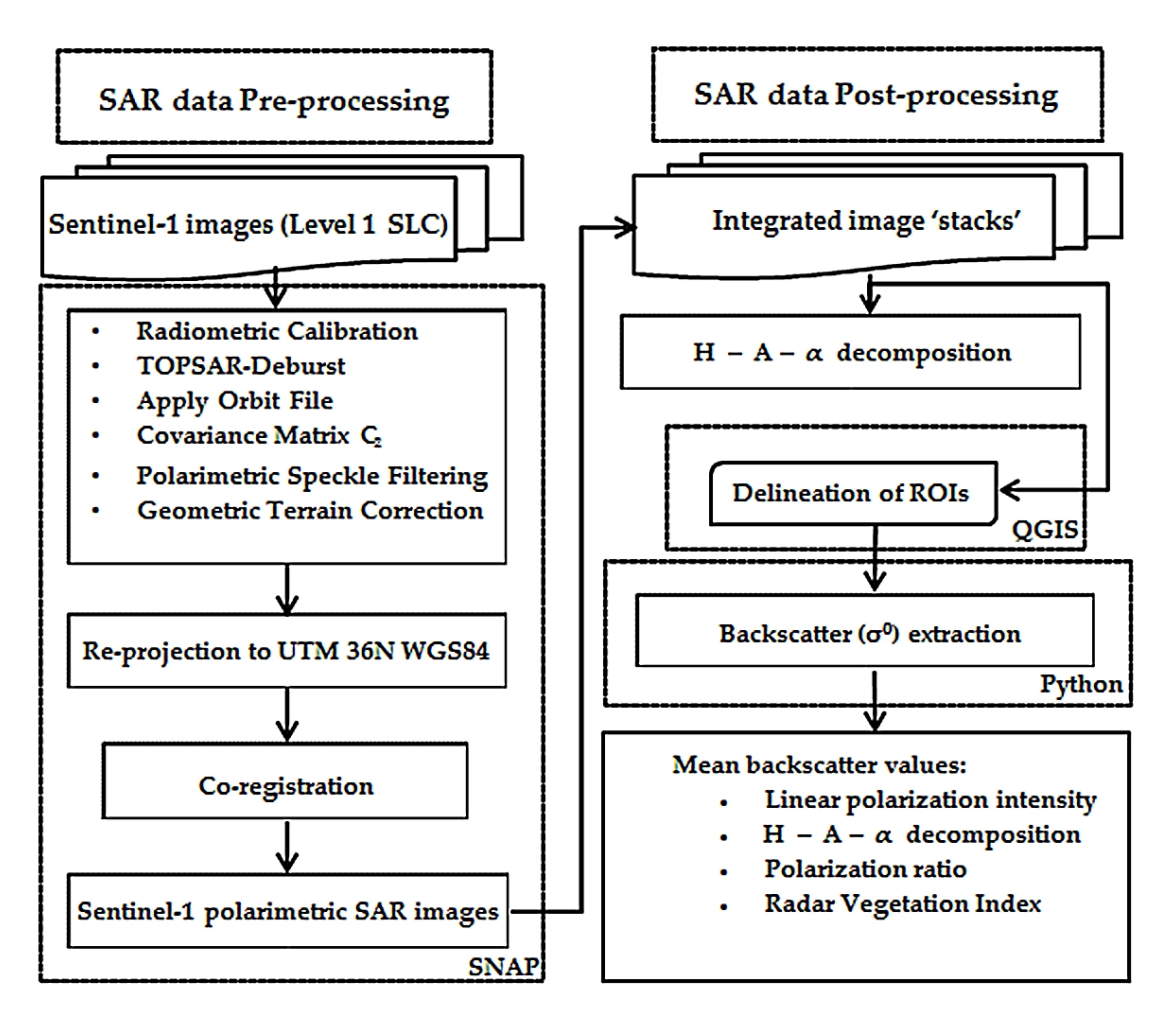


Figure 6.7 Flowchart of Sentinel-1 dual polarization SAR data processing

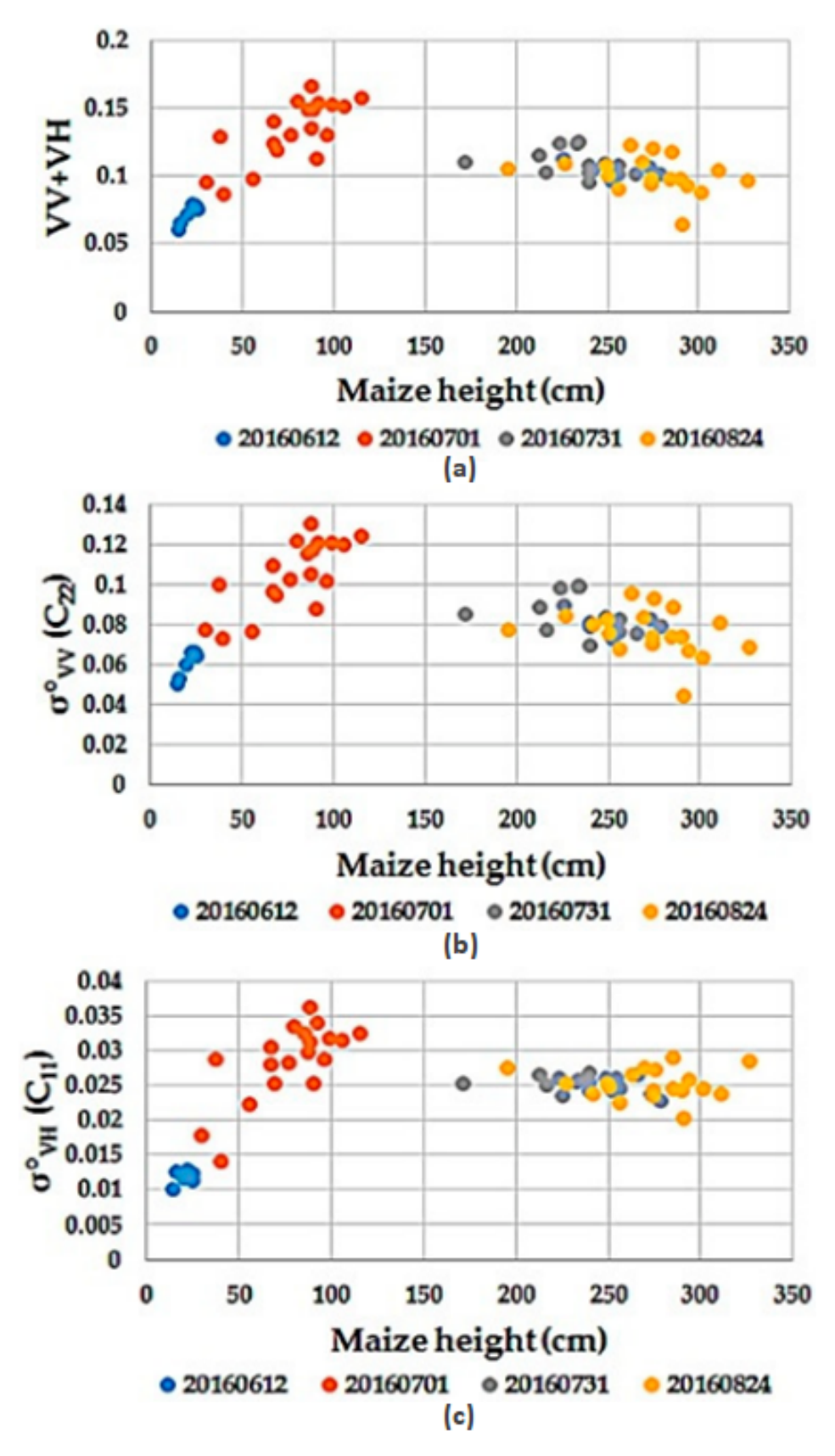


Figure 6.8 Correlation between **(a)** intensity arithmetic calculation of VV+VH, **(b)** σ_{VV}^0 backscatter, and **(c)** σ_{VH}^0 backscatter values of maize with its height during growing stages

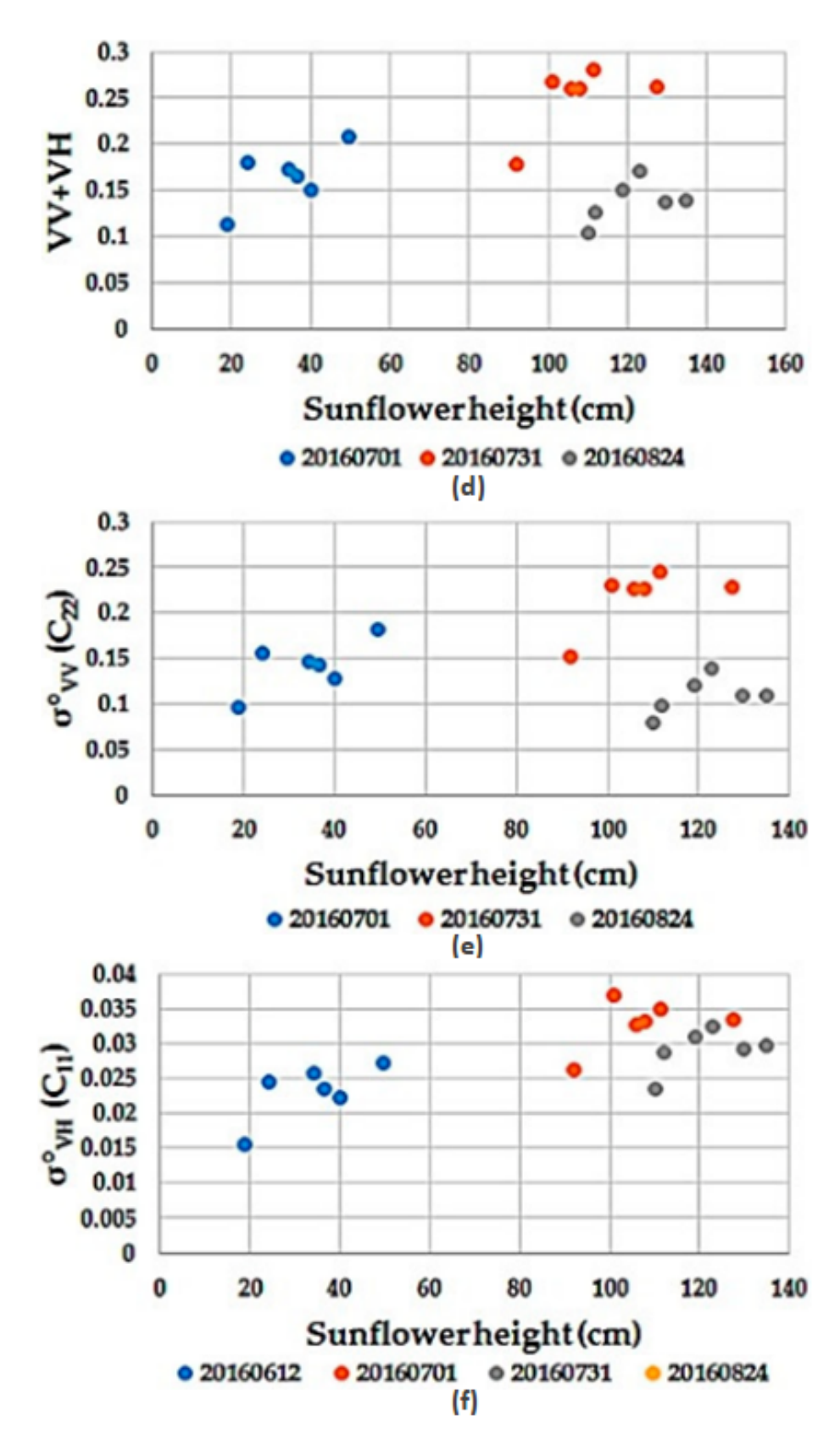


Figure 6.9 Correlation between **(d)** intensity arithmetic calculation of VV+VH, **(e)** σ_{VV}^0 backscatter, and **(f)** σ_{VH}^0 backscatter values of sunflowe with its height during growing stages

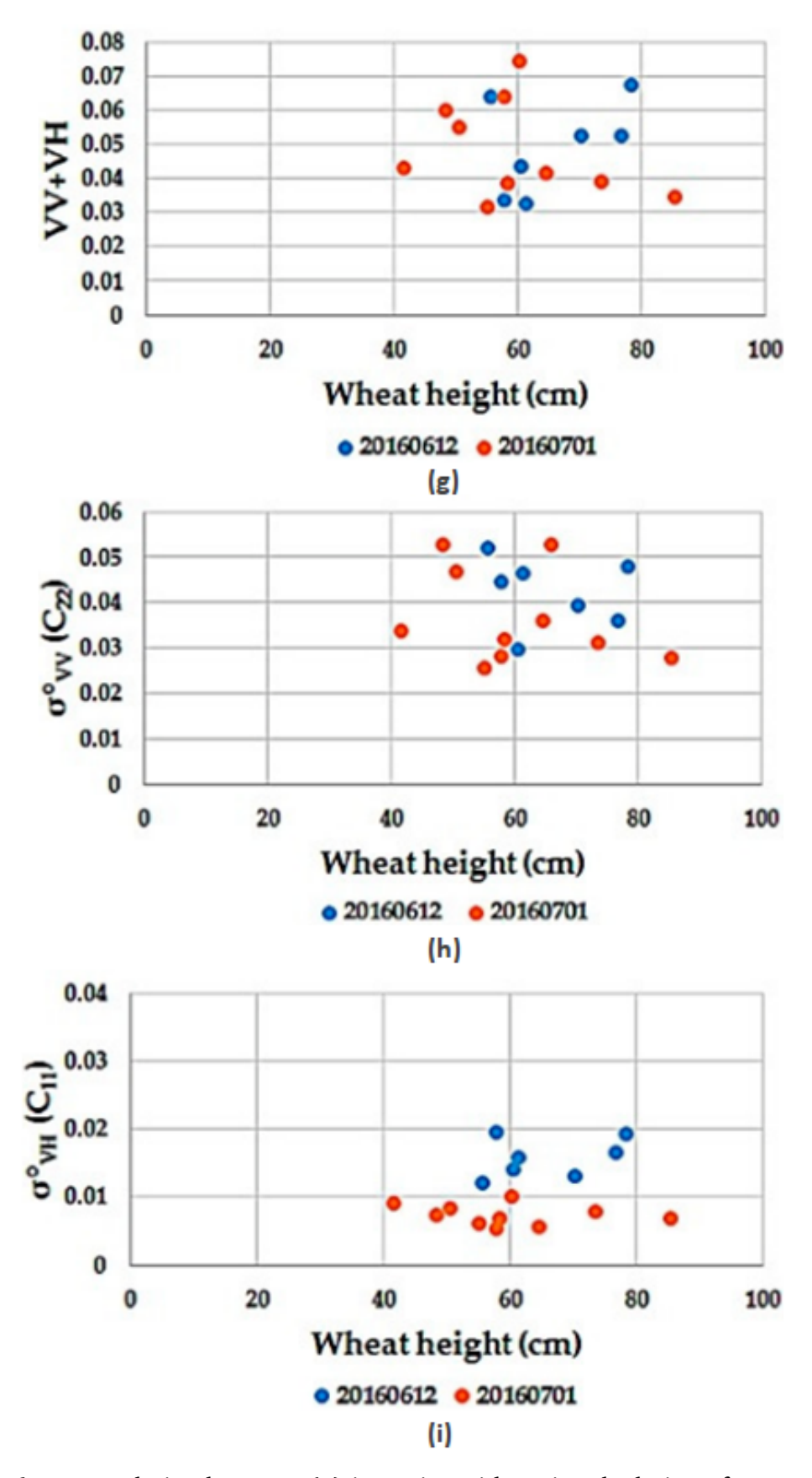


Figure 6.10 Correlation between **(g)** intensity arithmetic calculation of VV+VH, **(h)** σ_{VV}^0 backscatter, and **(i)** σ_{VH}^0 backscatter values of wheat with its height during growing stages

Table 6.3 Coefficient of determination (R^2) between crop height and Sentinel-1 SAR parameters

SAR Parameters	Maize (H) ¹		Sunflower (H)		Wheat (H)	
	H<150	H>150	H<92	H≥92	H <53	H≥53
Linear Polarization						
C11_Intensity (VH)	0.80	-0.1	0.31	-0.06	-0.65	0.03
C22_Intensity (VV)	0.81	-0.2	0.17	-0.19	0.62	-0.01
H-Alpha Decomposition						
Entropy (H)	0.53	0.20	0.01	0.20	-0.61	0.06
Anisotropy (A)	-0.54	-0.23	0.00	-0.18	-0.65	-0.05
Alpha (α)	-0.52	-0.19	-0.05	-0.17	0.67	-0.07
Radar Vegetation Index						
RVI	0.53	0.21	0.11	0.18	-0.65	0.03
Intensity Ratio						
VH/VV	0.52	0.21	0.11	0.17	-0.66	0.05
(VV-VH)/(VV+VH)	-0.53	-0.21	-0.11	-0.18	0.65	-0.05
Intensity Arith. Oper. ²						
VH-VV	0.77	-0.21	-0.14	0.20	0.63	-0.03
VV+VH	0.82	-0.18	0.19	-0.18	0.61	0.00

¹The height measurement unit is centimeter. ²Intensity Arithmetic Operation. The minus indicates negative correlation.

parameters at the early stage, although no considerable correlation is observed during the early stage of sunflower and at the later stage of wheat. Figure 6.11 shows the correlation between the H-Alpha decomposition parameters and crops height of maize, sunflower and wheat.

6.1.6 SAR Parameters and Their Correlation with Crop Coverage

The CC measured in field includes measuring the row and plant cover by steel tape in unit area. For validation of the CC calculated from measured data, photographs were taken using the camera in downward position and perpendicular to the ground with 100 cm distance from the camera lens. The CC extraction process is done by application of Python glob image processing package [132]. The photos are first converted to HSV (Hue, Saturation, and Value) model and used as a detector for the type and shape and to do color constancy processing by grouping or classifying the image. Following the HSV conversion green mask is applied to slice the green areas as white ratio and black to the bare soil. The sample classified green area for wheat is given in Figure 6.14. The unit area from the photograph is calculated using the ground sampling distance (GSD) formula and setting calibration derived from images. The contributing parameters for determination of ground resolution are the camera's height above the ground, the camera's pixel size, and the lens' focal length.

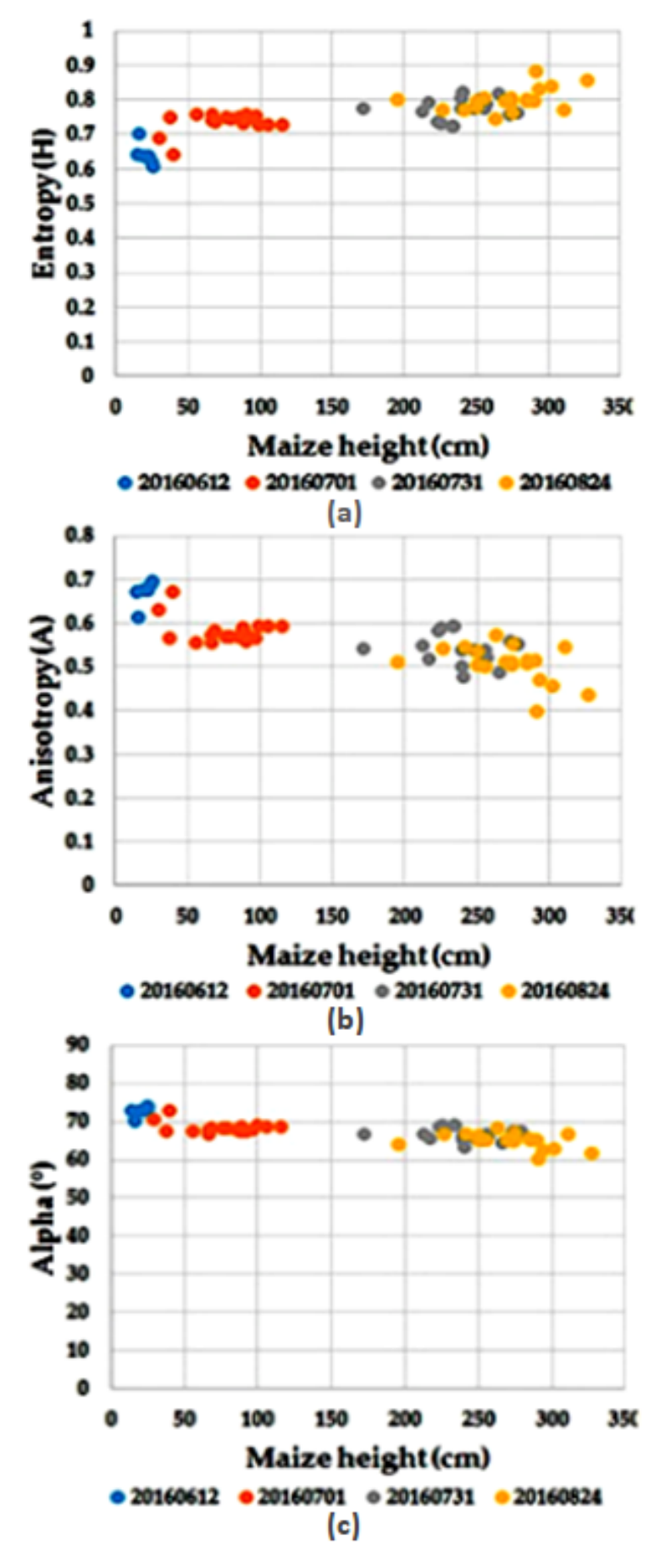


Figure 6.11 Correlation between Entropy **(a)**, Anisotropy, **(b)** and Alpha **(c)** decompositions of maize with its height during growing stages

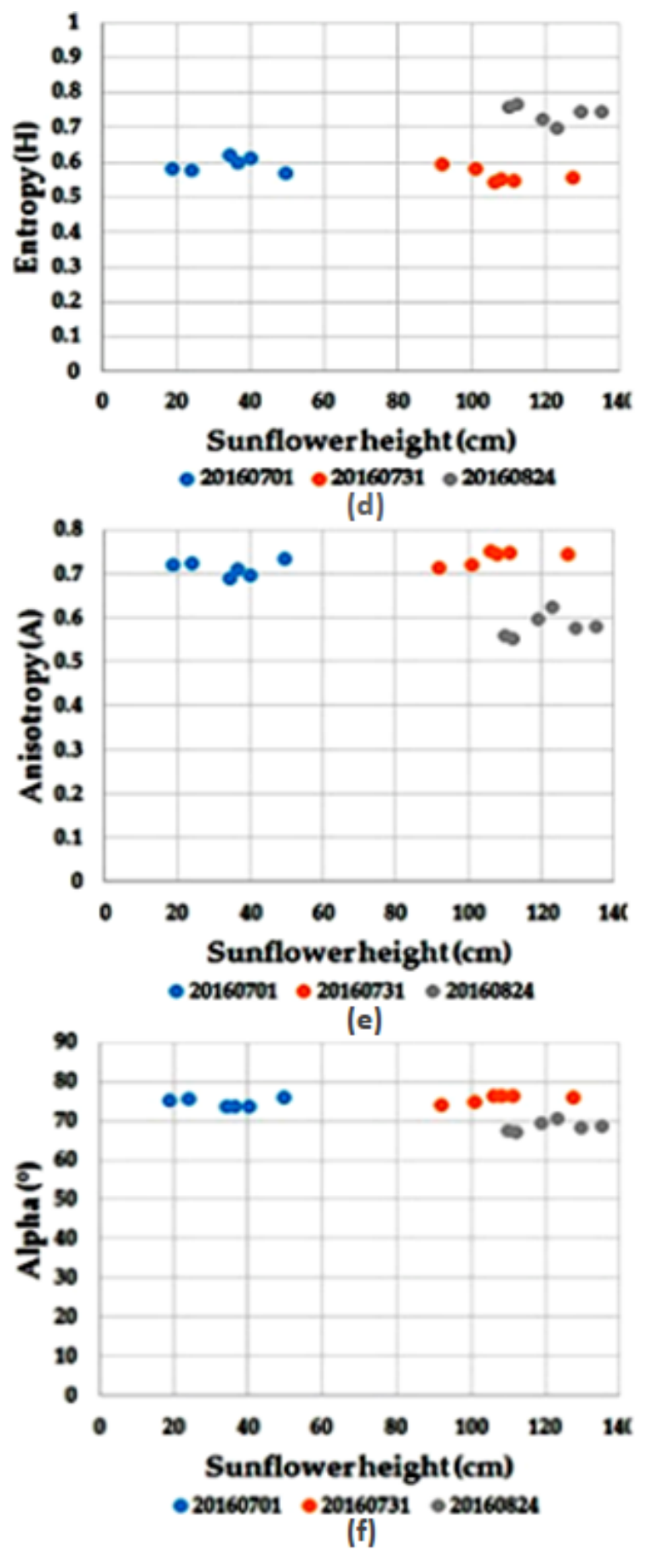


Figure 6.12 Correlation between Entropy **(d)**, Anisotropy, **(e)** and Alpha **(f)** decompositions of sunflower with its height during growing stages

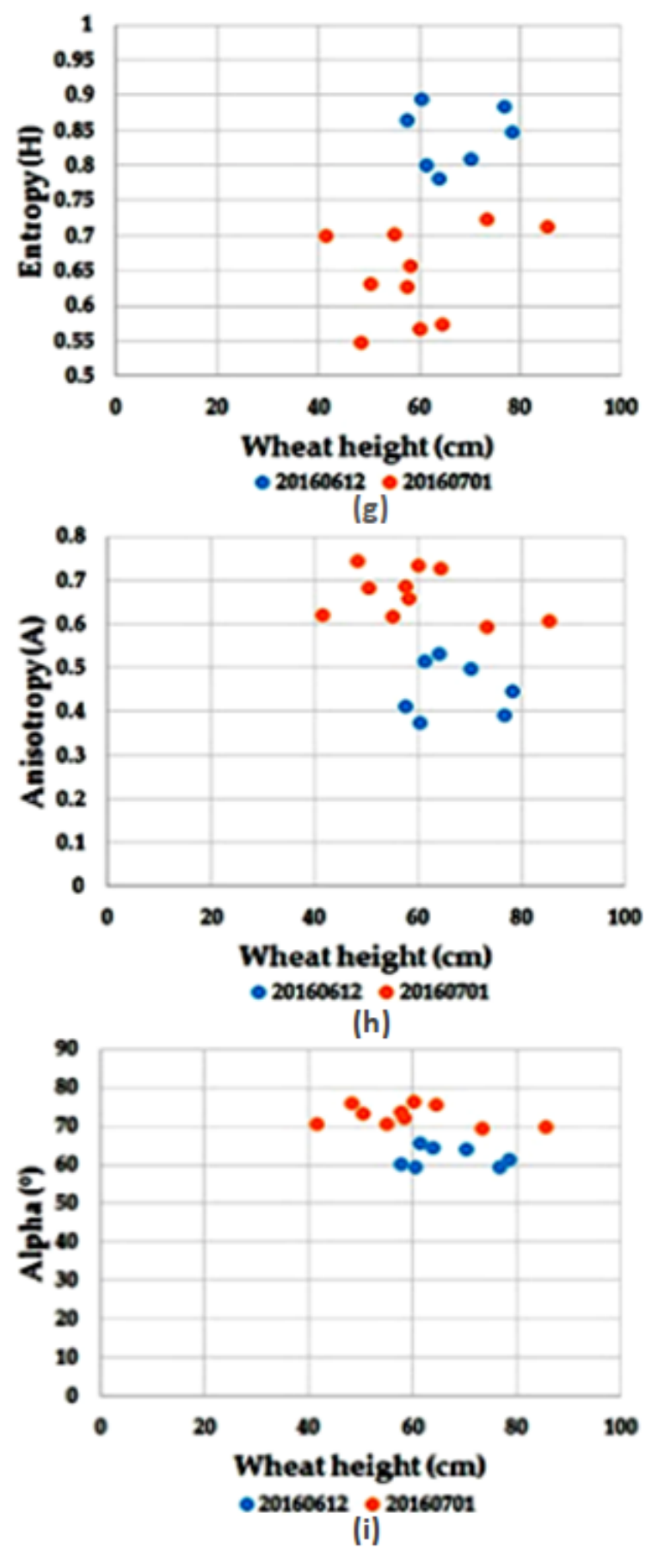
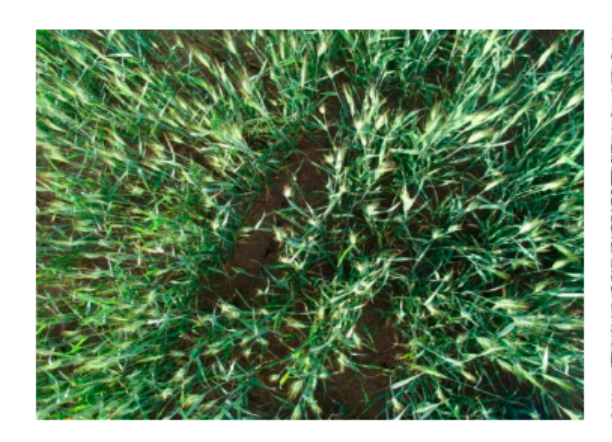


Figure 6.13 Correlation between Entropy **(g)**, Anisotropy, **(h)** and Alpha **(i)** decompositions of wheat with its height during growing stages



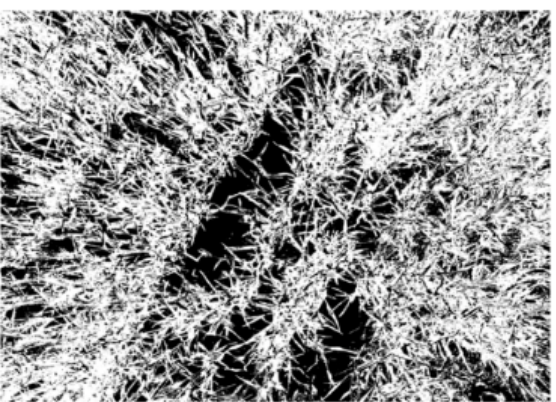


Figure 6.14 Canopy coverage extraction from in-situ photo taken using python image processing packages. **Left** panel is the original photo and the **right** panel shows white ratio calculated as green areas and black to the bare soil in wheat sample field

The coefficient of determination (R^2) between Sentinel-1 polarimetric SAR parameters and the measured CC for maize, sunflower and wheat for early and later growing stages are given in Table 6.4. According to the principle growth stage [133] when the maize reaches to the end of its stem elongation, leaves completely unfold and have full size. When the BBCH-scale is greater than 39 for maize, CC is measured 75%. The CC for sunflower and wheat is measured as 85% and 60%, respectively when the BBCH-scale is greater than 51 and 49.

Considering Sentinel-1 dual polarimetric SAR parameters and measured CC, the highest correlation is obtained for the VV polarization ($R^2 = 0.73$) and VV+VH (R^2 = 0.73) when the CC is lower than 75% for maize while with increasing CC the correlation decreased ($R^2 = 0.49$) for both crops. This is contrary to the findings of Liao et al. [57] where the sensitivity of RADARSAT-2 polarimetric SAR and its correlation with fractional vegetation cover (FVC) in HV polarization is high for maize, and they suggest that VV polarization is not a useful parameter for monitoring broad-leaf crops. Their findings may have conflict with our results due to the sensors properties. Regarding the sunflower, in its early stage (i.e., CC < 85%), again the higher coefficient of determinations are obtained for VV polarization ($R^2 = 0.46$) and VV + VH ($R^2 = 0.47$). However, comparing the maize and the sunflower as two different broad-leaf crops in our study, R^2 of the sunflower is lower than the maize. The discrepancy in correlations might be due to the difference in leaves geometry of maize and sunflower. In other respects, similar to the findings of Liao et al. [57], no correlation is observed for wheat at both stages in our study. This may be due to the wheat structure and leaves geometry as narrow-leaf crop. Wheat can reach its full development at early stage and penetrating from biomass occurs due to narrow leaves, stem affectation and contributing of underlying soil resulting attenuation of SAR backscatter [134]. Figure 6.15 depicts the parameters which have highest correlation with CC during the growth stage for maize and sunflower.

The results show that responses of polarimetric SAR parameters to the crop variables (crop height and CC) have variation in different crop types at different phenological stages of the crops. Among the SAR parameters, VV+VH and VV indicated a strong correlation with maize height by means of the coefficient determination (R^2) of 0.82 and 0.81, respectively. The maize CC with VV parameter showed high correlation (R^2 =0.73) at the early growing stage, but the correlation became weaker at the later stage while the sunflower height correlation with the majority of SAR parameters was insignificant. The wheat height represented high correlation with the Alpha (α) decomposition parameter. The sensitivity of SAR parameters to the wheat and sunflower's CC are good at the early stage while no significant correlation is observed at the later stage.

Table 6.4 Coefficient of determination (R^2) between CC and Sentinel-1 SAR parameters

SAR Parameters	Maize (CC) ¹		Sunflower (CC)		Wheat (CC)	
	CC<75	CC≥75	CC<85	CC≥85	CC <60	CC≥60
Linear Polarization						
C11_Intensity (VH)	0.25	-0.41	0.07	0.18	-0.01	-0.15
C22_Intensity (VV)	0.73	-0.49	-0.46	0.09	0.10	-0.06
H-Alpha Decomposition						
Entropy (H)	-0.28	0.36	-0.06	-0.01	-0.09	-0.01
Anisotropy (A)	0.30	-0.31	0.06	0.01	0.05	0.02
Alpha (α)	0.29	-0.32	0.07	0.00	0.07	0.04
Radar Vegetation Index						
RVI	-0.29	0.29	-0.07	0.01	-0.08	-0.03
Intensity Ratio						
VH/VV	-0.30	0.28	-0.07	0.00	-0.06	-0.05
(VV-VH)/(VV+VH)	0.29	-0.29	0.07	0.00	0.07	0.04
Intensity Arith. Oper. ²						
VH-VV	-0.69	0.48	-0.41	-0.07	-0.15	0.02
VV+VH	0.73	-0.49	0.47	0.10	0.05	-0.11

¹The CC is based on percent (%). ²Intensity Arithmetic Operation. The minus indicates negative correlation.

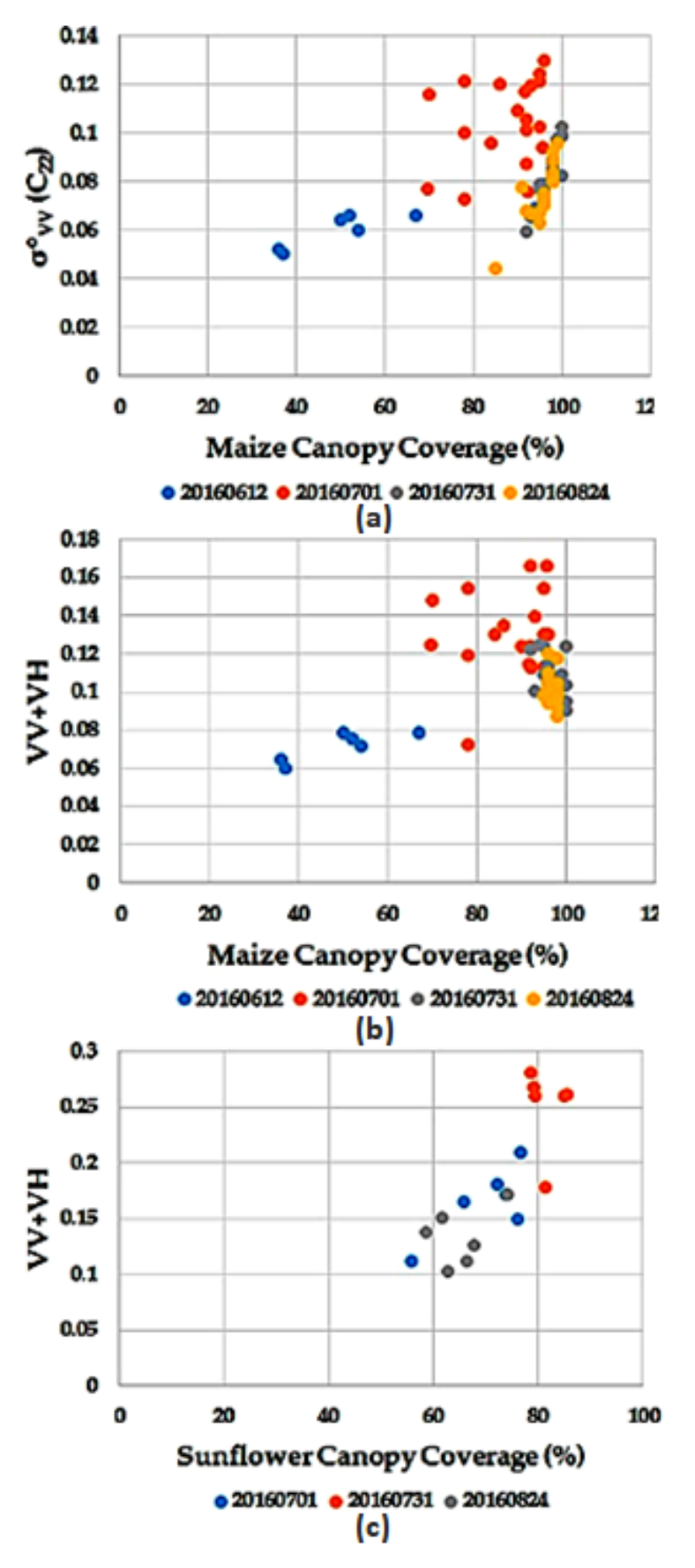


Figure 6.15 Correlation between σ_{VV}^0 (a), and VV+VH (b), backscatter values of maize, and VV+VH (c) backscatter value of sunflower with their CC during growing stages

6.2 Integration of radar and optical datasets for crop mapping improvment

Combining data from different sources of remote sensing data such as optical and radar datasets offer unique spectral and textural information for land use/cover evaluations, characterizing land use changes and generating information with higher quality than the individual datasets [6]. Optical data is limited by cloud cover, sensor spatial and temporal resolutions while Synthetic Aperture Radar (SAR) sensor has capability to collect data in different weather and day-or-night. Space-borne SAR data due to their high spatial and temporal resolution help to perform field-level crop classification and monitoring activities [36, 37]. In addition, SAR sensor has a capability to differentiate crop types due to its sensitivity to the crop structure and water content. Crop structure and water content are variables that varying in respect with crop type, growing stage and crop conditions [38].

For various land cover features, SAR products provide the feasibility of estimating crop height, crop type and crop condition mapping which are valuable information for different agricultural applications and marketing of agricultural yields [39]. Object characteristics such as orientation, material constituents, configuration, and dielectric properties can be estimated using SAR Polarimetry [109]. Scattering SAR data can be obtained in different wavelengths and polarizations. Texture measures, multi-sensor fusion, multi-polarization data, multi- temporal data and polarimateric data are techniques which is used to classification of the vegetation type [46, 47]. Different crop types at each phenological stage show different bio-physical characteristics [36]. Plant water content, roughness, leaf size, and vegetation greenness level that are related to the bio-physical characteristics of the features represent the amount of reflectance. Hence, optical sensors are beneficial for crop mapping and reliable applicants for agricultural land use monitoring as they measure reflectance from targets in the electromagnetic spectrum (reflectance in visible and shortwave infrared and thermal spectrum). However, success in crop identification with optical data mainly depends on the acquisition of image during key crop phonological stages. The accuracy of the classification decreases during these critical periods if optical data are used [3]. When added to the broad land use/cover classes' information provided by the optical data, the surface roughness and moisture information which are provided by SAR sensor allow one to extract more detailed specification of land surface and features [6].

In this section, the potential of discriminating crop types using polarimetric SAR (Sentinel-1) in integration with useful optical (Sentinel-2) indices is demonstrated. In order to map agricultural land management regimes of different intensities, it

is required to develop an approach to assess the patterns and rates of agricultural land use. Hereby, to discriminate different land use/cover categories of the study area, the potential of remotely sensed image analysis to merge multispectral and SAR images within a hierarchical classification framework were evaluated. The conceptual methodology of crop classification is shown in Figure 6.16. Main objectives of the study would be:

- Analyzing how to improve land use/cover mapping to better separation of land management regimes,
- Combination of the multi-spectral optical image and multi-temporal polarimetric SAR data to assess how to enhance crop classification methodology in the study area.

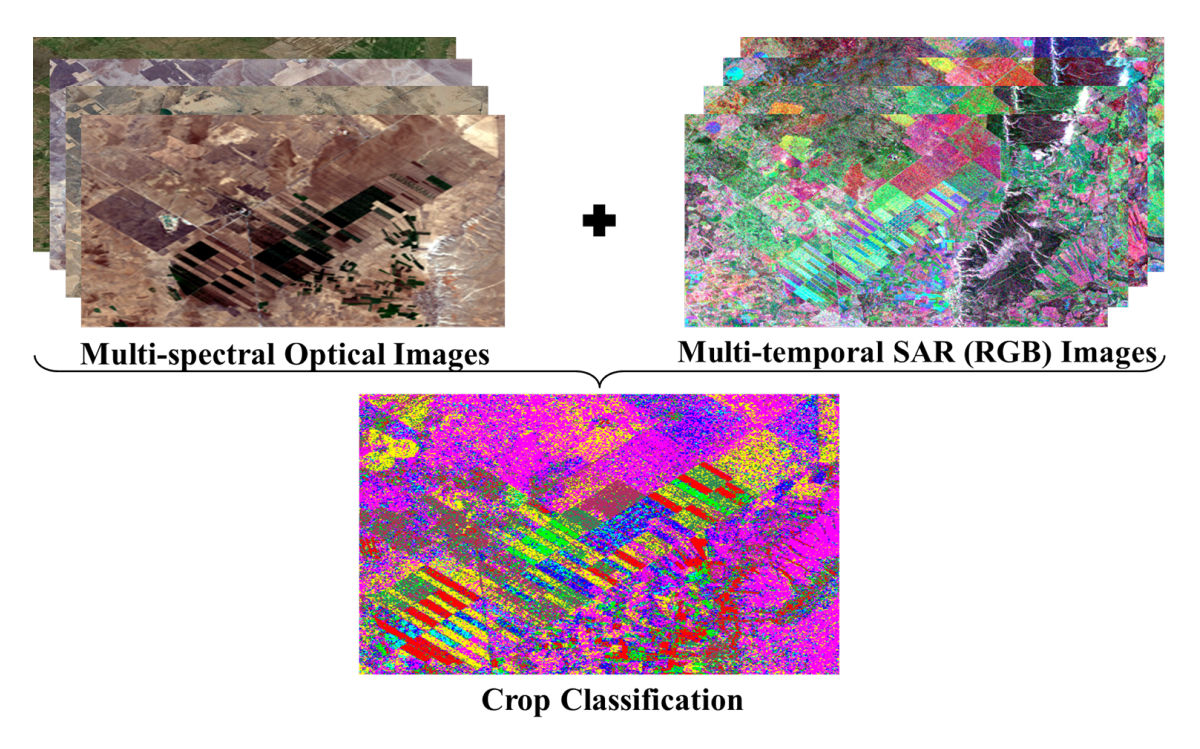


Figure 6.16 Crop classification methodology

6.2.1 Ground truth data acquisition

Field observation data are required to train the supervised classification models as well as to assess the accuracy of produced maps. In order to digitize the selected locations of the spectrally homogeneous Regions of Interest (ROIs) information obtained from field surveys is needed [135]. Crop information is collected on a field by field basis through an in-situ survey. In-situ measurements for under investigation site was conducted in the spring-summer agricultural season of the year 2016 for Potato, Sunflower, Maize, and Wheat fields. During the different field surveys, crop type,

crop height, canopy coverage of the crop, soil moisture and irrigation practices data were collected. The in-situ measurement periods were arranged regarding the general growth stages of the crops accordingly defined by the Biologische Bundesanstalt, bundessortenamt und CHemische industrie (BBCH) [133].

6.2.2 Datasets

In this study, high resolution multi-temporal optical (Sentinel-2) and dual polarimetric (VV and VH) C-band radar data (Sentinel-1) are used for the investigation area. The Sentinel-2 Multispectral Instrument (MSI) wide-swath, high- resolution imaging mission is equipped with 13 spectral bands: four bands at 10 m, six bands at 20 m and three bands at 60 m spatial resolution. It consists of a 12-bit radiometric resolution.

6.2.3 SAR Image Pre-processing

Sentinel-1 images were acquired in ascending orbit direction, Interferometric Wide swath (IW) mode Level-1 C-band Ground Range Detected (GRD) product that consist of focused SAR data which has been detected, multi-looked and projected to ground range using an earth ellipsoid model such as World Geodetic System 1984 (WGS84) (Table 6.5). Pre-processing steps such as Thermal Noise Removal, Apply Orbit File, Radiometric Calibration, Speckle Filtering, Range-Doppler Terrain Correction using SRTM 3-arc-second data and co-registration were performed with open source tools of Sentinel Application Platform (SNAP) software [136]. The work flow of multi-temporal mapping is shown in Figure 6.17. As a last step of the pre- processing chain, pixel digital numbers were converted to sigma nought in decibel (dB). A RGB (Red, Green and Blue) color composite of multi-temporal SAR image of study area is shown in Figure 6.18.

Table 6.5 Specifications of Sentinel-1 and Sentinel-2

Characteristics	Acquisition
of Sensor	Date
Satellite: Sentinel-1	01 July 2016
Wavelength: C-band	13 July 2016
Imaging mode: IW-GRD	25 July 2016
Orbit: Ascending	
Resolution: 19.93 (Rg. and Az)	
Polarization: VH and VV	
Satellite: Sentinel-2	11 July 2016
Imaging mode: MSI-Level-1C	
Resolution: 10 m (B8-B4-B3)	

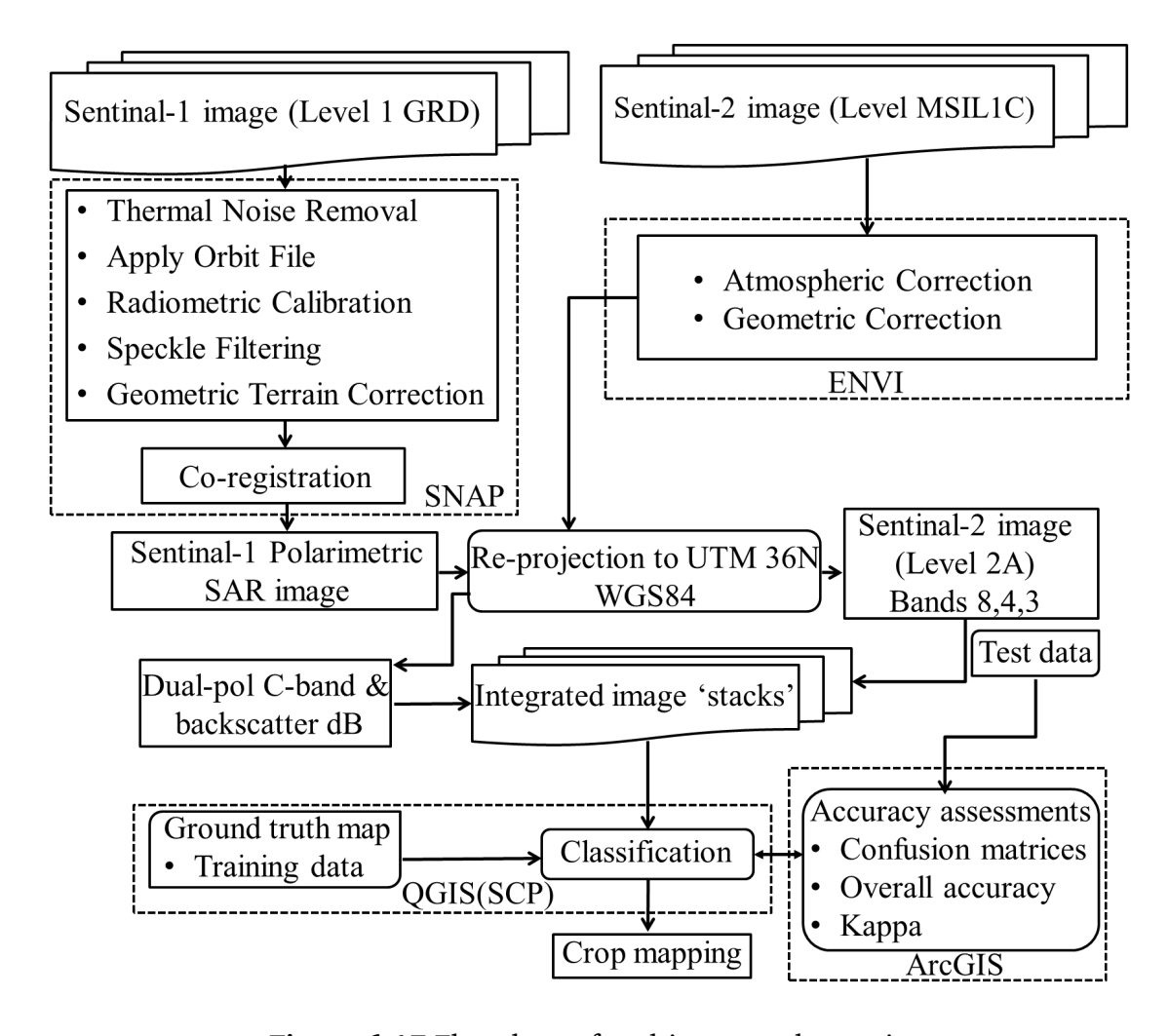


Figure 6.17 Flowchart of multi-temporal mapping

Output values of radiometric calibration indicated by Sigma0 as a parameter for backscattering value. It means that if there is reflectance value in the optical data, there is similar value in the radar data as a backscatter that is measured by a parameter called Sigma0. It has value between 0 and 1 where the higher backscatter the higher Sigma0 values and close to 1. As Sentinel-1 produces dual polarimetric data (VV and VH) the calibration operator will produce a single Sigma0 band for each polarization ($Sigma0_VV, Sigma0_VH$). Geometric correction is next step of SAR data per-processing where SAR geometric distortions would be corrected and using a Digital Elevation Model (DEM) and producing a map projected and geocoded product. The output map projection is Geographic Latitude/Longitude. In order to clean up some of the speckle inherent in SAR images and to normalize the high frequencies and De-speckling, a low pass filter is applied.

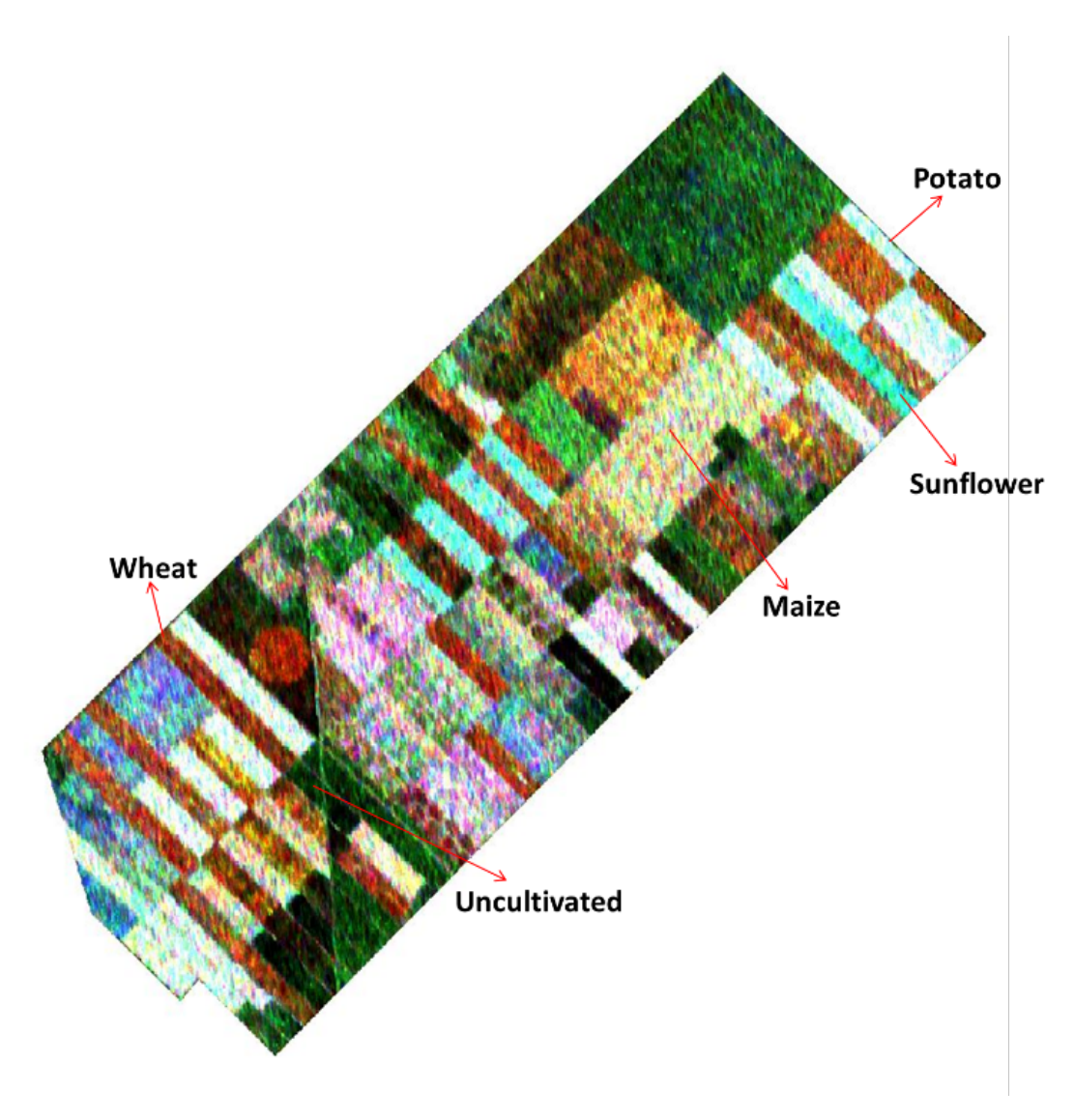


Figure 6.18 RGB color composite of Sentinel-1, (R: 2016.07.01_VH_dB, G: 2016.07.13 VV dB, B: 2016.07.25 VH dB)

6.2.4 Optical Image Pre-processing

For geometric correction of Sentinel-2 data, one needs to define the coordinate system just by opening the sentinel-2 data in the Environment for Visualizing Images (ENVI) software [137] environment and then exporting of data would specify its coordinate system. This method is not a usual procedure for specification of coordinate system, since ENVI is not able to open XML data format of the Sentinel then this help to store XML data for data file. Hence for layer stacking of different Sentinel-2 bands in ENVI following method would be useful. Therefore, each selected band is saved as ENVI.dat format which could be used in layer stacking stage for create Sentinel-2 datasets.

In *IMG_DATA* file into the Sentinel-2 data three bands; Near-Infrared (band 8), Red (band 4) and Green (band 3) selected as basis for geometric correction. Then each selected band is saved as ENVI data format. Data in .dat format could be used in layer stacking stage for create Sentinel-2 datasets. It is necessary to note that in layer stacking, bands should be reordered from short wavelength to long wavelength (1.Near-Infrared, 2.Red and 3.Green) respectively.

Sentinel-2 Level-1C product is Top of Atmosphere (TOA) reflectance image and for classification purposes it is required to atmospheric reflectance correction to obtain Bottom of Atmosphere (BOA) reflectance image (Level-2A product). In order to produce BOA reflectance images, ENVI provides the FLAASH Module [138] that corrects wavelengths in the visible through near-infrared and shortwave infrared regions.

6.2.5 Combination of SAR and optical data

Concepts of data combination and data fusion are aligned to each other whereas they are not exactly coinciding each other. In combination process, data are unified so that integrated data can be used together as a dataset for the different post-processing purposes. While in fusion process, the images are merged into each other and as a result of this merging, a new image is produced that containing the information of the two merged images.

This study describe how to get information from combined optical and SAR data (of Sentinel satellites). For this reason, two different Sentinels data types in a same period of time and same scene has been selected. Per-processing and preparation of each optical and SAR data and combination of per-processed data are two steps implemented to the Sentinels data combination. Combined datasets have been used as input data for different processing purposes such as data analysis, data interpretation,

modelling biophysical variables, classification etc.

To create a combined dataset, Sentinel-1 (VV_dB, VH_dB) and Sentinel-2 (Near-Infrared, Red and Green) data as two different data files, for geographical similarity should be resizing from a specific location. Each dataset should be resized separately to produce spatial subset. Finally, both resized datasets would be combined by applying layer stacking operator to create unique dataset combination including optical and SAR data (Figure 6.19). It must be considered that in this case which two Sentinels data were combined, as both data have been collected from same generation sensors with many similarities in terms of their imaging geometries so that co-registration process was not necessary. However, if combination of two datasets acquired from two different satellites (for example combining Landsat and Sentinel datasets) to be considered as the data are provided from two different sensor types due to their distinct imaging geometries and different angle of view then co-registration would be important to avoid any spatial deviation between optical and radar data.

6.2.6 Crop Mapping

Pixel based image classification is conducted to map the multi temporal coverage of the seasonal crops. Morphological features are created by applying appropriate bands selections and pre-classification is implemented and followed by pixel-level inputs in traditional classification algorithms (e.g., Maximum Likelihood Classification (MLC)). Results were analyzed comprehensively and comparatively. Figure 6.20 shows the crop classification map resulted from the combined SAR and optical dataset as an input data by applying the MLC supervised classification method. QGIS Semi-Automatic Classification plugins (SCP) [139] is applied for post-processing and classification of combined Sentinels image.

6.2.7 Accuracy Assessment

Land use map were produced after pixel-based image classification first for SAR color composite and then for the combined SAR and Optical datasets. Accuracy assessment was conducted on the classified crop map with a total of 38 fields by comparing the final results with reference data obtained from the field campaign to evaluate the quality of the map. Overall accuracy, producer's and user's accuracy were computed for each class from the SAR only and the combined SAR and Optical dataset classification maps. Kappa statistics were calculated from confusion matrix (Figure 6.21 and 6.22). ArcMap as an Esri's ArcGIS [140] component application for geospatial processing programs, is used for computing the accuracy assessment.

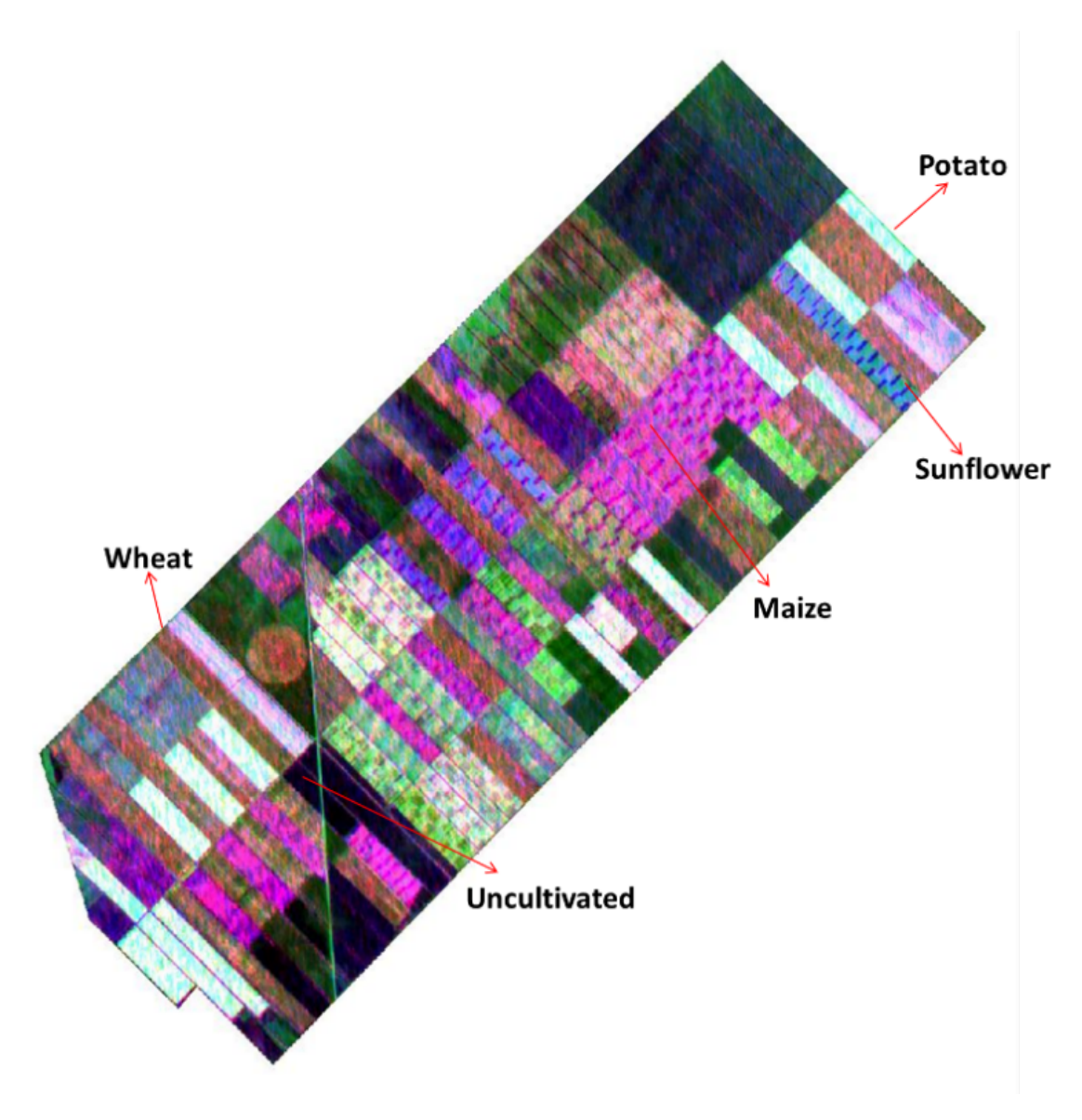


Figure 6.19 Sentinels combined dataset (R: Near-Infrared, G: Red, B: $2016.07.25_VH_dB$)

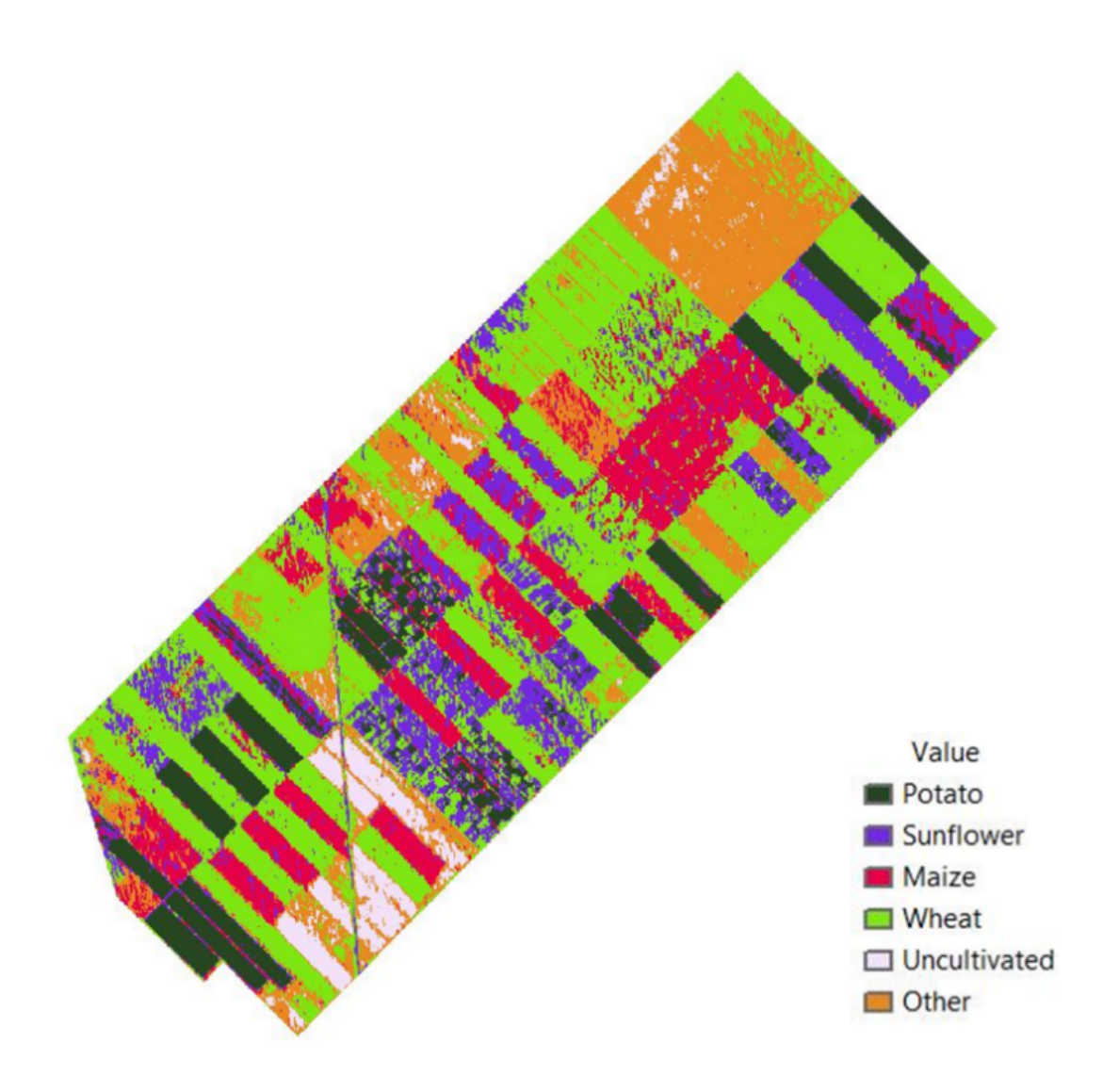


Figure 6.20 Crop classification of combined dataset (MLC)

An overall accuracy of 93% and Kappa value of 0.91 was achieved for the classification map of the combined dataset while for the SAR only classification map, overall accuracy and Kappa value were obtained 88% and 0.86, respectively. The results indicate that combinations of microwave with optical data improved the results (5%).

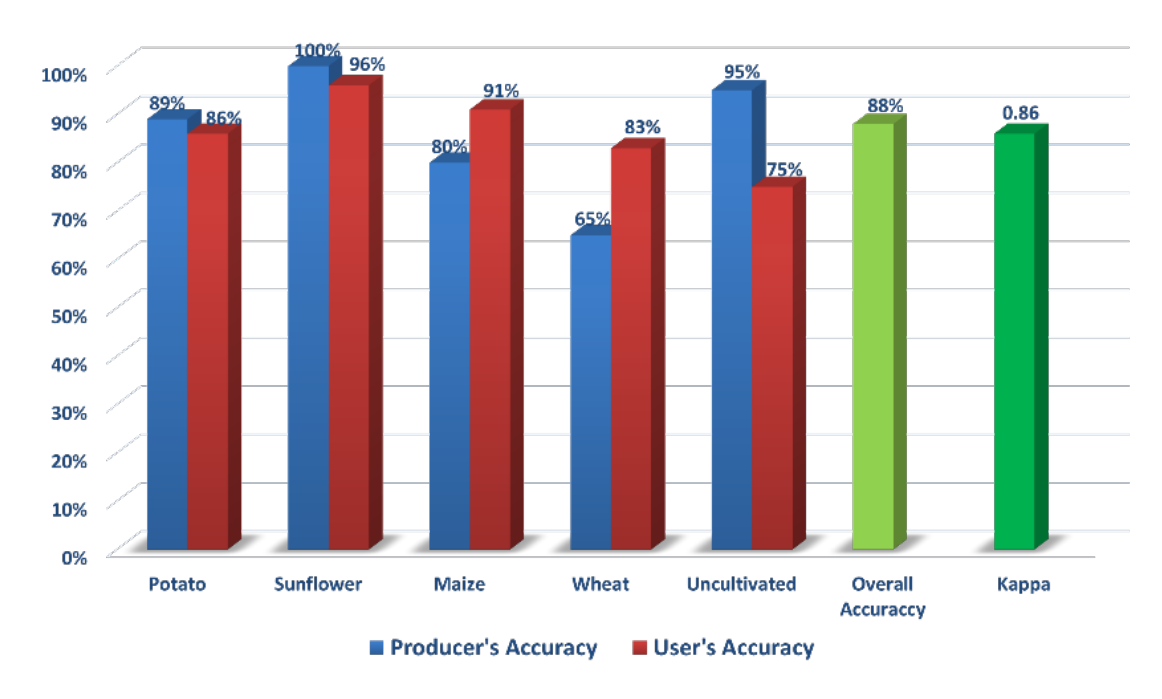


Figure 6.21 Producer, User and Overall accuracies and Kappa coefficient assessment of only Sentinel-1 SAR data

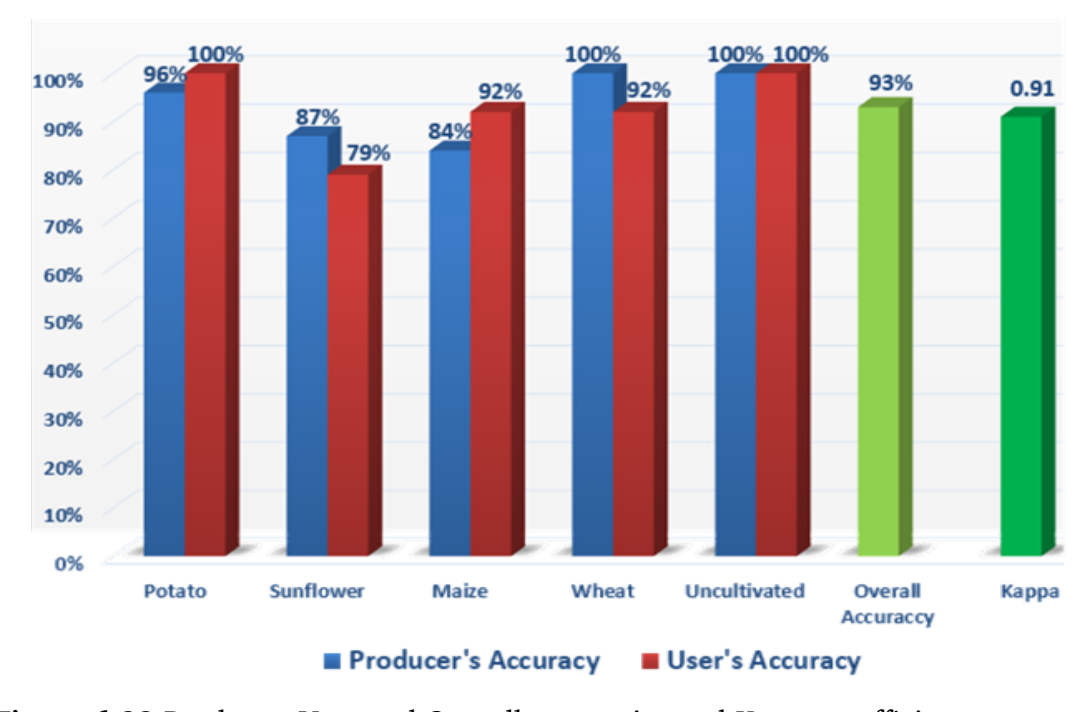


Figure 6.22 Producer, User and Overall accuracies and Kappa coefficient assessment of combined dataset

6.3 Multi-temporal data analysis for crops growth monitoring and identification of different crop types

The application of SAR data is very useful in agricultural monitoring due to the sensitivity of the microwave wavelength to the several characteristics of the crops. The SAR system has sensitivity to the physical morphology and the geometrical characteristics of the land surface and cover (soil roughness and moisture, vegetation structure, etc.). This study investigates the potential of Sentinel-1 polarimetric SAR backscatter data in an agricultural area for growth monitoring of different crop types (maize, sunflower, wheat and potato) and crop mapping using that polarimetric composite of images which are produced from multi-temporal analysis.

In-situ measurements for under investigating site was conducted for maize, sunflower wheat and potato fields in the springng-summer agricultural season of the year 2016. Among the various agricultural products in the study area due to their different structures maize, sunflower, wheat and potato are four investigated crops patterns. Maize, sunflower and potato based on filed measurements, generally are cultivated at the beginning of April to mid-May and harvested in August or the beginning of September in this study area. Winter wheat is seeded in previous October and harvested in July. During the field work, crop variables and parameters that indicate the growth rate of the crops including crop height and canopy coverage are recorded. In addition, field characteristics such as soil properties and irrigation status were collected in the field surveys. The in-situ measurements were conducted according the four main development periods including leaf development, stem elongation, heading and flowering stages of the crops that has been defined under Biologische Bundesanstalt, bundessortenamt und CHemische industrie Sacle (BBCH- Sacle) [133]. Figure 6.23 indicates the crop calendar for maize, sunflower, wheat and potato in the study area.

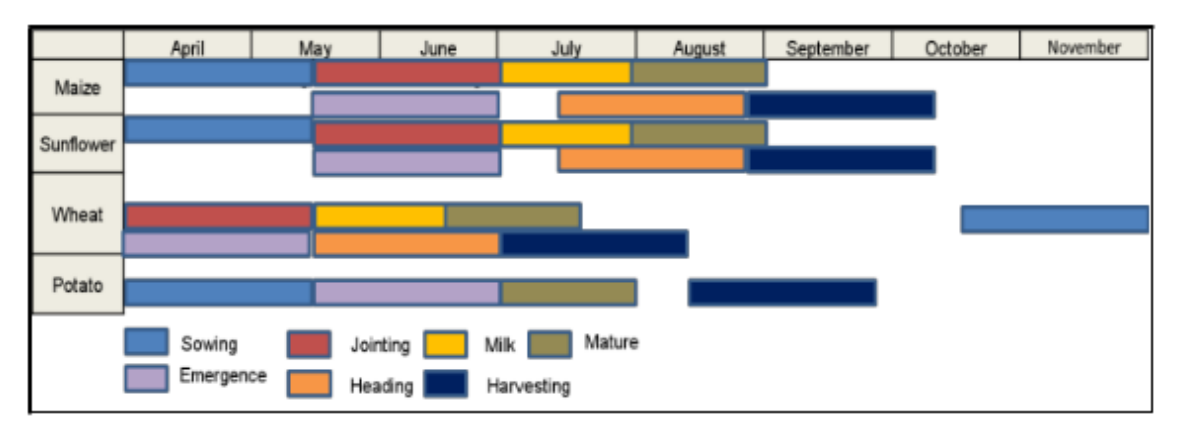


Figure 6.23 Seasonal maize, sunflower, wheat and potato calendar in the study area

6.3.1 Sentinel-1 SAR data statement and processing

Sentinel-1 Interferometric Wide swath (IW) mode images were acquired in both ascending and descending orbit pass directions. We used Level-1 C-band Ground Range Detected (GRD) products that consist of focused SAR data which has been detected, multi-looked and projected to ground range using an Earth ellipsoid model such as WGS84. The satellite obtains data with dual-polarization (VV and VH) backscatter. For the intensity analysis of SAR backscatter to crops, a time series of 24 remotely sensed Sentinel-1 SAR data in ascending and 23 data in descending pass direction were acquired starting from 02 May to 24 September in 2016. Processing steps as radiometric calibration, speckle filtering, topographic correction using SRTM second data and co-registration were performed with open source tools of Sentinel Application Platform (SNAP) software [136]. As a last step, pixel digital numbers were converted to sigma nought in decibel (dB). Spatial subset operation is applied to resize the images to reduce the amount of processing time. Flowchart of multi-temporal Sentinel-1 SAR data processing is shown in Figure 6.24. As a post-processing step,

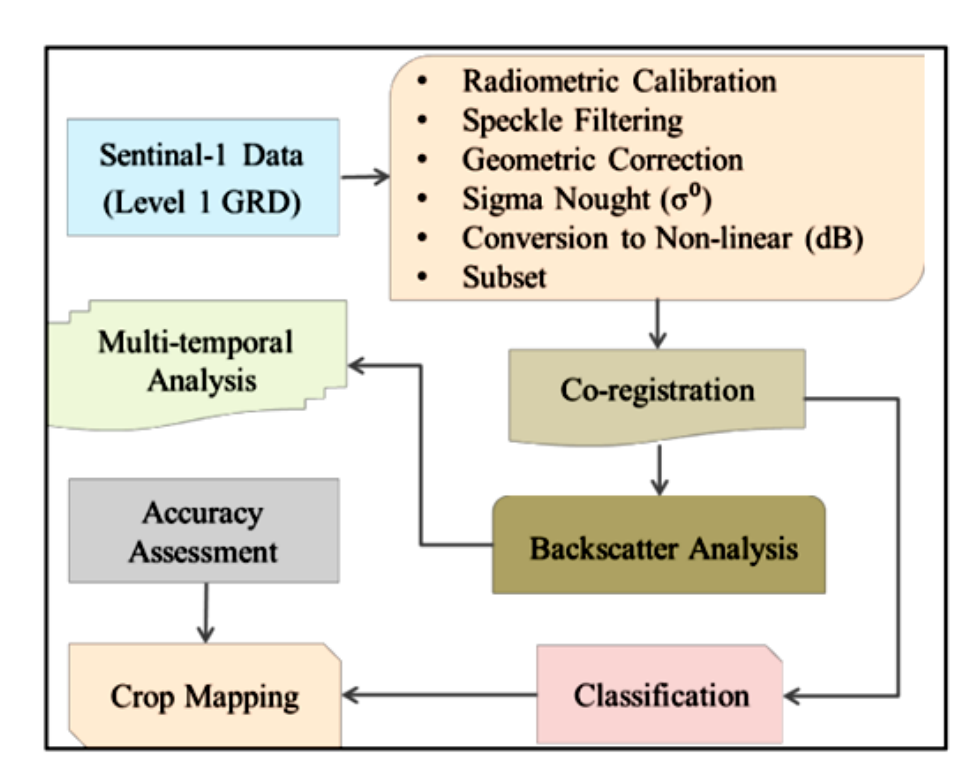


Figure 6.24 Workflow of multi-temporal SAR analysis

Maximum Likelihood Classification (MLC) method is used for crop classification of SAR dataset to map the multi-temporal coverage of the seasonal crops in the study area. Six different classes consist of Potato, Sunflower, Maize, Wheat, Uncultivated and Bare Soil used to provide reliable crop map. Overall accuracy and kappa coefficient are calculated from confusion matrix to evaluate the quality of the crop map. Classification process was performed using Semi- Automatic Classification

6.3.2 SAR backscattering analysis

The backscatters of individual pixels were determined and the correlation between the field measurements was evaluated by analysing multi-temporal SAR images for each field with different crop types. Then the backscatter signature of the selected individual pixels for all patterns in the same plot as well as backscattering value changes for each crop types with different fields during the timeframe of the study were interpreted. Figures 6.25 and 6.26 show the variation of the mean backscatter value of each pattern in the timeframe of the study in ascending and descending orbit pass modes in VH and VV polarizations. While the mean backscatter values of selected pixels for each crop types change between -11dB and -26dB in VH polarization in ascending orbit direction, the values vary between -4dB and -19dB in VV polarized images in the same orbit pass. These values show variation between -11dB and -27dB in VH and -4dB and -18dB in VV polarizations in descending pass mode. The backscatter results show that the satellite orbit pass directions did not affect the intensity values; whereas, in different polarizations change in values is considerable. In Figures 6.25 and 6.26, mean backscatter value of all crop types at the early stages of the crops present a relatively homogeneous intensity values. Whereas in the growing stages (mid stage) of the crops, due to differences in physical structure of the crops and the sensitivity of the SAR to the geometrical characteristics of the patterns, each crop types has high differences in backscatter values. It can be interpreted that in later stages of the crops there is a similarity in the backscatter value. According the field measurements, this point shows the end of the heading and beginning of the harvesting time. Time-series backscatter analysis gives very useful information when one crop type in various fields is intended to be observed in terms of the monitoring programs and management practices. The results also indicate that there is relationship between Sentinel-1 SAR backscatter values and crop variables such as crop height and crop coverage during the different phonological stages [142].

6.3.3 Crop mapping

In addition to the multi-temporal SAR backscattering analysis, polarimetric composite of the images of the different polarization over time without classification methods may also provide beneficial information regarding the identification of crop types. Figure 6.27 displays the polarimetric color composite images of Sentinel-1 in three observation times and each pin in the image represents one crop type. Identification of crop types is validated with the application of classification methods in the study

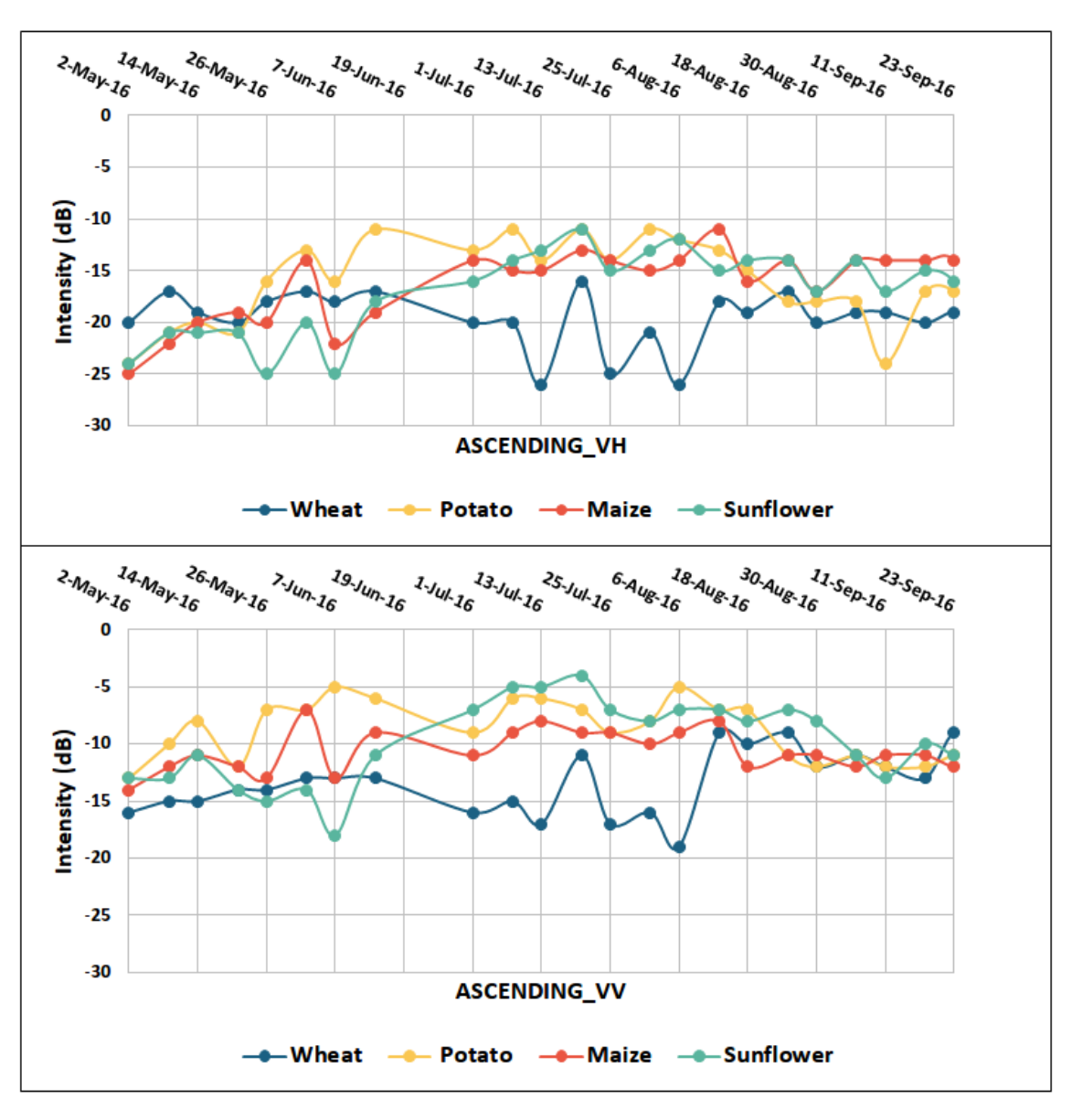


Figure 6.25 The backscatter value of maize, sunflower, wheat and potato on multi-temporal Sentinel-1 images, in ascending pass direction with VH **(top)** and VV **(bottom)** polarization

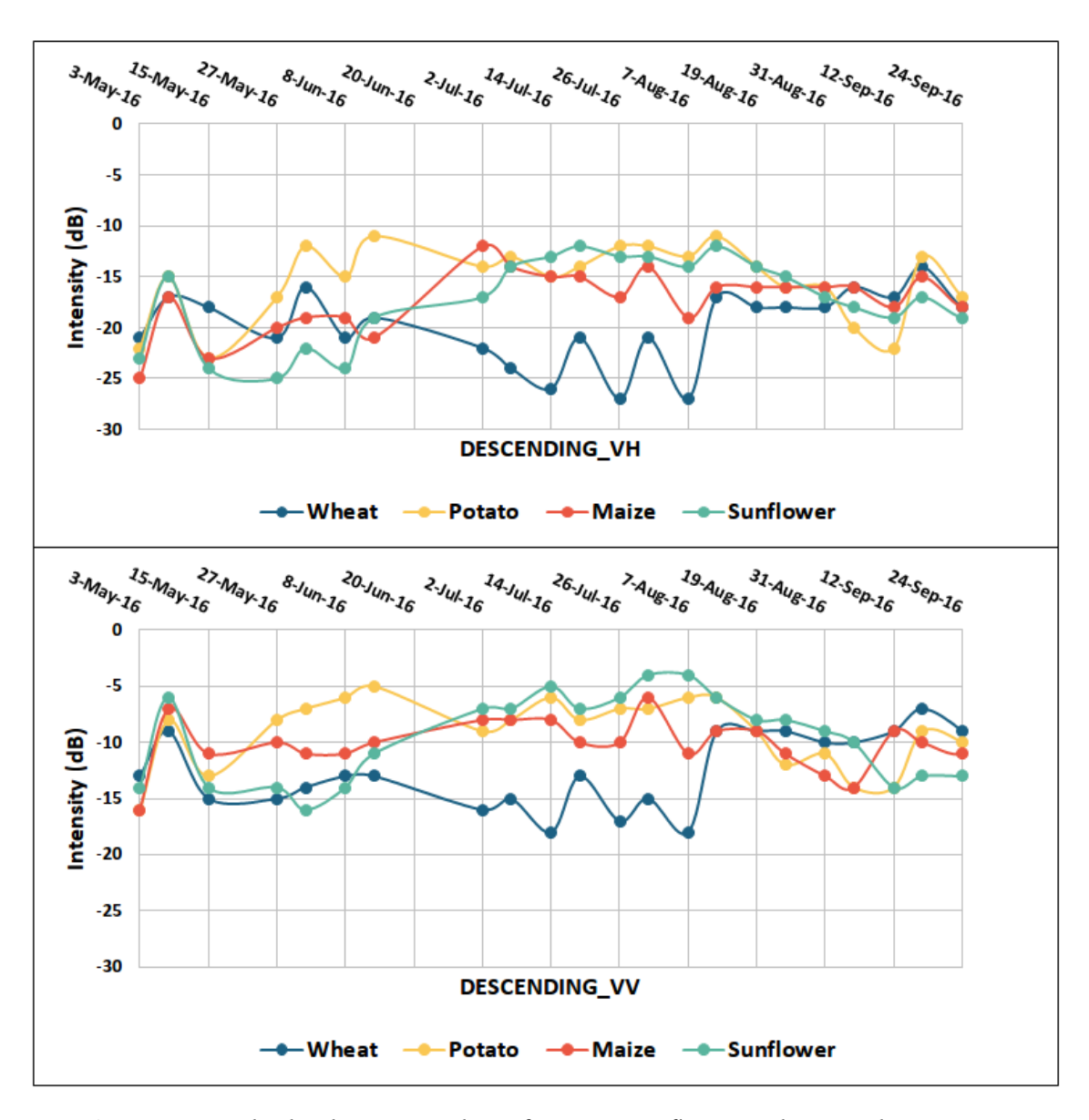


Figure 6.26 The backscatter value of maize, sunflower, wheat and potato on multi-temporal Sentinel-1 images, in descending pass direction with VH **(top)** and VV **(bottom** polarization

area.

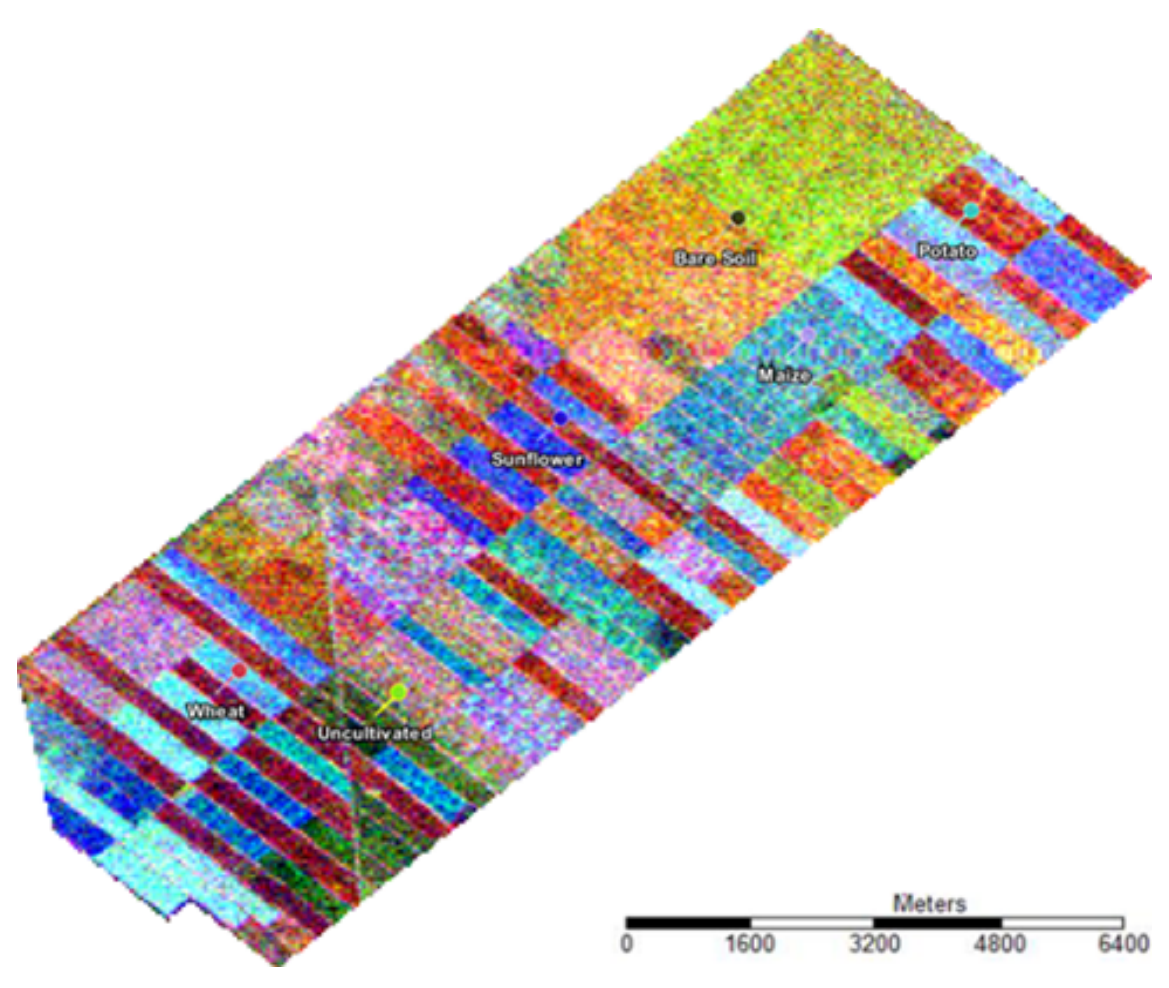


Figure 6.27 RGB color composite using multi-temporal Sentinel-1 SAR data in descending pass direction (**R:** 2016.05.15_*VH*_*dB*, **G:** 2016.06.01_*VV*_*dB*, **B:** 2016.07.31 *VH dB*)

6.3.4 Accuracy assessment of crop classification

The classification has been done based on SAR backscatter values and their temporal changes in each class. Confusion (error) matrix (Table 6.6) was applied to evaluate the accuracy of the multi-temporal SAR-derived crop map and determination of the accuracy of the classification process. The confusion matrix just compares the reference points (test data) to the classified points (training data). Overall, produce and user accuracies, Kappa coefficient, the commission error and the omission error for each class were calculated from confusion matrix (Table 6.7). Crop map were produced after pixel-based image classification for multi-temporal SAR color composite image (Figure 6.28). The results showed that high overall accuracy of 88% and Kappa coefficient of 0.83 has been obtained (Figure 6.29).

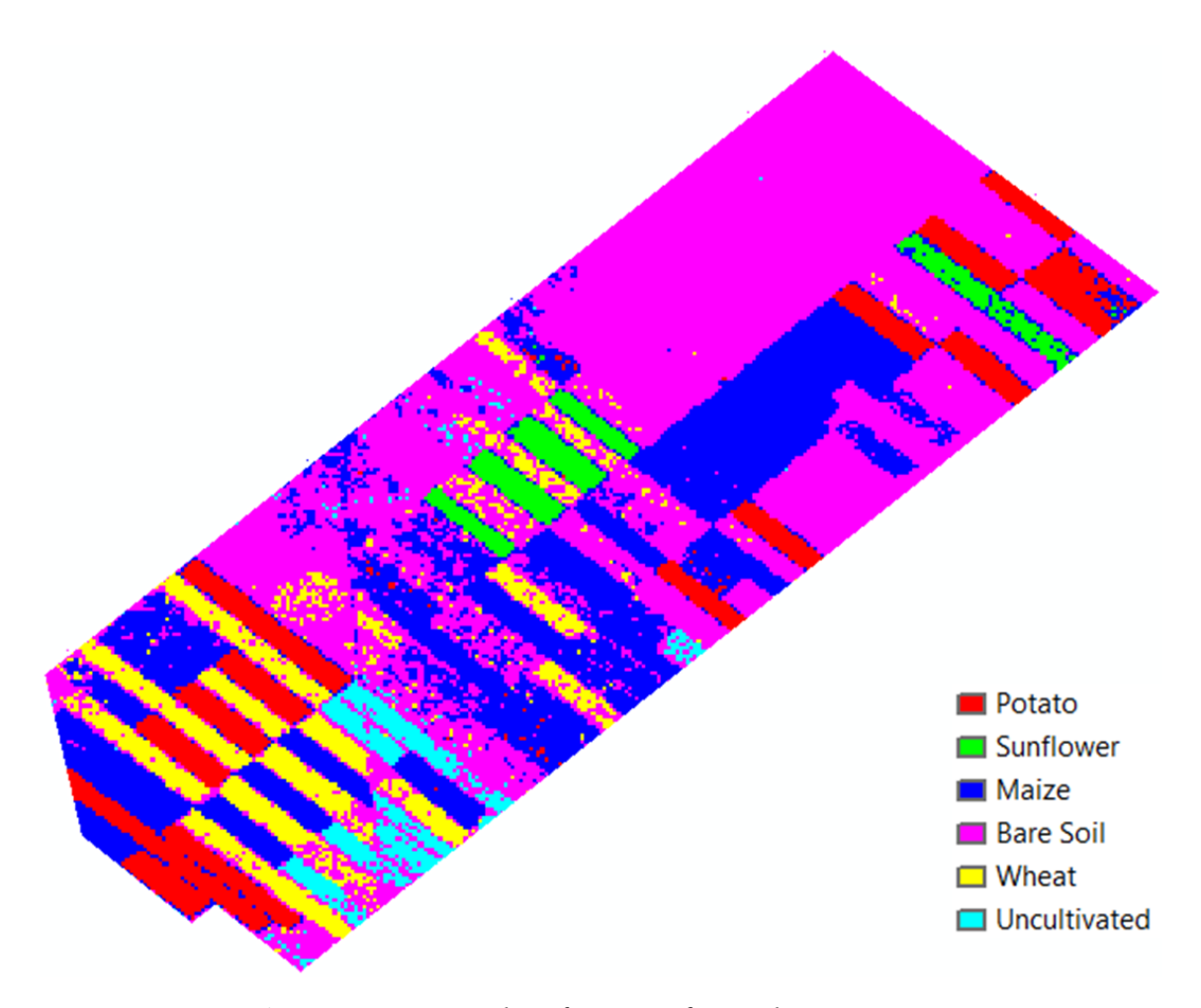


Figure 6.28 Crop classification of SAR dataset (MLC)

Table 6.6 Maximum Likelihood classification confusion matrix

Class	Potato	Sunflower	Maize	Wheat	Uncult. ¹	Bare ²	Total
Potato	279	1	36	0	0	1	317
Sunflower	27	105	56	1	0	0	189
Maize	39	18	375	0	1	7	440
Wheat	0	1	1	170	9	72	253
Uncult. ¹	0	0	5	10	141	33	189
Bare ²	70	0	3	2	4	1384	1393
Total	345	125	476	183	155	1497	2781

¹Uncultivated ²Bare Soil

Table 6.7 Percentages of errors of omission, errors of commission, Producer's and User's accuracies for each class

Class	Omission	Commission	Producer Accuracy	User Accuracy
Potato	11.99	19.13	80.87	88.01
Sunflower	44.44	16	84	55.56
Maize	14.77	21.22	78.78	85.23
Wheat	32.81	7.11	92.9	67.19
Uncultivated	25.4	9.03	90.97	74.6
Bare soil	0.65	7.55	92.45	99.35

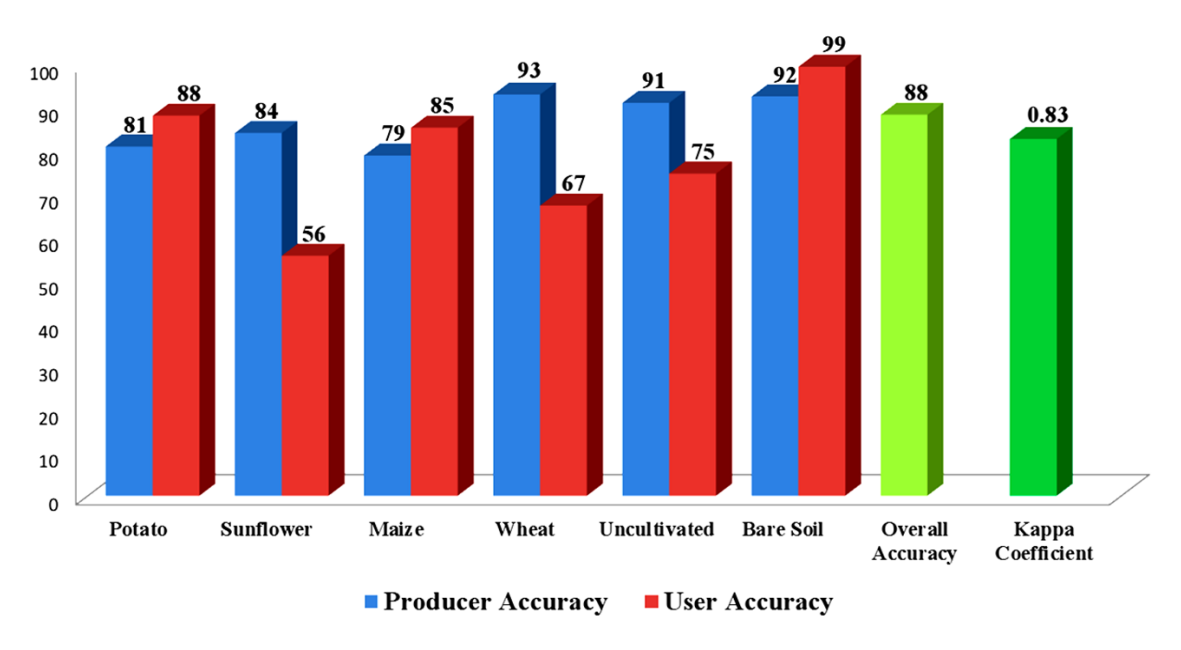


Figure 6.29 Producer's, User's and Overall accuracies and Kappa coefficient assessment of multi-temporal Sentinel-1 SAR data (percentages are rounded to the nearest decimal)

6.4 Interferometric coherence analysis to crop growth monitoring

Sentinel-1 (A and B) satellites with the same generation of sensors and having many compatibilities as to their imaging geometries and the common orbital plane with a 180° phase difference along with small orbital baselines, offer a 6-day interval to formation of the interferometric SAR (InSAR) data pairs for precise surface monitoring and coherent change detection appication. Single Look Complex (SLC) products in the Interferometric Wide swath operation mode (IW) with dual polarization (VV and VH) were acquired for this study. Data is obtained in both ascending and descending orbit pass directions, which means that subject fields could be evaluated from two independent perspectives. From two different tracks in each pass direction in total, 62 SAR data were processed to produce image pairs to obtain interferometric coherence values in relation to crops growth evaluation on the agricultural fields of the study area. Prior to positioning Sentinel-1B in orbit, data were obtained every 12 days for each orbit in the study area, but since end of September, due to its placement into orbit, this period is reduced to 6 days. An overview of datasets with relative orbit number is given in Table 6.8. The images acquisition dates for each orbit from April to September are given in Table 6.9. Two datasets also were obtained for different orbits in October.

Table 6.8 Characteristic parameters of acquired Sentinel-1 datasets

Orbit Number	Satellite Pass	Acquisition Time (UTC)	Swath	Incidence Angle (°)	Resolution (m)	
					S. Range ¹	Azimuth
87	Ascending	15:42	IW3	43.1	3.5	22.6
65	Descending	03:58	IW1	32.9	2.7	22.5
160	Ascending	15:49	IW3	43.1	3.5	22.6
167	Descending	03:50	IW3	43.1	3.5	22.6

¹Slant Range

Generic Mapping Tools Synthetic Aperture Radar (GMTSAR) developed by [143] is used as an open code radar interferometry processing system. The main components of GMTSAR processing system include: 1) a preprocessor for different sensor data type to convert the original data format and its orbital information into a common configuration; 2) an InSAR processor to set the stacks of images for co-registration to eliminate the topographic phase and form the complex interferogram; and 3) a post-processor, based on Generic Mapping Tools (GMT) [144] system, to filter the interferogram and establishment of the interferometric products of phase, amplitude and coherence; to convert the interferometric phase into line-of-sight (LOS) displacement and a geocoding processing to convert the radar image coordinates into geographic coordinates [122].

Table 6.9 Datasets acquisition dates for different orbits

Orbit No.				April					May			
87		3		15		27		9			21	
65	2		14		26					8		
160		8		20			2		14		26	
167	9		21					3		15		27
Orbit No.				June					July			
87		8		20				2	14			
65	1		13				7			19		31
160		7						1	13		25	
167	8						2			14		26
Orbit No.				August					September			
87	1		13		25		6		18		30	
65		12		14		24		5		17		29
160	6		18		30		11		23^1		29	
167		7		19		31		12		24^1		30

¹From these date on for 160 and 167 orbit numbers acquisitions were made every 6 days in September and for all orbits from October

Different-pass Sentinel-1 SAR data was used to calculate interferometric coherence values for agricultural field with different crop types. Figure 6.30 illustrates the acquired Sentinel-1 images locations with related track numbers and satellite orbit pass direction and its LOS position. In this study the correlation between different phenological stages (sowing, growth and harvesting) of the crops and radar coherence were investigated. The results showed that coherence values was high before plowing and seeding and had sharp coherence decrease with starting the growing of the crops. During the growth stage of crops the values stay low and slightly similar for each fields and crop types. The coherence values were significantly higher after crop harvesting and reaping the remnants of the crops. In comparing with ascending pass direction it has indicated that coherence value is high for each field with the same crop type in descending orbit.

6.4.1 Coherence estimation and its relation with crop growth

For each crop type and totally for 20 crop fields vegetation parameters including sowing, growth, and harvesting stages were recorded in the different field measurements. Due to the simultaneous planting of maize and sunflower in the study area, the coherence value was in the highest for both crops at the end of March and early June after plowing the fields and seeding the crop. The value is started to decrease with the growth of the plants. At the beginning of July, once the ground covered by the plant and hence the soil affects eliminated from the radar backscatter, it reaches the lowest value. The coherence again started to get higher

in late September and October for sunflower and maize, respectively, when the crops is reaching to their harvesting time. Since winter wheat is seeded in previous and

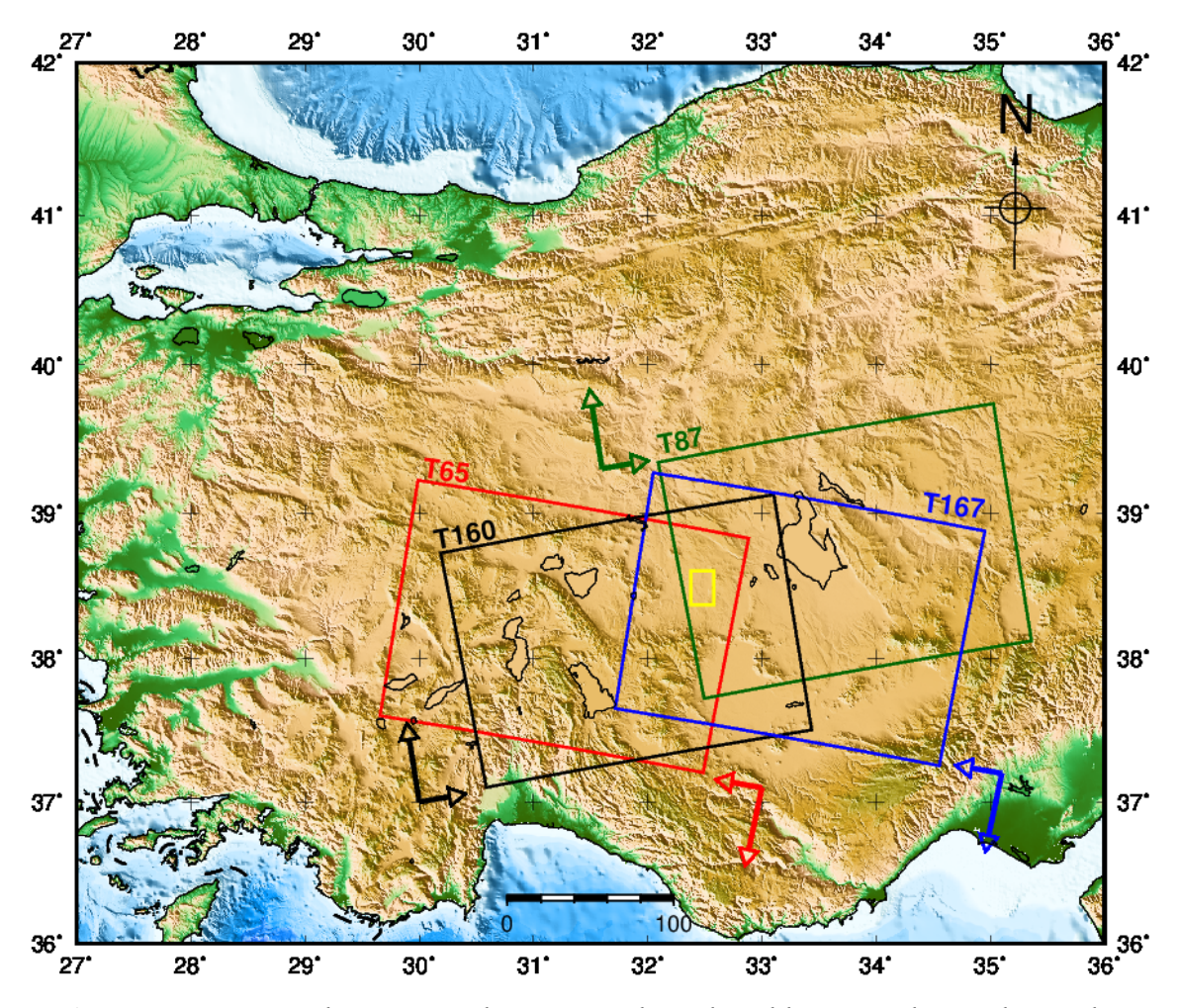


Figure 6.30 Sentinel-1 imagery locations. The colored boxes with *T* indicate the tracks and perpendicular arrows represent satellite propagation direction and its LOS with longer and short arrows respectively and yellow box shows the study area

late October, and interferometric coherence analysis for the wheat is related to the beginning of the April when the crop is its heading stage, therefore, coherence values were low until the harvesting time and after that there is a sharp increases in estimated coherence at the end of June and early July. However, before the crops reaching their harvesting time, an increase observed in the coherence value for maize and sunflower that can be resulted from the changes in weather conditions such as wind, moisture or precipitation. Mean coherence values for maize (9 fields), sunflower (6 fields) and wheat (5 fields) for ascending and descending pass directions in four different tracks for VH and VV polarization are given through Figures 6.30 to 6.35, respectively. In compared with the ascending pass direction, descending represented high interferometric coherence values in all crop types. Between the VV and VH polarization much better coherence values were estimated using VV polarization.

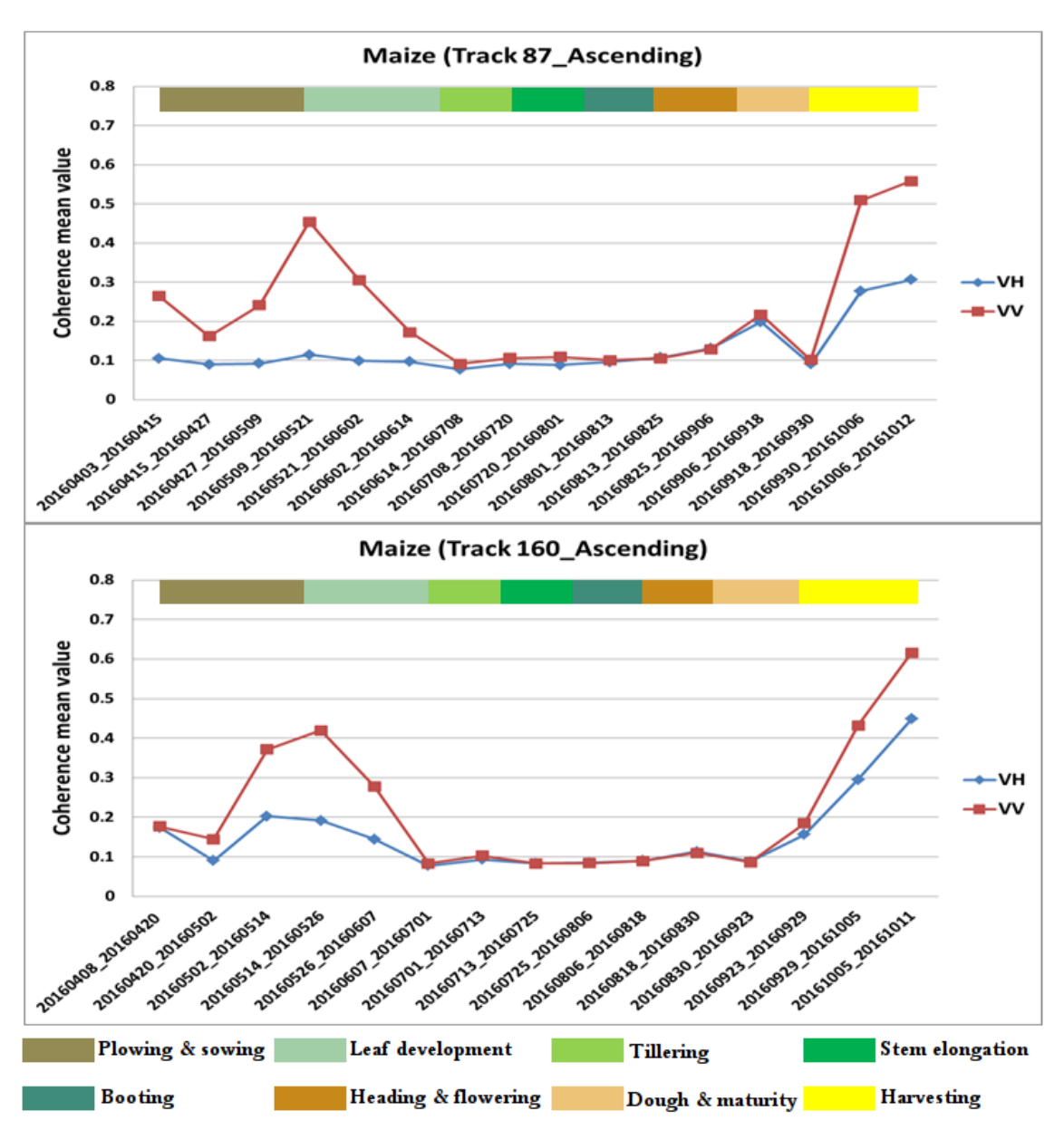


Figure 6.31 Mean Coherence values of 9 maize fields during the seasonal growth stages in the ascending pass direction for VH and VV polarization in two different tracks. The date of images used for coherence pair formation is represented in the x - axis of the graph

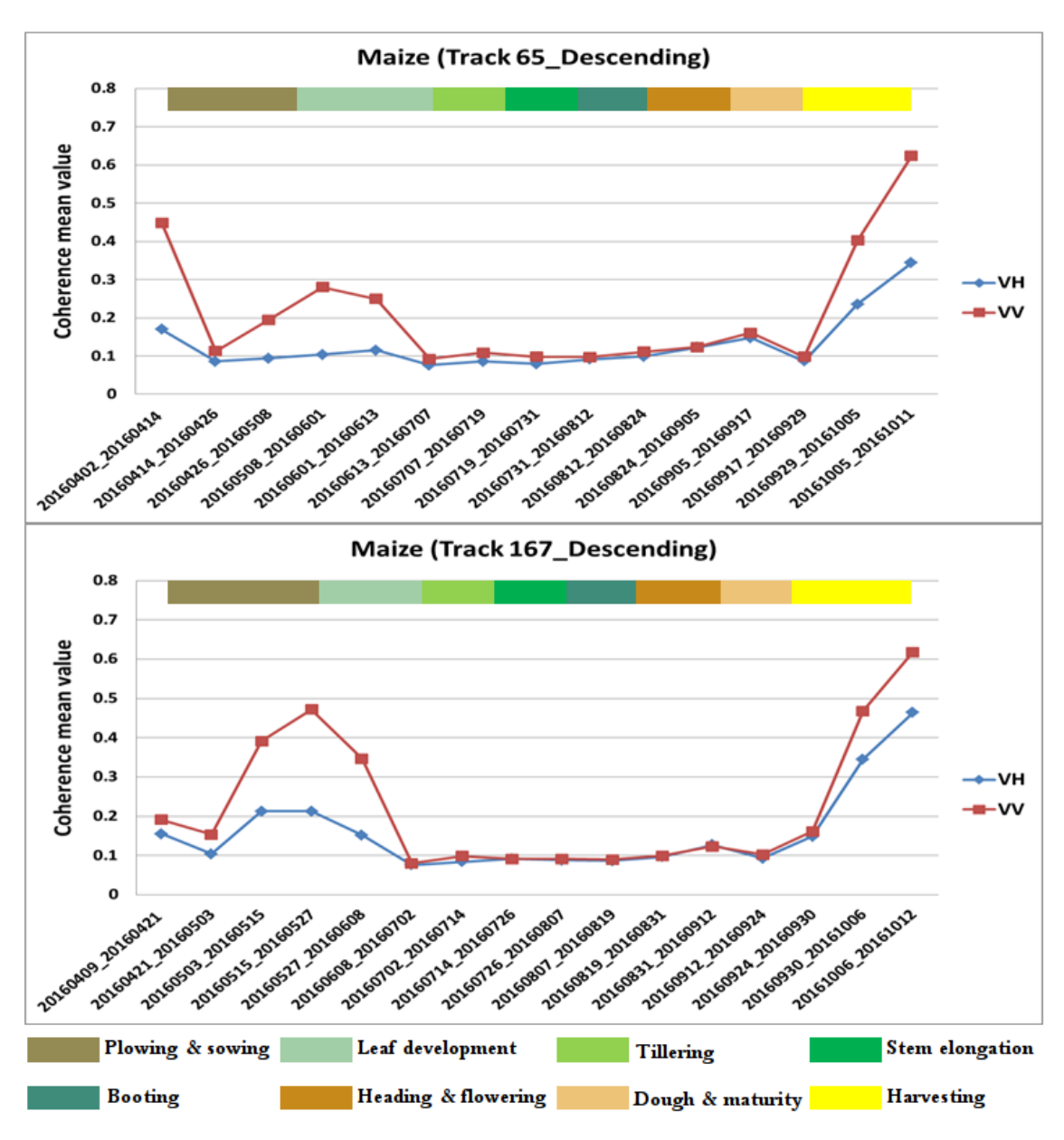


Figure 6.32 Mean Coherence values of 9 maize fields during the seasonal growth stages in the descending pass direction for VH and VV polarization in two different tracks. The date of images used for coherence pair formation is represented in the x - axis of the graph

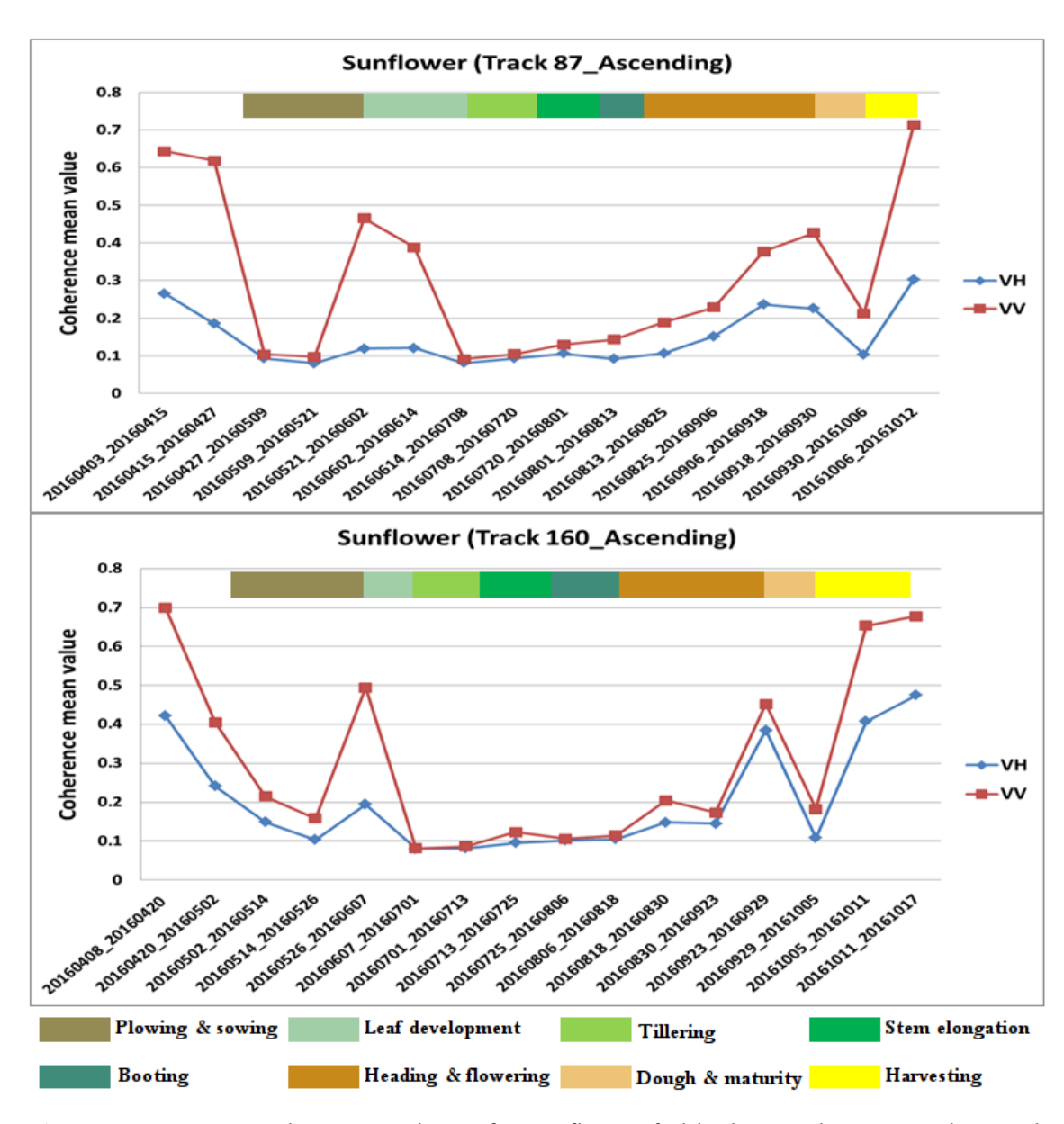


Figure 6.33 Mean Coherence values of 6 sunflower fields during the seasonal growth stages in the ascending pass direction for VH and VV polarization in two different tracks. The date of images used for coherence pair formation is represented in the x-axis of the graph

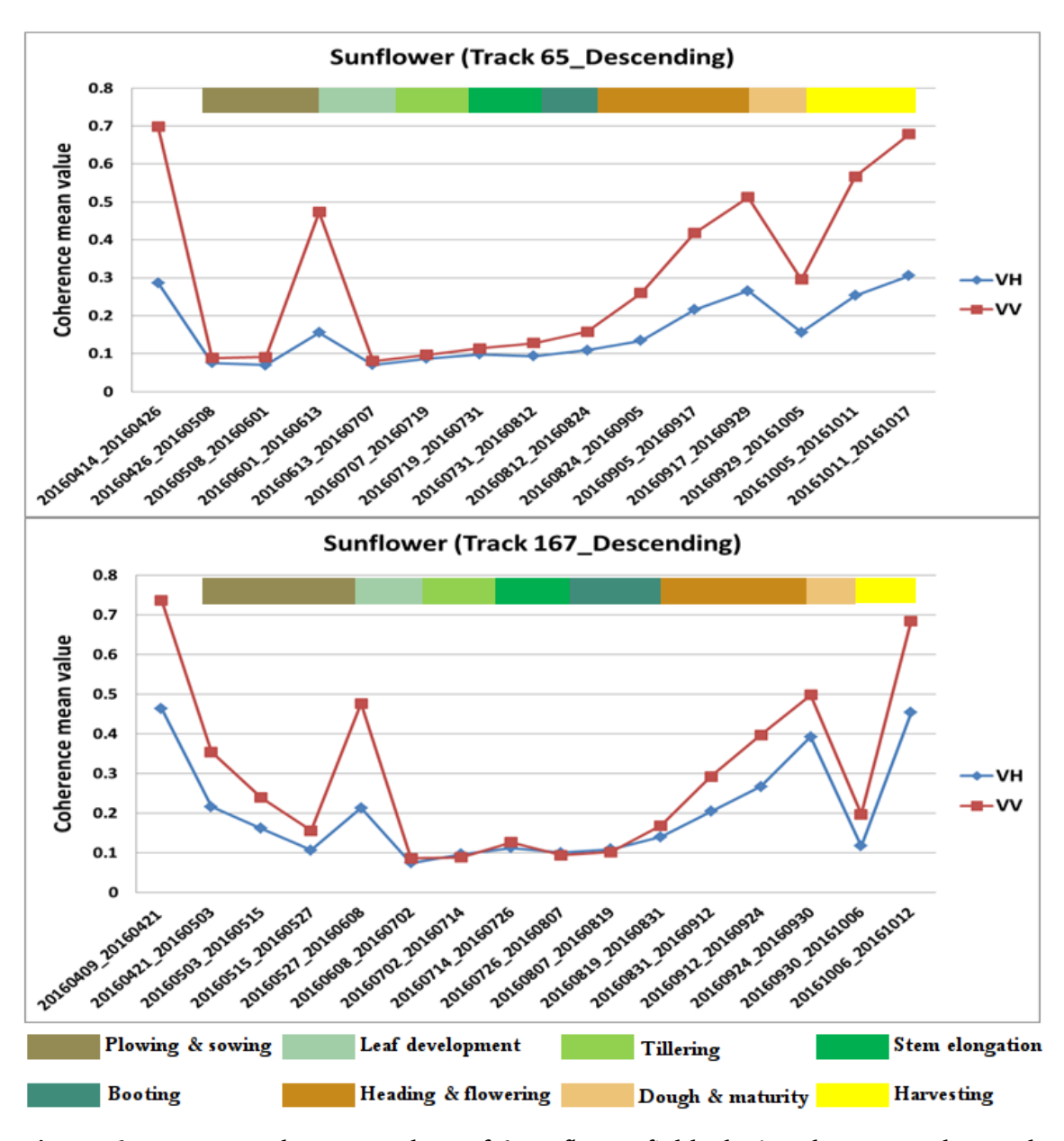


Figure 6.34 Mean Coherence values of 6 sunflower fields during the seasonal growth stages in the descending pass direction for VH and VV polarization in two different tracks. The date of images used for coherence pair formation is represented in the x - axis of the graph

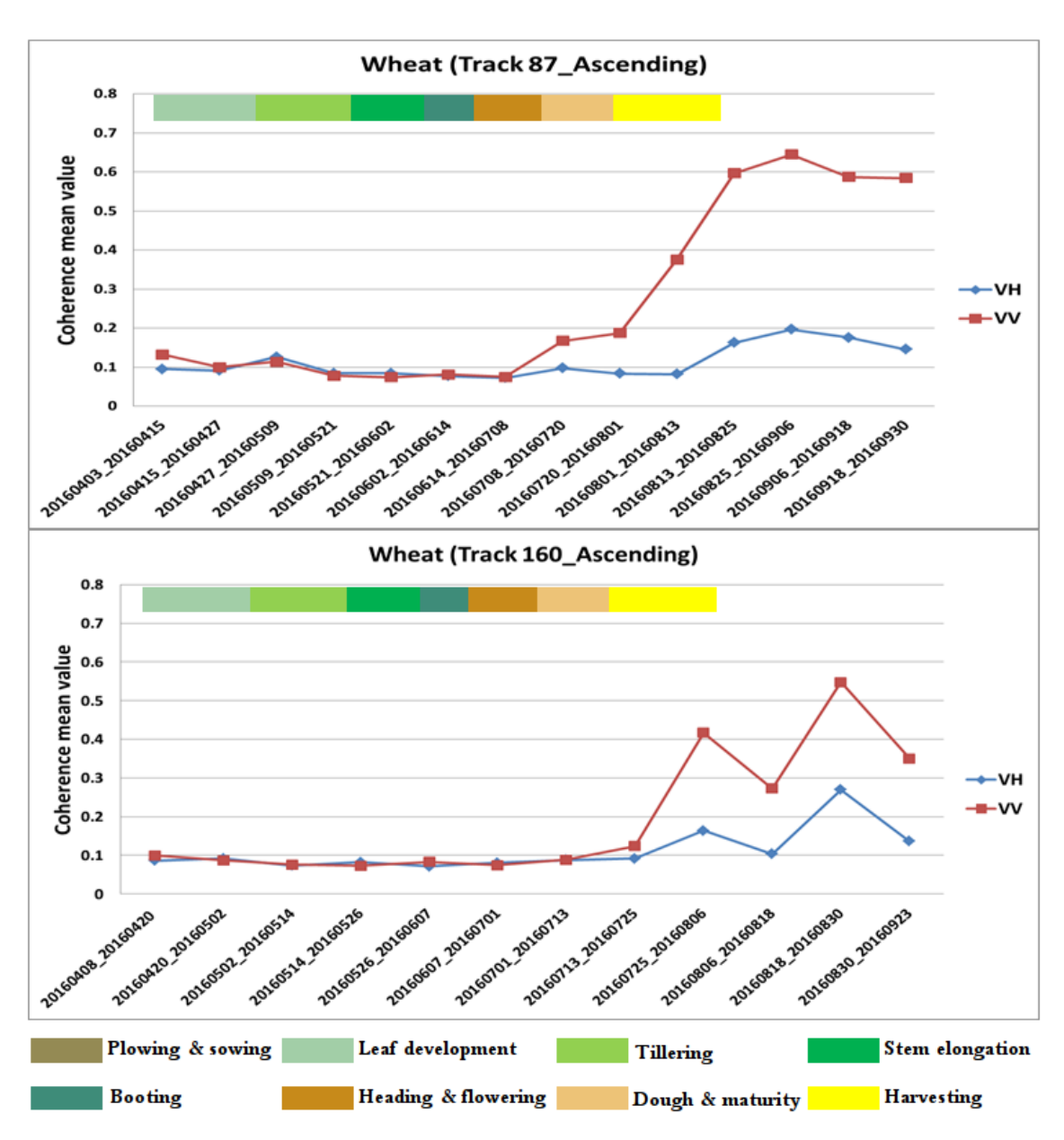


Figure 6.35 Mean Coherence values of 5 wheat fields during the seasonal growth stages in the ascending pass direction for VH and VV polarization in two different tracks. The date of images used for coherence pair formation is represented in the x - axis of the graph

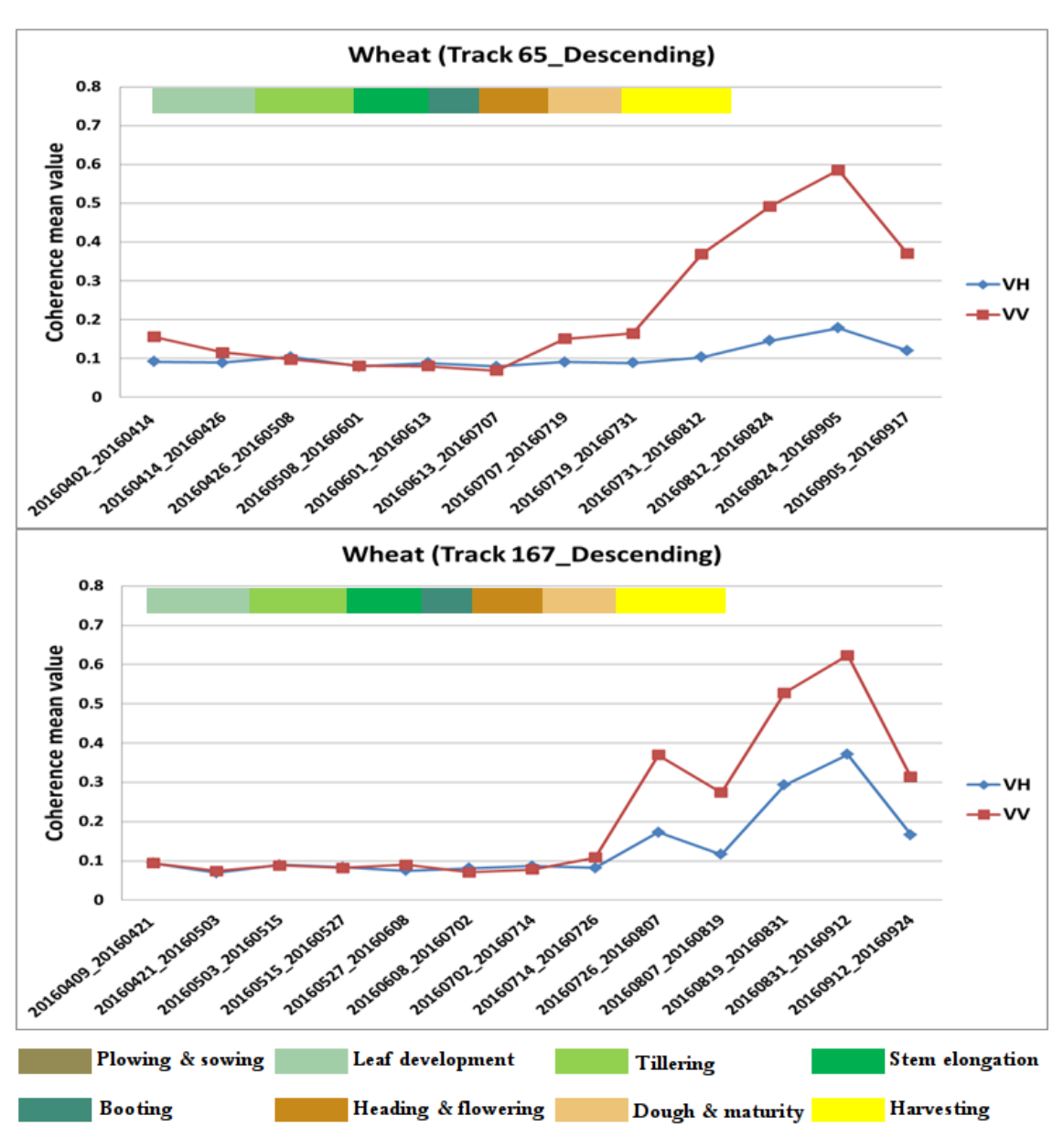


Figure 6.36 Mean Coherence values of 5 wheat fields during the seasonal growth stages in the descending pass direction for VH and VV polarization in two different tracks. The date of images used for coherence pair formation is represented in the x - axis of the graph

Results And Discussion

In application of PolSAR technique for crop monitoring, three different crop types that have "broad" and "narrow" leaves were selected to investigate the sensitivity of the Sentinel-1 dual polarimetric SAR parameters to plant height and canopy coverage (CC). Maize and sunflower is selected as broad leaf and wheat as narrow leaf crop. The reason for studying two broad-leave crops was to validate the high sensitivity of SAR polarimetric data to early stages of broad-leave crops and then comparing the findings for wheat as narrow-leave crop. We demonstrate that maize presents higher correlation during the early stages of the crop growth when the crop height is less than 150 cm. It is strongly correlated with the SAR parameters including VV+VH (R^2 = 0.82), VV (R^2 = 0.81), and VH (R^2 = 0.80). Besides, CC of maize was well correlated with VV polarization ($R^2 = 0.73$) at the early stage before the heading stage although at the later growing stage the correlation becomes weaker after the heading stage. From the backscatter analysis, the same result is not observed in the sunflower. The sunflower height has very low correlation with the most of SAR parameters. Only VH polarization shows slightly better sensitivity when its height is below 92 cm before the ending of flowering and the inflorescence reaches to full size. The sunflower CC is relatively correlated with VV polarization at the early stage (during the flowering stage) while any considerable correlation between SAR parameters and sunflower height and CC is observed at the later stage. The sensitivity of SAR parameters to wheat variables is often low compared to maize and sunflower. The high, but negative correlations are related to the VH/VV intensity ratio and VH polarization. However, Alpha (α) decomposition parameter shows highest correlation at the beginning stage and represents absence of SAR parameters sensitivity with wheat height at the later growing stage and CC at both stages. The results we have obtained reveals that Sentinel-1 dual polarimetric SAR (C-band) has a high potential for identifying growth stages and estimation of crop height, canopy coverage of maize as a broad-leaf crops. However, this is not proven for sunflower, that may be due to the crop structure and leaves geometry since they may change the SAR backscatter value in any stages of crops. This study also demonstrates that Sentinel-1 dual polarimetric SAR data can be a good alternative to other commercial data which enables users to access freely available of a constant long-term data archive for applications requiring long-range time series.

Although the use of single orbit direction (descending) provides possibility of monitoring and investigating agricultural growth stages, future studies should use both the ascending and descending orbits to have independent results from different angles of view. In addition, the relationship between backscatter values of multi-temporal Sentinel-1 data and vegetation variables will be incorporated to improve the crops mapping and classification accuracy as a future work.

Combinations of microwave remote sensing data with optical data considerably improved the results (5%), achieving the excellent classification of croplands and allowed to discriminate the crops for the accurate assessment. Although high spatial resolution and unique color combination are the strengths of optical spectral bands, the application of optical images in a climate condition with a cloudy sky and particularly in rainy weather causes a serious obstacle in monitoring of agricultural activities during most of the growing season. In contrast, a SAR sensor utilizes the microwave portion of the spectrum, which enables radar pulses to penetrate clouds and rain. In addition, radar has capability to collect data in day-or-night. Therefore, in case of optical images being not applicable due to the weather conditions, the integrated use of SAR and optical data is the most suitable option. Moreover, data from the optical and microwave provide complementary information and the combined use, either simultaneously or at different times, can provide important additional information of terrain surface and vegetation canopies.

In multi-temporal data analysis, backscatter values for each crop types (i.e., maize, sunflower, wheat and potato) over the time were determined and the relation between the intensity values and the data obtained from filed campaign was evaluated. Due to the different methods of irrigation and fertilization and the differences in crops physical geometry during the growing stages, different backscatter values are observed for different types of crops. However, at the later stages of the crops growth, due to reaching the harvesting time, similar backscatter values are observed. Moreover, the backscatter signature in timeframe varies considerably over different areas and thus it may not be possible to drive a unique backscatter signature. That is valid for the same crop in all areas although this distribution gives an indication of the differences in backscatter for different crop over time. Regarding the relationship between ascending and descending pass directions with VH and VV polarization, it was demonstrated that early and later stages of crops growth have relatively similar correlation in backscatter values and opposite to this, mid stages showed lower similarity due to

geometrical characteristics of the different crop types. In addition, it has indicated that the homogeneity between SAR backscatters is high for each field with the same crop type in descending pass direction with VH polarization. In conclusion, using the multi-temporal Sentinel-1 SAR data for the agriculture monitoring system which may play an important role for the accurate crop assessment is an ideal preference due to its free availability and a constant long-term data archive.

Interferometric coherence values that calculated from the multi-track repeat-pass SAR data for the agricultural field with different crop types in dealing with acquired information from the field measurements, a very strong correlation between different phenological stages (sowing, growth, and harvesting) of the crops and radar coherence is indicated in the study area. The results declared that before plowing and after seeding the coherence values were high but had sharp coherence decrease with starting the growing the crops. During the growth stage of crops the values stay low and slightly similar for each field and crop type. The coherence values were significantly higher after crop harvesting and reaping the remnants of the crops. In comparing with ascending pass direction it is observed that coherence value is high for each field with the same crop type in descending orbit pass. The increase of values for VV polarization was higher in compared with the VH polarization for different crop types. It can be inferred from the interferometric coherence analysis that several factors and agriculture activities such as plowing, seeding, and precipitation before image acquisitions affect the values.

This study employed remote sensing data which acquired by Sentinel-1 as SAR data and Sentinel-2 as optical images for the different investigation purposes such as sensitivity analysis of the multi-temporal Sentinel-1 SAR parameters to the crop variables, utilizing the multi-temporal Sentinel-1 SAR imagery and Sentinel-2 optical datasets to improve the crop mapping by combination of the datasets, application of Sentinel-1 radar data for time-series analysis to investigate the temporal backscatter changes for different crop types and also Sentinel-1 interferometric coherence analysis to crop growth monitoring. The results demonstrate the high potentialities of the Sentinel-1 dual polarimetric SAR data and multi-spectral Sentinel-2 data due to provide useful information and access freely available of a constant long-term data archive for applications requiring long-range time series such as agricultural activities monitoring and mapping are ideal preference and a good alternative to other commercial data.

- [1] F. Canisius, J. Shang, J. Liu, X. Huang, B. Ma, X. Jiao, X. Geng, J. M. Kovacs, D. Walters, "Tracking crop phenological development using multi-temporal polarimetric Radarsat-2 data," *Remote Sensing of Environment*, vol. 210, pp. 508–518, 2018.
- [2] J. Soria-Ruiz, Y. Fernandez-Ordonez, H. McNairn, "Corn monitoring and crop yield using optical and microwave remote sensing," in *Geoscience and Remote Sensing*, IntechOpen, 2009.
- [3] H. McNairn, C. Champagne, J. Shang, D. Holmstrom, G. Reichert, "Integration of optical and Synthetic Aperture Radar (SAR) imagery for delivering operational annual crop inventories," *ISPRS Journal of Photogrammetry and Remote Sensing*, vol. 64, no. 5, pp. 434–449, 2009.
- [4] W. Zhang T. Yan, "Analysis of advantage on radar remote sensing for agricultural application," in *Proceedings of the Asian Conference on Remote Sensing, Hong Kong, China*, 1999, pp. 22–25.
- [5] S. Aggarwal, "Principles of remote sensing," *Satellite remote sensing and GIS applications in agricultural meteorology*, pp. 23–38, 2004.
- [6] N. Joshi, M. Baumann, A. Ehammer, R. Fensholt, K. Grogan, P. Hostert, M. R. Jepsen, T. Kuemmerle, P. Meyfroidt, E. T. Mitchard, *et al.*, "A review of the application of optical and radar remote sensing data fusion to land use mapping and monitoring," *Remote Sensing*, vol. 8, no. 1, p. 70, 2016.
- [7] F. Bioresita, A. Puissant, A. Stumpf, J.-P. Malet, "A method for automatic and rapid mapping of water surfaces from sentinel-1 imagery," *Remote Sensing*, vol. 10, no. 2, p. 217, 2018.
- [8] J. Rouse Jr, R. Haas, J. Schell, D. Deering, "Monitoring vegetation systems in the great plains with ERTS," 1974.
- [9] D. J. Watson, "Comparative physiological studies on the growth of field crops: I. variation in net assimilation rate and leaf area between species and varieties, and within and between years," *Annals of botany*, vol. 11, no. 41, pp. 41–76, 1947.
- [10] H. Q. Liu A. Huete, "A feedback based modification of the NDVI to minimize canopy background and atmospheric noise," *IEEE transactions on geoscience and remote sensing*, vol. 33, no. 2, pp. 457–465, 1995.
- [11] B.-C. Gao, "NDWI—A normalized difference water index for remote sensing of vegetation liquid water from space," *Remote sensing of environment*, vol. 58, no. 3, pp. 257–266, 1996.

- [12] C. F. Jordan, "Derivation of leaf-area index from quality of light on the forest floor," *Ecology*, vol. 50, no. 4, pp. 663–666, 1969.
- [13] J. Xue B. Su, "Significant remote sensing vegetation indices: A review of developments and applications," *Journal of Sensors*, vol. 2017, 2017.
- [14] H. Meinke, G. L. Hammer, H. van Keulen, R. Rabbinge, B. A. Keating, "Improving wheat simulation capabilities in australia from a cropping systems perspective: Water and nitrogen effects on spring wheat in a semi-arid environment," in *Developments in Crop Science*, vol. 25, Elsevier, 1997, pp. 99–112.
- [15] M. Weiss F. Baret, "Use of remote sensing data for nitrogen management in precision farming," in *IGARSS 2000. IEEE 2000 International Geoscience and Remote Sensing Symposium. Taking the Pulse of the Planet: The Role of Remote Sensing in Managing the Environment. Proceedings (Cat. No. 00CH37120)*, IEEE, vol. 4, 2000, pp. 1468–1470.
- [16] N. Bagheri, H. Ahmadi, S. K. Alavipanah, M. Omid, "Multispectral remote sensing for site-specific nitrogen fertilizer management," *Pesquisa Agropecuária Brasileira*, vol. 48, no. 10, pp. 1394–1401, 2013.
- [17] R. Tripathi, A. Nayak, R. Raja, M. Shahid, S. Mohanty, B. Lal, P. Gautam, B. Panda, A. Kumar, R. Sahoo, "Site-specific nitrogen management in rice using remote sensing and geostatistics," *Communications in Soil Science and Plant Analysis*, vol. 48, no. 10, pp. 1154–1166, 2017.
- [18] B. Bohman, C. Rosen, D. Mulla, "Evaluating remote sensing based adaptive nitrogen management for potato production," 2018.
- [19] I. Yule R. Pullanagari, "Optical sensors to assist agricultural crop and pasture management," in *Smart Sensing Technology for Agriculture and Environmental Monitoring*, Springer, 2012, pp. 21–32.
- [20] F. P. Povh W. d. P. G. dos Anjos, "Optical sensors applied in agricultural crops," in *Optical sensors-New developments and practical applications*, IntechOpen, 2014.
- [21] C. Sun, Y. Bian, T. Zhou, J. Pan, "Using of multi-source and multi-temporal remote sensing data improves crop-type mapping in the subtropical agriculture region," *Sensors*, vol. 19, no. 10, p. 2401, 2019.
- [22] B. D. Wardlow S. L. Egbert, "Large-area crop mapping using time-series MODIS 250 m NDVI data: An assessment for the US Central Great Plains," *Remote sensing of environment*, vol. 112, no. 3, pp. 1096–1116, 2008.
- [23] D. Arvor, M. Jonathan, M. S. P. Meirelles, V. Dubreuil, L. Durieux, "Classification of MODIS EVI time series for crop mapping in the state of Mato Grosso, Brazil," *International Journal of Remote Sensing*, vol. 32, no. 22, pp. 7847–7871, 2011.
- [24] N. Torbick, X. Huang, B. Ziniti, D. Johnson, J. Masek, M. Reba, "Fusion of moderate resolution earth observations for operational crop type mapping," *Remote Sensing*, vol. 10, no. 7, p. 1058, 2018.

- [25] N. Kussul, S. Skakun, A. Shelestov, O. Kravchenko, J. F. Gallego, O. Kussul, "Crop area estimation in Ukraine using satellite data within the MARS project," in *2012 IEEE international geoscience and remote sensing symposium*, IEEE, 2012, pp. 3756–3759.
- [26] X. Xiao, S. Boles, J. Liu, D. Zhuang, S. Frolking, C. Li, W. Salas, B. Moore III, "Mapping paddy rice agriculture in southern china using multi-temporal MODIS images," *Remote sensing of environment*, vol. 95, no. 4, pp. 480–492, 2005.
- [27] M.-N. Tuanmu, A. Viña, S. Bearer, W. Xu, Z. Ouyang, H. Zhang, J. Liu, "Mapping understory vegetation using phenological characteristics derived from remotely sensed data," *Remote Sensing of Environment*, vol. 114, no. 8, pp. 1833–1844, 2010.
- [28] A. Potgieter, K. Lawson, A. R. Huete, "Determining crop acreage estimates for specific winter crops using shape attributes from sequential MODIS imagery," *International Journal of Applied Earth Observation and Geoinformation*, vol. 23, pp. 254–263, 2013.
- [29] A. Schut, D. Stephens, R. Stovold, M. Adams, R. Craig, "Improved wheat yield and production forecasting with a moisture stress index, AVHRR and MODIS data," *Crop and Pasture Science*, vol. 60, no. 1, pp. 60–70, 2009.
- [30] M. Sharifi, "Crop inventory and production forecasting using remote sensing and agrometorological models: The case of major agricultural commodities in hamadan province, iran," *International Archives of Photogrammetry and Remote Sensing*, vol. 33, no. B7/4; PART 7, pp. 1364–1372, 2000.
- [31] M. M. Awad, "Toward precision in crop yield estimation using remote sensing and optimization techniques," *Agriculture*, vol. 9, no. 3, p. 54, 2019.
- [32] I. Ahmad, A. Ghafoor, M. I. Bhatti, I.-u. H. Akhtar, M. Ibrahim, "Satellite remote sensing and GIS-based crops forecasting & estimation system in Pakistan," *Crop monitoring for improved food security*, 2014.
- [33] A. Moreira, P. Prats-Iraola, M. Younis, G. Krieger, I. Hajnsek, K. P. Papathanassiou, "A tutorial on synthetic aperture radar," *IEEE Geoscience and remote sensing magazine*, vol. 1, no. 1, pp. 6–43, 2013.
- [34] T.-D. Guyenne, "Satellite radar in agriculture. experience with ERS-1," in *ESA Special Publication*, vol. 1185, 1995.
- [35] J. Soria-Ruiz, Y. Fernandez-Ordonez, H. McNairm, J. Bugden-Storie, "Corn monitoring and crop yield using optical and RADARSAT-2 images," in *2007 IEEE International Geoscience and Remote Sensing Symposium*, IEEE, 2007, pp. 3655–3658.
- [36] G. Forkuor, C. Conrad, M. Thiel, T. Ullmann, E. Zoungrana, "Integration of optical and synthetic aperture radar imagery for improving crop mapping in northwestern benin, west africa," *Remote sensing*, vol. 6, no. 7, pp. 6472–6499, 2014.
- [37] S. C. Steele-Dunne, H. McNairn, A. Monsivais-Huertero, J. Judge, P.-W. Liu, K. Papathanassiou, "Radar remote sensing of agricultural canopies: A review," *IEEE Journal of Selected Topics in Applied Earth Observations and Remote Sensing*, vol. 10, no. 5, pp. 2249–2273, 2017.

- [38] H. McNairn B. Brisco, "The application of c-band polarimetric SAR for agriculture: A review," *Canadian Journal of Remote Sensing*, vol. 30, no. 3, pp. 525–542, 2004.
- [39] H. S. Srivastava, P. Patel, R. R. Navalgund, "Application potentials of synthetic aperture radar interferometry for land-cover mapping and crop-height estimation.," *Current Science* (00113891), vol. 91, no. 6, 2006.
- [40] B. Brisco, R. Brown, M. Manore, "Early season crop discrimination with combined SAR and TM data," *Canadian Journal of Remote Sensing*, 1989.
- [41] Y. Ban, "Synergy of multitemporal ERS-1 SAR and Landsat TM data for classification of agricultural crops," *Canadian Journal of Remote Sensing*, vol. 29, no. 4, pp. 518–526, 2003.
- [42] G. Chust, D. Ducrot, J. L. Pretus, "Land cover discrimination potential of radar multitemporal series and optical multispectral images in a mediterranean cultural landscape," *International Journal of Remote Sensing*, vol. 25, no. 17, pp. 3513–3528, 2004.
- [43] G. Hong, A. Zhang, F. Zhou, B. Brisco, "Integration of optical and synthetic aperture radar (SAR) images to differentiate grassland and alfalfa in prairie area," *International Journal of Applied Earth Observation and Geoinformation*, vol. 28, pp. 12–19, 2014.
- [44] J. Inglada, A. Vincent, M. Arias, C. Marais-Sicre, "Improved early crop type identification by joint use of high temporal resolution SAR and optical image time series," *Remote Sensing*, vol. 8, no. 5, p. 362, 2016.
- [45] M. Hirschmugl, C. Sobe, J. Deutscher, M. Schardt, "Combined use of optical and synthetic aperture radar data for REDD+ applications in Malawi," *Land*, vol. 7, no. 4, p. 116, 2018.
- [46] T. Strozzi, P. B. Dammert, U. Wegmuller, J.-M. Martinez, J. I. Askne, A. Beaudoin, N. Hallikainen, "Landuse mapping with ERS SAR interferometry," *IEEE Transactions on Geoscience and Remote Sensing*, vol. 38, no. 2, pp. 766–775, 2000.
- [47] E. Rignot, S. Gogineni, W. Krabill, S. Ekholm, "North and northeast greenland ice discharge from satellite radar interferometry," *Science*, vol. 276, no. 5314, pp. 934–937, 1997.
- [48] P. Ferrazzoli, S. Paloscia, P. Pampaloni, G. Schiavon, S. Sigismondi, D. Solimini, "The potential of multifrequency polarimetric SAR in assessing agricultural and arboreous biomass," *IEEE Transactions on Geoscience and Remote Sensing*, vol. 35, no. 1, pp. 5–17, 1997.
- [49] F. T. Ulaby, "Radar remote sensing and surface scattering and emission theory," *Microwave remote sensing: active and passive*, 1982.
- [50] M. Karjalainen, H. Kaartinen, J. Hyyppä, "Agricultural monitoring using Envisat alternating polarization SAR images," *Photogrammetric Engineering & Remote Sensing*, vol. 74, no. 1, pp. 117–126, 2008.
- [51] W.-M. Boerner, "Recent advances in radar polarimetry and polarimetric SAR interferometry," ILLINOIS UNIV AT CHICAGO, Tech. Rep., 2005.

- [52] W.-M. Boerner, "Recent advances in polarimetry and polarimetric interferometry," in *2006 IEEE International Symposium on Geoscience and Remote Sensing*, IEEE, 2006, pp. 49–51.
- [53] F. Mattia, T. Le Toan, G. Picard, F. I. Posa, A. D'Alessio, C. Notarnicola, A. M. Gatti, M. Rinaldi, G. Satalino, G. Pasquariello, "Multitemporal C-band radar measurements on wheat fields," *IEEE Transactions on Geoscience and Remote Sensing*, vol. 41, no. 7, pp. 1551–1560, 2003.
- [54] X. Jiao, H. McNairn, J. Shang, E. Pattey, J. Liu, C. Champagne, "The sensitivity of RADARSAT-2 polarimetric SAR data to corn and soybean leaf area index," *Canadian Journal of Remote Sensing*, vol. 37, no. 1, pp. 69–81, 2011.
- [55] G. Wiseman, H. McNairn, S. Homayouni, J. Shang, "RADARSAT-2 polarimetric SAR response to crop biomass for agricultural production monitoring," *IEEE Journal of Selected Topics in Applied Earth Observations and Remote Sensing*, vol. 7, no. 11, pp. 4461–4471, 2014.
- [56] X. Blaes, P. Defourny, U. Wegmuller, A. Della Vecchia, L. Guerriero, P. Ferrazzoli, "C-band polarimetric indexes for maize monitoring based on a validated radiative transfer model," *IEEE transactions on geoscience and remote sensing*, vol. 44, no. 4, pp. 791–800, 2006.
- [57] C. Liao, J. Wang, J. Shang, X. Huang, J. Liu, T. Huffman, "Sensitivity study of Radarsat-2 polarimetric SAR to crop height and fractional vegetation cover of corn and wheat," *International journal of remote sensing*, vol. 39, no. 5, pp. 1475–1490, 2018.
- [58] N. Baghdadi, N. Boyer, P. Todoroff, M. El Hajj, A. Bégué, "Potential of SAR sensors TerraSAR-X, ASAR/ENVISAT and PALSAR/ALOS for monitoring sugarcane crops on reunion island," *Remote Sensing of Environment*, vol. 113, no. 8, pp. 1724–1738, 2009.
- [59] X. Wang, L. Ge, X. Li, "Pasture monitoring using sar with cosmo-skymed, envisat asar, and alos palsar in otway, australia," *Remote Sensing*, vol. 5, no. 7, pp. 3611–3636, 2013.
- [60] K. Voormansik, T. Jagdhuber, A. Olesk, I. Hajnsek, K. P. Papathanassiou, "Towards a detection of grassland cutting practices with dual polarimetric TerraSAR-X data," *International journal of remote sensing*, vol. 34, no. 22, pp. 8081–8103, 2013.
- [61] K. Voormansik, T. Jagdhuber, K. Zalite, M. Noorma, I. Hajnsek, "Observations of cutting practices in agricultural grasslands using polarimetric SAR," *IEEE Journal of Selected Topics in Applied Earth Observations and Remote Sensing*, vol. 9, no. 4, pp. 1382–1396, 2015.
- [62] U. Wegmuller C. L. Werner, "Sar interferometric signatures of forest," *IEEE Transactions on Geoscience and Remote Sensing*, vol. 33, no. 5, pp. 1153–1161, 1995.
- [63] H. A. Zebker J. Villasenor, "Decorrelation in interferometric radar echoes," *IEEE Transactions on geoscience and remote sensing*, vol. 30, no. 5, pp. 950–959, 1992.

- [64] K. Zalite, K. Voormansik, J. Praks, O. Antropov, M. Noorma, "Towards detecting mowing of agricultural grasslands from multi-temporal COSMO-SkyMed data," in *2014 IEEE Geoscience and Remote Sensing Symposium*, IEEE, 2014, pp. 5076–5079.
- [65] K. Zalite, O. Antropov, J. Praks, K. Voormansik, M. Noorma, "Monitoring of agricultural grasslands with time series of X-band repeat-pass interferometric SAR," *IEEE Journal of Selected Topics in Applied Earth Observations and Remote Sensing*, vol. 9, no. 8, pp. 3687–3697, 2015.
- [66] U. Wegmuller C. Werner, "Retrieval of vegetation parameters with SAR interferometry," *IEEE Transactions on Geoscience and Remote Sensing*, vol. 35, no. 1, pp. 18–24, 1997.
- [67] M. Santoro, U. Wegmuller, J. I. Askne, "Signatures of ERS–Envisat interferometric SAR coherence and phase of short vegetation: An analysis in the case of maize fields," *IEEE Transactions on Geoscience and Remote Sensing*, vol. 48, no. 4, pp. 1702–1713, 2009.
- [68] J. I. Askne, P. B. Dammert, L. M. Ulander, G. Smith, "C-band repeat-pass interferometric SAR observations of the forest," *IEEE Transactions on Geoscience and Remote Sensing*, vol. 35, no. 1, pp. 25–35, 1997.
- [69] J. Askne, M. Santoro, G. Smith, J. E. Fransson, "Multitemporal repeat-pass SAR interferometry of boreal forests," *IEEE Transactions on Geoscience and Remote Sensing*, vol. 41, no. 7, pp. 1540–1550, 2003.
- [70] C. Proisy, E. Mougin, A. Lopes, F. Sarti, E. Dufrene, V. LeDantec, P. Borderies, I. Chênerie, "Temporal variations of interferometric coherence over a deciduous forest," in *SAR workshop: CEOS Committee on Earth Observation Satellites*, vol. 450, 2000, p. 25.
- [71] T. Tamm, K. Zalite, K. Voormansik, L. Talgre, "Relating sentinel-1 interferometric coherence to mowing events on grasslands," *Remote Sensing*, vol. 8, no. 10, p. 802, 2016.
- [72] G. Joseph, Fundamentals of remote sensing. Universities Press, 2005.
- [73] J. Awange J. Kiema, "Environmental geoinformatics," *Berlin, Heidelberg: Springer Berlin Heidelberg. doi*, vol. 10, pp. 978–3, 2013.
- [74] M. Engdahl *et al.*, "Multitemporal InSAR in land-cover and vegetation mapping," 2013.
- [75] Y. K. Chan V. C. Koo, "An introduction to synthetic aperture radar (SAR)," *Progress In Electromagnetics Research*, vol. 2, pp. 27–60, 2008.
- [76] N. Kerle, L. L. Janssen, G. C. Huurneman, "Principles of remote sensing," *ITC, Educational textbook series*, vol. 2, pp. 46–64, 2004.
- [77] K. Ouchi, "Recent trend and advance of synthetic aperture radar with selected topics," *Remote Sensing*, vol. 5, no. 2, pp. 716–807, 2013.
- [78] J. W. Merchant, "Remote sensing of the environment: An earth resource perspective," *Cartography and Geographic Information Science*, vol. 27, no. 4, pp. 311–311, 2000.
- [79] R. F. Hanssen, *Radar interferometry: data interpretation and error analysis*. Springer Science & Business Media, 2001, vol. 2.

- [80] G. Franceschetti R. Lanari, *Synthetic aperture radar processing*. CRC press, 2018.
- [81] J. C. Curlander R. N. McDonough, *Synthetic aperture radar*. John Wiley & Sons New York, NY, USA: 1991, vol. 396.
- [82] F. T. Ulaby, R. K. Moore, A. K. Fung, "Microwave remote sensing: Active and passive. volume 3-from theory to applications," 1986.
- [83] M. Suess W. Wiesbeck, "Side-looking synthetic aperture radar system," *European Patent EP*, vol. 1, no. 241, p. 487, 2002.
- [84] F. M. Henderson A. J. Lewis, "Principles and applications of imaging radar. Manual of remote sensing: Volume 2," 1998.
- [85] R. K. Raney, H. Runge, R. Bamler, I. G. Cumming, F. H. Wong, "Precision SAR processing using chirp scaling," *IEEE Transactions on geoscience and remote sensing*, vol. 32, no. 4, pp. 786–799, 1994.
- [86] C. Wolff, "Radar tutorial," Retrieved February, vol. 15, p. 2012, 2012.
- [87] M. Born E. Wolf, *Principles of optics: electromagnetic theory of propagation, interference, and diffraction of light.* Macmillan, 1959.
- [88] J. R. Jensen, "Remote sensing of the environment-an earth resource perspective prentice hall," *Inc., Upper Saddle River, New Jersey*, 2000.
- [89] R. Touzi, W. Boerner, J. Lee, E. Lueneburg, "A review of polarimetry in the context of synthetic aperture radar: Concepts and information extraction," *Canadian Journal of Remote Sensing*, vol. 30, no. 3, pp. 380–407, 2004.
- [90] O. Landron, M. J. Feuerstein, T. S. Rappaport, "In situ microwave reflection coefficient measurements for smooth and rough exterior wall surfaces," in *IEEE 43rd Vehicular Technology Conference*, IEEE, 1993, pp. 77–80.
- [91] J. Trevett, "Imaging radar for resources surveys," 1987.
- [92] M. S. Rahman L. Di, "The state of the art of spaceborne remote sensing in flood management," *Natural Hazards*, vol. 85, no. 2, pp. 1223–1248, 2017.
- [93] A. K. Gabriel, R. M. Goldstein, H. A. Zebker, "Mapping small elevation changes over large areas: Differential radar interferometry," *Journal of Geophysical Research: Solid Earth*, vol. 94, no. B7, pp. 9183–9191, 1989.
- [94] D. Massonnet K. L. Feigl, "Radar interferometry and its application to changes in the earth's surface," *Reviews of geophysics*, vol. 36, no. 4, pp. 441–500, 1998.
- [95] S. Abdikan, "Monitoring of land surface subsidence in zonguldak coal mining field in the northern turkey using multi temporal SAR interferometry," 2012.
- [96] A. Smith, P. Eddy, J. Bugden-Storie, E. Pattey, H. McNairn, M. Nolin, I. Perron, M. Hinther, J. Miller, D. Haboudane, "Multipolarized radar for delineating within-field variability in corn and wheat," *Canadian Journal of Remote Sensing*, vol. 32, no. 4, pp. 300–313, 2006.
- [97] J. S. Ruiz, Y. F. Ordonez, H. McNairn, "Corn monitoring and crop yield using optical and microwave remote sensing," *Geoscience and Remote Sensing, Edited by Pei-Gee Peter Ho, DOI*, vol. 10, no. 46146, pp. 405–420, 2008.

- [98] V. Santalla, Y. M. Antar, A. Pino, "Polarimetric radar covariance matrix algorithms and applications to meteorological radar data," *IEEE transactions on geoscience and remote sensing*, vol. 37, no. 2, pp. 1128–1137, 1999.
- [99] J. Lee E. Pottier, "Electromagnetic vector scattering operators," *Polarimetric Radar Imaging: From Basics to Applications; CRC Press: New York, NY, USA*, 2009.
- [100] J. Van Zyl, "Scattering matrix representations for simple targets," *Radar polarimetry for geoscience applications*, 1990.
- [101] K. Conradsen, A. A. Nielsen, H. Skriver, "Determining the points of change in time series of polarimetric SAR data," *IEEE Transactions on Geoscience and Remote Sensing*, vol. 54, no. 5, pp. 3007–3024, 2016.
- [102] T. L. Ainsworth, J. Kelly, J.-S. Lee, "Polarimetric analysis of dual polarimetric SAR imagery," in 7th European Conference on Synthetic Aperture Radar, VDE, 2008, pp. 1–4.
- [103] Y. Duguay, M. Bernier, E. Lévesque, B. Tremblay, "Potential of C and X band SAR for shrub growth monitoring in sub-arctic environments," *Remote Sensing*, vol. 7, no. 7, pp. 9410–9430, 2015.
- [104] A. A. Nielsen, K. Conradsen, H. Skriver, M. J. Canty, "Change detection in a series of Sentinel-1 SAR data," in 2017 9th International Workshop on the Analysis of Multitemporal Remote Sensing Images (MultiTemp), IEEE, 2017, pp. 1–3.
- [105] S. R. Cloude E. Pottier, "A review of target decomposition theorems in radar polarimetry," *IEEE transactions on geoscience and remote sensing*, vol. 34, no. 2, pp. 498–518, 1996.
- [106] —, "An entropy based classification scheme for land applications of polarimetric sar," *IEEE transactions on geoscience and remote sensing*, vol. 35, no. 1, pp. 68–78, 1997.
- [107] K. Li, B. Brisco, S. Yun, R. Touzi, "Polarimetric decomposition with RADARSAT-2 for rice mapping and monitoring," *Canadian Journal of Remote Sensing*, vol. 38, no. 2, pp. 169–179, 2012.
- [108] H. McNairn, J. Shang, X. Jiao, C. Champagne, "The contribution of ALOS PALSAR multipolarization and polarimetric data to crop classification," *IEEE Transactions on Geoscience and Remote Sensing*, vol. 47, no. 12, pp. 3981–3992, 2009.
- [109] S. D. Kumar, S. S. Rao, J. Sharma, "Radar vegetation index as an alternative to NDVI for monitoring of soyabean and cotton," in *Proceedings of the XXXIII INCA International Congress (Indian Cartographer), Jodhpur, India*, 2013, pp. 19–21.
- [110] Y. Kim J. van Zyl, "Vegetation effects on soil moisture estimation," in *IGARSS* 2004. 2004 IEEE International Geoscience and Remote Sensing Symposium, IEEE, vol. 2, 2004, pp. 800–802.
- [111] Y. Kim J. J. van Zyl, "A time-series approach to estimate soil moisture using polarimetric radar data," *IEEE Transactions on Geoscience and Remote Sensing*, vol. 47, no. 8, pp. 2519–2527, 2009.

- [112] F. Charbonneau, M. Trudel, R. Fernandes, "Use of dual polarization and multi-incidence SAR for soil permeability mapping," *Advanced Synthetic Aperture Radar (ASAR)* 2005, 2005.
- [113] M. Trudel, F. Charbonneau, R. Leconte, "Using RADARSAT-2 polarimetric and ENVISAT-ASAR dual-polarization data for estimating soil moisture over agricultural fields," *Canadian Journal of Remote Sensing*, vol. 38, no. 4, pp. 514–527, 2012.
- [114] N. R. Goodman, "Statistical analysis based on a certain multivariate complex gaussian distribution (an introduction)," *The Annals of mathematical statistics*, vol. 34, no. 1, pp. 152–177, 1963.
- [115] E. Rodriguez J. Martin, "Theory and design of interferometric synthetic aperture radars," in *IEE Proceedings F (Radar and Signal Processing)*, IET, vol. 139, 1992, pp. 147–159.
- [116] C. Patri F. Rocca, "Range resolution enhancement with multiple SAR surveys combination," in [Proceedings] IGARSS'92 International Geoscience and Remote Sensing Symposium, IEEE, vol. 2, 1992, pp. 1576–1578.
- [117] F. Rocca, C. Prati, P. Pasquali, A. M. Guarnieri, "ERS-1 SAR interferometry techniques and applications," *ESA, Noordwijk, The Netherlands, Contract Rep*, no. 3-7439, p. 92, 1994.
- [118] A. Ferretti, A. Monti Guarnieri, C. Prati, F. Rocca, D. Massonnet, February 2007. INSAR principles: Guidelines for SAR interferometry processing and interpretation.
- [119] C.-H. Lu, C.-F. Ni, C.-P. Chang, J.-Y. Yen, R. Chuang, "Coherence difference analysis of sentinel-1 SAR interferogram to identify earthquake-induced disasters in urban areas," *Remote Sensing*, vol. 10, no. 8, p. 1318, 2018.
- [120] R. Bamler P. Hartl, "Synthetic aperture radar interferometry," *Inverse problems*, vol. 14, no. 4, R1, 1998.
- [121] P. A. Rosen, S. Hensley, I. R. Joughin, F. K. Li, S. N. Madsen, E. Rodriguez, R. M. Goldstein, "Synthetic aperture radar interferometry," *Proceedings of the IEEE*, vol. 88, no. 3, pp. 333–382, 2000.
- [122] D. Sandwell, R. Mellors, X. Tong, M. Wei, P. Wessel, "Open radar interferometry software for mapping surface deformation," *Eos, Transactions American Geophysical Union*, vol. 92, no. 28, pp. 234–234, 2011.
- [123] A. B. Ruescas, J. M. Delgado, F. Costantini, F. Sarti, "Change detection by interferometric coherence in nasca lines, peru (1997–2004)," *Fringe 2009*, vol. 30, 2009.
- [124] M. Born E. Wolf, Principles of optics: electromagnetic theory of propagation, interference and diffraction of light. Elsevier, 2013.
- [125] P. A. Rosen, S. Hensley, H. A. Zebker, F. H. Webb, E. J. Fielding, "Surface deformation and coherence measurements of kilauea volcano, hawaii, from SIR-C radar interferometry," *Journal of Geophysical Research: Planets*, vol. 101, no. E10, pp. 23 109–23 125, 1996.

- [126] D. Massonnet, K. Feigl, M. Rossi, F. Adragna, "Radar interferometric mapping of deformation in the year after the landers earthquake," *Nature*, vol. 369, no. 6477, p. 227, 1994.
- [127] S. Chelbi, A. Khireddine, J. Charles, "Interferometry process for satellite images SAR," in 2011 7th International Conference on Electrical and Electronics Engineering (ELECO), IEEE, 2011, pp. II–200.
- [128] D. Just R. Bamler, "Phase statistics of interferograms with applications to synthetic aperture radar," *Applied optics*, vol. 33, no. 20, pp. 4361–4368, 1994.
- [129] J. Feranec, T. Soukup, G. Hazeu, G. Jaffrain, European landscape dynamics: CORINE land cover data. CRC Press, 2016.
- [130] L. Li, Q. Kong, P. Wang, L. Xun, L. Wang, L. Xu, Z. Zhao, "Precise identification of maize in the north china plain based on Sentinel-1A SAR time series data," *International Journal of Remote Sensing*, vol. 40, no. 5-6, pp. 1996–2013, 2019.
- [131] K. Koppel, K. Zalite, K. Voormansik, T. Jagdhuber, "Sensitivity of Sentinel-1 backscatter to characteristics of buildings," *International Journal of Remote Sensing*, vol. 38, no. 22, pp. 6298–6318, 2017.
- [132] A. Mordvintsev K. Abid, "Opency-python tutorials documentation," *Obtenido de https://media. readthedocs. org/pdf/opency-python-tutroals/latest/opency-python-tutroals. pdf*, 2014.
- [133] U. Meier, "Bbch monograph, federal biological research centre for agriculture and forestry. 2001," *Growth stages of mono-and dicotyledonous plants*,
- [134] G. Macelloni, S. Paloscia, P. Pampaloni, F. Marliani, M. Gai, "The relationship between the backscattering coefficient and the biomass of narrow and broad leaf crops," *IEEE Transactions on Geoscience and Remote Sensing*, vol. 39, no. 4, pp. 873–884, 2001.
- [135] G. V. Laurin, V. Liesenberg, Q. Chen, L. Guerriero, F. Del Frate, A. Bartolini, D. Coomes, B. Wilebore, J. Lindsell, R. Valentini, "Optical and SAR sensor synergies for forest and land cover mapping in a tropical site in west africa," *International Journal of Applied Earth Observation and Geoinformation*, vol. 21, pp. 7–16, 2013.
- [136] L. Veci, J. Lu, P. Prats-Iraola, R. Scheiber, F. Collard, N. Fomferra, M. Engdahl, "The Sentinel-1 Toolbox," in *Proceedings of the IEEE International Geoscience and Remote Sensing Symposium (IGARSS)*, 2014, pp. 1–3.
- [137] H. G. Solutions, *Interactive data language*, 1977.
- [138] I. VIS, "ENVI atmospheric correction module: QUAC and FLAASH user's guide," *Module Version*, vol. 4, pp. 1–44, 2009.
- [139] L. Congedo, "Semi-automatic classification plugin documentation," *Release*, vol. 4, no. 0.1, p. 29, 2016.
- [140] R. ESRI, "ArcGIS desktop: Release 10," *Environmental Systems Research Institute, CA*, 2011.
- [141] Q. D. Team *et al.*, "QGIS geographic information system. open source geospatial foundation project," *URL: http://qgis. osgeo. org*, 2015.

- [142] R. Nasirzadehdizaji, F. Balik Sanli, S. Abdikan, Z. Cakir, A. Sekertekin, M. Ustuner, "Sensitivity analysis of multi-temporal Sentinel-1 SAR parameters to crop height and canopy coverage," *Applied Sciences*, vol. 9, no. 4, p. 655, 2019.
- [143] D. Sandwell, R. Mellors, X. Tong, M. Wei, P. Wessel, "Gmtsar: An insar processing system based on generic mapping tools," 2011.
- [144] P. Wessel W. H. Smith, "New, improved version of Generic Mapping Tools released," *Eos, Transactions American Geophysical Union*, vol. 79, no. 47, pp. 579–579, 1998.

Publications From the Thesis

Contact Information: rouhollah.nasirzadehdizaji@std.yildiz.edu.tr

Papers

1. R. Nasirzadehdizaji, F. Balik Sanli, S. Abdikan, Z. Cakir, A. Sekertekin, M.Ustuner, "Sensitivity analysis of multi-temporal Sentinel-1 SAR parameters to crop height and canopy coverage," *Applied Sciences*, vol. 9, no. 4, p. 655, 2019.

Conference Papers

- 1. R. Nasirzadehdizaji, F. Balik Sanli, Z. Cakir, "Application of sentinel-1 multi-temporal data for crop monitoring and mapping, "The International Archives of Photogrammetry, Remote Sensing and Spatial Information Sciences, vol. 42, pp. 803–807, 2019.
- 2. R. Nasirzadehdizaji, F. Balik Sanli, Z. Cakir, E. Sertel, "Crop mapping improvement by combination of optical and sar datasets," in 2019 8th International Conference on Agro-Geoinformatics (Agro-Geoinformatics), IEEE, 2019, pp. 1–6.
- 3. S. Abdikan, A. Sekertekin, M. Ustunern, F. B. Sanli, R. Nasirzadehdizaji, "Backscatter analysis using multi-temporal sentinel-1 SAR data for crop growth of maize in konya basin, turkey," in Proceedings of the ISPRS TC III Mid-Term Symposium "Developments, Technologies and Applications in Remote Sensing", Beijing, China, 2018, pp. 7–10.

Awards

1. Taking 2nd place in presentations session for the presenting titled with "Sentinel-1 Polarimetric SAR Data Sensitivity Studying to Crop Variables," *in XXXII International Geodetic Student Meeting held at Faculty of Geodesy and Cartography of Warsaw University of Technology, Poland*, 2019.